A STUDY OF A DUAL POLARIZATION LASER BACKSCATTER SYSTEM FOR REMOTE IDENTIFICATION AND MEASUREMENT OF WATER POLLUTION

BY

THOMAS CARLYLE SHEIVES

May 1974

Supported by

United States Coast Guard
Contract DOT-CG-34017-A

and

National Aeronautics and Space Administration
Grant NGL 44-001-001

TEXAS A&M UNIVERSITY
REMOTE SENSING CENTER
COLLEGE STATION, TEXAS

TECHNICAL REPORT RSC-53

A STUDY OF A DUAL POLARIZATION LASER BACKSCATTER SYSTEM FOR REMOTE IDENTIFICATION AND MEASUREMENT OF WATER POLLUTION

by

THOMAS CARLYLE SHEIVES

May 1974

Supported by

United States Coast Guard
Contract DOT-CG-34017-A

and

National Aeronautics and Space Administration
Grant NGL 44-001-001

ABSTRACT

A Study of a Dual Polarization Laser Backscatter System For Remote Identification and Measurement of Water Pollution. (May 1974)

Thomas Carlyle Sheives, B.S., Texas A&M University and B.A., Baylor University

Chairman of Advisory Committee: Dr. J. W. Rouse, Jr.

This study examines the applicability of a dual polarization laser backscatter system (lidar polarimeter) for remote identification and measurement of subsurface water turbidity and oil on water. Analytical models for describing the backscatter from turbid water and oil on turbid water are developed and compared with experimental data. Lidar measurements from natural waterways are also presented and compared with ground observations of several physical water quality parameters.

The analytical model for describing the backscatter from smooth surfaced, turbid water includes subsurface single scatter and multiple scatter effects. The like polarized backscatter is modeled by an incoherent sum of a subsurface single scatter term and a subsurface multiple scatter term. The single scatter term is represented by a Mie scatter model, incorporating the Mie scattering and extinction coefficients. The multiple scatter term employs

a multiple scatter volume reflection coefficient, similar to that used in the analytical treatments of backscatter by Rouse [30] and Wilhelmi [18]. Experimental laboratory data presented in this report verify the validity of the analytical model and demonstrate the characteristic that the depolarization ratio (cross return divided by like return) increases with an increase in water turbidity.

Field measurement data from several natural waterways show that the like and cross returns, and the depolarization ratio, vary directly with the water quality parameters turbidity and suspended solids, and inversely with transmittance. These data support the use of a lidar polarimeter for remote measurements of these physical water quality parameters.

The analytical model for backscatter from oil on water includes the effect on the backscatter of the change in refractive index and the attenuation due to oil. The oil layer is considered to be a laterally inhomogeneous, lossy dielectric. Experimental data performed in the laboratory verify the validity of the analytical model and establish the following characteristics of the data: 1) the presence of oil on turbid water does not significantly alter the depolarization ratio; and 2) the attenuation due to oil is a function of oil type, oil thickness, and excitation wavelength. Considering these effects on the

backscatter, a detection scheme is presented whereby the presence of oil on water can be established by using a single wavelength lidar polarimeter. A detection, type identification, and thickness measurement method is also presented using a dual wavelength lidar polarimeter. Using these results, the applicability of a lidar polarimeter for oil detection, identification, and thickness measurement is established.

ACKNOWLEDGEMENTS

For his guidance and support during this research effort, I would like to express my sincere appreciation to Dr. J. W. Rouse, Jr. The assistance of Dr. Charles Adams of the Data Processing Center at Texas A&M University in the calculation of the scattering coefficients is also gratefully acknowledged. This research was supported by the United States Coast Guard (Contract DOT-CG-34017-A) and the National Aeronautics and Space Administration (Grant NGL 44-001-001).

The water sample analyses and vessel operations offered by Environmental Engineering under the Civil Engineering Department is gratefully acknowledged. Also, the assistance in the data acquisition given by Mr. W. C. Hulse, Mr. S. L. Lee, Mr. T. L. Brown, and Mr. L. D. Daigle of the Remote Sensing Center is appreciated.

TABLE OF CONTENTS

LIST OF TABLES

LIST OF FIGURES

CHAPTER I

INTRODUCTION

The water environment can generally be characterized as a dilute, aqueous solution, containing a large variety of dissolved and suspended, organic and inorganic, chemical species, and including an abundance of plant and animal life [1]. Because of the invaluable productivity and aesthetic value that this environment provides, the control of industrial, agricultural, and municipal water waste discharges has become increasingly important. Control efforts exerted by governmental agencies have been segmented into two areas: the control of surface effluents, and the control of subsurface effluents. The most harmful surface effluent presently receiving waste control attention is oil on water. Several ecological investigations have shown that petroleum products discharged or spilled in the water environment present a serious threat to the existence of the aquatic habitat. Suspended subsurface pollutants from precipitation run-off or industrial discharge have also generated significant concern among

environmentalists because of impairment to the aquatic habitat and degradation of the aesthetic value.

While governmental agencies have attempted to control surface and subsurface pollution, their efforts have been handicapped by the ineffectiveness of present day instrumentation methods for identifying and measuring water pollutants. These methods usually require either slow laboratory analysis, or expensive field equipment analysis. This report discusses some of the present methods of water quality analysis, and then presents a new method utilizing laser backscatter for performing remote, continuous, real-time identification and measurement of oil on water and selected water quality parameters.

Water Quality Determination

The purpose of water quality parameters is to provide a means for quantitatively describing water impurities. Three basic classifications of water quality parameters are biological, chemical, and physical, each of which refers to the nature of the water impurity. This section describes some of the present methods for determining these parameters.

Direct Sampling Methods

The traditional approach to measuring water quality parameters involves direct sampling methods. These measurement methods can generally be divided into two categories: 1) laboratory measurements and 2) *in situ* measurements. Laboratory measurements involve collection of water samples from the sites, followed by an analysis of the samples in the laboratory. There are two major problems associated with this approach: 1) the analysis of the samples is not real-time and therefore cannot adequately monitor the dynamic pollutant variations that occur in the water environment; and 2) the physical and chemical form of the desired constituent may be altered as a result of moving the sample from its natural environment.

In situ measurements attempt to alleviate some of these problems. This measurement method requires portable field equipment which can determine water quality parameters at the site. This method is usually preferrable to the laboratory method but still has several inherent problems: 1) sample collecting and instrumentation operation usually require several qualified personnel; 2) large areas cannot be measured in short periods of time; 3) continuous analysis is usually not possible with present instrumentation methods; and 4) the measurement procedures

are usually very tedious.

The realization of the need for continuous, real-time water quality analysis has motivated several investigators to consider remote sensing techniques for water quality monitoring. The following section describes some of these investigations.

Remote Sensing Methods

The basic approach of remote sensing is the detection and measurement of electromagnetic radiation for the identification and measurement of geophysical phenomena. The source from which the electromagnetic radiation originates defines two types of remote sensing systems: *passive* systems and *active* systems. Passive systems identify and measure geophysical phenomena through the detection and measurement of *naturally* occurring radiation, such as solar or thermal radiation. Active systems, however, generate their own source energy and identify or measure geophysical phenomena through the measurement of the scattered, reflected, or transmitted *source* electromagnetic radiation.

Passive Systems. The simplest and oldest form of passive remote sensing is *photography*. The primary advantage of aerial photography is the performance of high ground resolution mapping with large areal coverage. For

determining water quality parameters, aerial photography senses natural radiation scattered or emitted from the water subsurface. Several aerial photography techniques have been used to detect water pollution, including the use of color film, infrared color film, and selective spectral filtering [2].

One problem that has restricted the successful application of aerial photography for water quality analysis has been the inability to separate peripheral atmospheric effects from the desired water subsurface radiation. Ground control reflectances have been used to suppress peripheral atmospheric effects but these have provided only marginally satisfactory results. Piech, et al. [3,4], however, introduced a scene color standard technique which provides accurate photographic measurements of volume spectral reflectances without interference from atmospheric effects. Their study showed the feasibility of accurate, quantitative analysis of physical water quality parameters through aerial photography.

Other studies in aerial photographic analysis of water quality have been performed by James and Burgess [5]. Through a computer analysis of data obtained from densitizing photographic data, an analysis of waste concentrations of pulp mill outfalls was made with the results giving approximately 90% correlations between photographic

data and ground observations of several physical water quality parameters.

In 1971, Halajian and Hallock [6] introduced a direct digital approach to the imaging and signature analysis of water targets and indicated that quantitative analysis of water turbidity and water depth was feasible. Later in 1971, Hallock and Halajian [7] reported a similar investigation using a passive dual-polarization system for remote sensing of water quality. This study indicated that dual polarization measurements offer another means of separating peripheral atmospheric effects from measurements of water subsurface reflectance.

Schwebel [8] has also shown the feasibility of determining turbidity using photographic methods. Color photography with selective spectral filtering was taken of numerous ponds with simultaneous measurements of ground observations of water turbidity. Correlations between 90% and 95% were obtained from a regression analysis of the photographic data with water turbidity. The usefulness of this method, however, was restricted by 1) the use of ground control reflectances, and 2) day-time operation only.

Passive infrared imagery has been used by Foster [9] to study thermal mixing in effluent waters. The results showed good accuracy in quantitative remote measurement

of water temperature. Thermal infrared imagery has also been applied to oil slick detection [10]. The imagery showed that areas with thin layers of oil appeared darker (colder) than the surrounding water, while areas with thick layers of oil appeared lighter (warmer).

Although some passive remote sensing systems have performed quantitative analysis of a few water quality parameters, these systems have had several disadvantages:
1) sensing is generally restricted to daytime only;
2) sensing is generally restricted to clear weather; and
3) parameter analysis is generally not real-time.

Active Systems. Active remote sensing is a relatively new approach for identifying geophysical characteristics. The primary advantage of active sensing over passive sensing is the capability of: 1) nighttime operation, and 2) detection insensitivity to ambient radiation.

Active microwave (radar) systems have been used in many earth resource applications. A recent investigation in water quality analysis includes the use of a four frequency microwave radar system for detecting oil slicks [11]. The results of this study indicate that detection of oil thickness of 1 μm are feasible, although classification of oil type could not be established.

The advent of the laser has provided a powerful new tool for application in active remote sensing of water

quality. Kim [12] has studied the application of an airborne laser fluorosensor for the detection of algae in the sea and has demonstrated the capability for measuring chlorophyll-a concentrations in a range from 0.0 to 30 mgs/m^3. Laser flourosensors have also been used for the detection of oil spills and have shown the feasibility of classifying oil types and thicknesses [13].

Granastein [14] reported in 1972 a laboratory study which used a linearly polarized laser and a beaker of water with known suspended scatterers and absorbers to determine the relation between the volume scatter and the concentrations scatterers and absorbers. Polarization effects were also considered in a later study [15]. The results indicated that the depolarization ratio (orthogonally depolarized backscatter divided by like polarized backscatter) depended on the ratio of the scattering to absorbing concentrations, and not the absolute mass concentrations. This work is significant in that it shows the dependence of the depolarization on subsurface effects.

Another study investigating laser backscatter from turbid water was conducted by Wilhelmi, Mayo, and Rouse [16]. A dual polarization laser backscatter system (lidar polarimeter) was constructed and used to measure backscatter from laboratory simulations of natural water. The hypothesis which motivated the design and construction

of the lidar polarimeter was that suspended contaminants in real water scatter and depolarize the incident radiation, and that the degree of depolarization should indicate concentrations of contaminants. Laboratory measurements of backscatter supported this hypothesis, and therefore the investigation established the feasibility of determining certain water quality parameters with a lidar polarimeter.

A further investigation with the lidar polarimeter was performed by Sheives [17]. In this study, an analytical model was presented which described the backscatter from smooth surface turbid water illuminated by vertically polarized laser light. Experimental measurements were performed and compared with calculated values. The results of this study were: 1) a further indication of the feasibility of using a lidar polarimeter for determining water quality parameters, and 2) the postulation that a volume multiple scatter mechanism should explain the depolarization process.

The most recent investigation with the lidar polarimeter was performed by Wilhelmi [18]. This study included a theoretical development of the polarized and depolarized backscatter component from a rough surface and a smooth surface, incorporating single scatter surface and multiple scatter subsurface effects. Experimental laboratory

measurements were performed to investigate the validity of the theoretical model. The results of this study indicated that since the theoretical values and the experimental values had correlation coefficients greater than 90%, a volume multiple scatter mechanism appears to explain the depolarization process.

Report Objectives

The foregoing discussion shows two important results which provide the stimulus for this investigation. First, it establishes the need for real-time identification and measurement of surface and subsurface water quality parameters; and second, it demonstrates the feasibility of using laser backscatter for this application. This investigation extends the previous laser backscatter studies in the following manner. First, a new analytical approach is taken to describe the backscatter from turbid water. Previous laser backscatter studies, such as that performed by Wilhelmi [18], assumed that the backscattered energy was entirely multiple scatter from the subsurface. However, backscatter measurements from turbid water show that the like-polarized component is significantly larger than the cross-polarized component which strongly suggests the presence of single scatter within the volume. Therefore, the model presented in this report incorporates

a single scatter component into the backscattered return. The results of laboratory measurements are also given to show the validity of the model.

A second extension of previous studies presented in this report is the development of an analytical model for describing the backscatter from oil on turbid water. An identification and measurement method using a lidar polarimeter for detecting oil on water is discussed along with preliminary laboratory measurements to examine the concept.

Furthermore, this report describes the results of numerous lidar polarimeter field measurements conducted from several natural waterways. A discussion of the field portable lidar polarimeter used in these field measurements along with an analysis of the data is included.

Scope of Report

Chapter II provides the necessary background for understanding the nature of water pollution and for selecting water quality parameters which appear suitable for detection by the lidar system.

Chapter III describes the analytical modeling techniques used to characterize the electromagnetic interaction between the water subsurface and the lidar system. Also included is an electromagnetic scattering model for oil on water.

Chapter IV describes the lidar polarimeter used in this investigation including a description of the system components and transceiver geometrical configuration.

Chapter V describes the experiments of this study. Lidar laboratory measurements with simulated turbid water and oil on water are discussed in conjunction with lidar field measurements performed from several natural waterways.

Chapter VI compares the experimental results with the analytical models for backscatter from turbid water and oil on turbid water. Lidar field measurement data are also presented graphically to show the relationships between the lidar returns and several water quality parameters.

Chapter VII gives the conclusions drawn from this study concerning the validity of the analytical models and the applicability of using laser backscatter for determining water quality parameters. In addition, this chapter provides recommendations for future investigations.

CHAPTER II

WATER QUALITY

This chapter discusses some of the characteristics of the water environment and concludes with a selection of surface and subsurface water quality parameters which appear applicable to detection and measurement by the laser sensor.

Water Environment

The water environment is a very complex, dynamic, heterogeneous system. The structure of the water environment generally consists of four constantly exchanging aquatic systems: estuaries, rivers, lakes, and oceans. The most dynamic and complex aquatic system is the estuary, defined as the mixing basin where the ocean water and fresh water rivers meet. The estuary is characterized by extremes in water quality, currents, and bottom deposits [19]. In addition, the intertidal zone is subjected to alternate exposure of air and water.

The fresh water rivers and lakes are burdened with the transport of waste discharges and sediment deposits. The ability of the rivers to assimilate these wastes depends largely on the type and volume of the wastes. When the levels of waste discharges are low, the water

removes the wastes and cleans itself. At higher levels of waste discharges, the ability of the rivers to assimilate wastes becomes restricted, resulting in environmental degradation.

The oceans, however, have almost an unlimited ability to assimilate wastes, and because of their relatively constant characteristics, absorb most of the effluents discharged into the estuary by the fresh water rivers.

The dynamic nature of the aquatic environment is a result of several factors, besides the obvious factor of varying waste discharges. Climatic conditions such as runoff from snowmelt or floods can produce muddy, soft water with a high bacterial count. Runoff during a drought, however, can produce high mineral content groundwater.

Geographic conditions also are a primary factor in water quality variations. For example, in the great belt of heavily populated areas along the east side of the Mississippi, sediment concentrations in most surface waters average less than 270 mg/liter. For the eastern United States though, sediment concentrations average approximately 1900 mg/liter [20].

Seasonal conditions such as aquatic organism growth, floods, droughts, waste discharges, and the overturn lakes and reservoirs, also contribute to the dynamic character

of the water environment.

Physical Subsurface Impurities

General Characteristics

Subsurface impurities in the aquatic environment, whether solid, liquid, or gas, are dispersed into three progressively finer states: suspended, colloidal, and dissolved. Dissolved impurities are those which are dispersed in water as single molecules or ions [20]. Generally, particles less than .01 μm are classified as dissolved impurities.

Insoluble material is usually defined as any particle from .01 to 200 μm in diameter, and includes both suspended and colloidal materials. Particles greater than 200 μm will not generally be found suspended in water unless the water has high velocity currents, or unless the matter is bouyant bio-organic particles [20].

Many investigations have been conducted to study the size distribution of particles suspended in the ocean. Sheldon, et al. [21] used the Coulter counter technique to study suspended particles in the North Atlantic Ocean surface waters and found particle sizes with geometric mean diameters of approximately 20 μm. Gordon [22] also conducted a similar type study in the North Atlantic Ocean

and found that particles with diameters less than 7 μm were the most numerically abundant and that there was no significant change in size distribution with ocean depth.

Krey [23] conducted a study in estuaries and found the mean spherical diameter of suspended organic particles to be between 5-6 μm. Biggs conducted a sediment size analyzer of the Chesapeake Bay and reported sediment size distributions with geometric means of approximately 25-30 μm. The significance of these example particle size distributions will become apparent when analytical modeling is considered in Chapter III.

Measurement Parameters

Physical water quality parameters refer to the appearance, taste, or odor of the water and thus are a good measure of the aesthetic quality of the water. The appearance of the water is usually measured by light scattering techniques. Most of these techniques consist of a collimated beam of light illuminating a water sample with the scattered, or transmitted light collected by a light detector which may be spectrally filtered. The intensity of scattered or transmitted light is compared with a known standard, with the results giving a quantitative measure of the appearance of the water.

Several physical subsurface water quality parameters appear suitable for measurement by the laser sensor examined in this report. These parameters include *turbidity, suspended solids,* and *transmittance,* and are discussed in the following paragraphs.

Turbidity. Turbidity is a measure of the light scattering characteristics of water caused by the presence of colloidal and suspended matter. The presence of suspended matter can indicate a change in the water quality, for example, contamination of the water sample by microorganisms or the presence of finely divided inorganic substances such as clay or silt. The determination of turbidity affords a very sensitive means of detecting the presence of suspended matter. Of some importance is the fact that the presence of suspended matter will degrade the appearance of the water. Turbidity is also undesirable for industry applications where the product is destined for human consumption, for domestic water supplies, and for other industrial applications such as pulp and paper manufacture. The turbidity of natural waters is also an important factor in the control of productivity. Turbidity interferes with the penetration of light and will affect the ecosystem since photosynthetic activity within the ecosystem is highly dependent upon light penetration.

The traditional procedure for the measurement of turbidity is the visual candle turbidimeter, usually termed the Jackson candle turbidimeter. In this method the extinction of the image of a candle flame, situated below a vertically suspended graduated tube, is observed by viewing the sample through various depths of the water. The sample tube is graduated in Jackson Turbidity Units (JTU). The lower limit of turbidity that may be measured using the Jackson candle turbidimeter is 25 JTU.

A new measurement technique for measuring turbidity termed nephelometry has been recommended by Standard Methods [25]. A nephelometer measures the intensity of scattered light at right angles to the incident collimated light beam. The measurement units of a nephelometer are Formazin Turbidity Units (FTU, where one FTU is approximately equal to one JTU) named after the standard solution which is used to calibrate the meter. The primary advantages of nephelometers are: 1) the ability to measure turbidities much less than 25 FTU; and 2) the elimination of visual judgments as required by the Jackson candle turbidimeter.

The sampling frequency for measuring the turbidity of an estuary or stream depends on how critical the quality of the water is to the particular location. However, as a general rule, if turbidity is an important

parameter, sampling should be continuous [1].

Suspended Solids. Suspended solids is a measure of the weight concentration of particulate matter in water. Although the presence of suspended solids does cause turbidity, the amount of turbidity in the water does not necessarily relate to the amount of suspended solids. The measurement of suspended solids is made by filtering a known volume of water and determining the weight difference between the clean filter and the contaminated filter. The units of suspended solids are usually mg/liter.

Transmittance. Transmittance is a measure of the light attenuation of water, and is related to the scattering and absorbing constituents in the water. Transmittance is usually measured with a spectrally filtered light source and detector, with units in percent, relative to distilled water. The importance of transmittance in ecology is similar to that of turbidity.

Oil on Water

Oil pollution has become a problem of major impact on the environment - a problem of a more pervasive and disturbing nature than the obvious detrimental effects observed on the habitat and shores. Before examining these detrimental effects, some of the general characteristics of oil pollution are discussed.

General Characteristics

Oil is not a single substance but a complicated and variable mixture of hundreds of chemical compounds. The constituents of oil share many common properties but also differ considerably in their influence on the environment [26]. Among these properties are:

1. Toxicity - Many low boiling aromatic hydrocarbons are lethal poisons to almost any organism, while some higher boiling paraffin hydrocarbons are essentially nontoxic to most forms of life. No.2 fuel oil, for example, is widely known to be extremely lethal to marine life while in general crude oils are not highly toxic [27].
2. Solubility - Petroleum derivatives in certain concentrations are soluble, while other hydrocarbons are essentially insoluble. Solubility significantly influences the toxicity of a component of oil.
3. Biodegradability - This varies widely according to the nature of the hydrocarbon with the rate of biodegradability significantly effecting the persistance of environmental effects.
4. Carcinogenity - Some components of oil are known to have cancer-inducing properties [26].

The effect of oil on the environment is not only dependent on the type of oil spilled as discussed above, but also on the amount spilled. Typical amounts of oil spills range from a few hundred barrels to hundreds of thousands of barrels, as occurred in the famous Torrey Canyon spill where 400,000 barrels of oil were spilled.

The spreading of oil from such spills largely depends on the type of oil. Pollution by light oils in the estuaries (where unfortunately most spills occur) seldom reach the shore. Rather, they dissipate quickly, particularly if disturbed by wind or waves. Small scale spills of crude oils, however, tend to move inland. In large scale crude oil spills, the oil remains in a cohesive mass and comes ashore in the form of a slick. Pollution by heavy oils tends to breakup into large lumps and, particularly in cold weather, solidifies very quickly [28].

Thicknesses of oil spills after spreading vary largely with the condition of the wind and waves. Generally, however, thicknesses for most spills range from tenths of millimeters to several millimeters.

Effect on Aquatic System

The overall effect of oil pollution on the aquatic system is best illustrated by the following oil spill example discussed by Murphy [26]. The example discussed

is the West Falmouth spill which occurred near the shores of Cape Cod in 1969 with 4,000 barrels of No. 2 fuel oil spilled. A feature of this medium size spill was a massive initial kill of area marine life, in accordance with the nature of most spills of this type. Most of the spill dispersed into the sea after two days, resulting in a persistence of oil on the ocean floor which expanded to cover 50 hectacres (more than 1 acre per original barrel of oil spilled). As the spill expanded on the ocean floor, the mortality to bottom life increased significantly. The kill of marsh plants and bottom organisms apparently changed the physical properties of the sediments and may have caused erosion and spreading of the trapped oil. Another feature of this oil spill was the tainting of the flesh of commercial fish and shellfish, which has been one of the oldest and most frequent complaints of oil pollution.

The effects of oil spills on the aquatic system vary for different oil spills. However, the West Falmouth spill is described as a typical oil spill and is considered to be representative of the impact of oil pollution on the aquatic system.

CHAPTER III

ANALYTICAL MODEL FOR LASER BACKSCATTER

Many investigations have been conducted to determine an analytical model for describing backscatter from a volume of scatterers. Some investigations have presented single scatter Mie models to describe the backscatter, however, numerous laboratory measurements with spherical scatterers illuminated by a polarized light source have shown a significant amount of depolarization of the backscattered energy, which suggests the presence of multiple scatter within the volume. While several subsurface multiple scatter models have been investigated for describing backscatter from a volume of scatterers [29], [30], these models assume that the backscattered energy is randomly polarized, that is, the backscattered electric field has no preferred polarization (For a comparison of these scattering models, see Rouse [31]). Measurements from cast dielectric samples and turbid water reported by Wilhelmi [18], however, show large like polarized (relative to cross polarized) returns, which suggests the presence of single scatter within the volume. This chapter presents the development of a volumetric backscatter model which incorporates both a single scatter return and a multiple scatter return from an aqueous suspension of

scatterers illuminated by a polarized electromagnetic plane wave. These results are then extended to include the effect on the backscatter of a layer of oil on the turbid water.

Turbid Water

Approach

The following approach will be taken in developing the volumetric backscatter model. A linearly polarized electromagnetic plane wave is incident upon a smooth surface volume containing spherical scatterers (Figure III-1). Since the backscatter from a smooth surface can be assumed negligible for optical frequencies [18], these effects will not be considered. The backscatter from the subsurface will consist of two components: a like polarized return and a cross depolarized return. The like polarized return (P_{vv} or P_{hh}, where the first subscript indicates transmitter polarization, vertical or horizontal, and the second subscript indicates receiver polarization) consists of a single scatter return (denoted by superscript s) plus a multiple scatter return (denoted by superscript m). Thus,

$$P_{vv} = P_{vv}^{s} + P_{vv}^{m} \qquad \text{(III-1)}$$

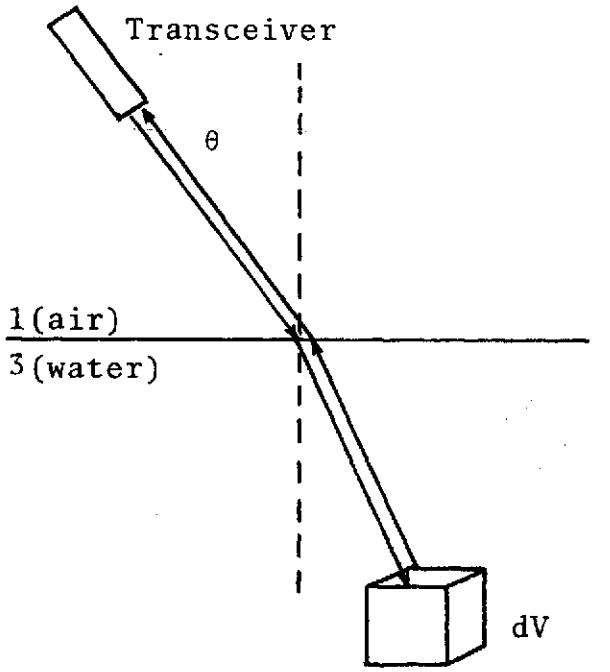

Figure III-1. Scattering Geometry

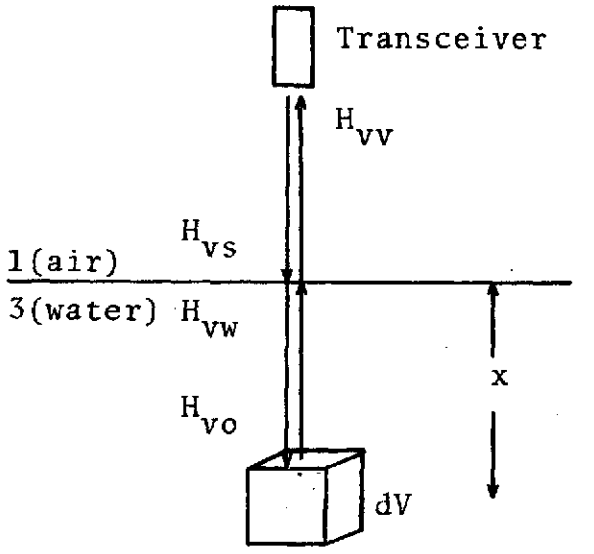

Figure III-2. Simplified Scattering Geometry

$$P_{hh} = P_{hh}^{s} + P_{hh}^{m} \qquad \text{(III-2)}$$

The cross depolarized return (P_{vh} or P_{hv}) from spherical scatterers consists only of a multiple scatter return or

$$P_{vh} = P_{vh}^{m} \qquad \text{(III-3)}$$

$$P_{hv} = P_{hv}^{m} \qquad \text{(III-4)}$$

The following sections develop this model for single scatter return and the multiple scatter return.

Single Scatter Model

Assuming a vertically polarized, monochromatic plane wave incident upon a smooth surface volume of water and considering the simplified geometry shown in Figure III-2 (since the incidence angle θ shown in Figure III-1 effects only the transmission coefficients), the irradiance H_{vs} at the top surface of the water is

$$H_{vs} = P_t / A_s$$

where P_t is the power transmitted (assuming lossless transmission) and A_s is the area of illumination at the surface of the water. The portion of the irradiance H_{vw} transmitted into the water is

$$H_{vw} = \left(T_{13}^{v}\right) H_{vs}$$

where T_{13}^{v} is the Fresnel power transmission coefficient for vertical polarization for propagation from medium 1 (air) to medium 3 (water).

Due to the attenuation of the beam through the volume (due to scattering and absorption by the scatterers), the irradiance H_{vo} on a differential element within the volume is

$$H_{vo} = H_{vw} \exp(-\beta x)$$

where β is the volume extinction coefficient and x is the distance from the surface to the differential volume. The volume extinction coefficient is defined by van de Hulst [32] as

$$\beta = \int Q_{ext}(a) N(a) \pi a^2 da \qquad \text{(III-5)}$$

where $Q_{ext}(a)$ is the efficiency factor for scattering and absorption (polarization independent for spherical particles), and N(a)da is the number of particles per unit volume with radii a in the interval da. For a suspension

of particles with a broad size distribution (polydisperse), it is advantageous to express the volume extinction coefficient in terms of the total number of particles per unit volume by defining

$$N(a)da = Nr(a)da$$

where N is the total number of particles per unit volume and r(a)da is the relative number of particles per unit volume with radii a in the interval da. Equation (III-5) can then be written as

$$\beta = N \int Q_{ext}(a)\pi a^2 r(a)da$$

Using this equation to calculate β requires only one numerical evaluation of the integral expression for different particle concentrations. Defining this integral to be β_r gives

$$\beta = N\beta_r \qquad \text{(III-6)}$$

For a suspension of particles with a very narrow size distribution (monodisperse), the volume extinction coefficient is simply

$$\beta = Q_{ext} N \pi a^2$$

The general relationship for the irradiance scattered from a volume dV in the direction ψ is

$$dH = H_o F(\psi) dV / r^2$$

where $F(\psi)$ is the scattering function, which in general is related to the polarization state, relative particle size distribution, particle orientation, and particle concentration [32]; ψ is the scattering angle measured from the direction of the incident wave; r is the distance from the differential volume to the point of observation; and H_o is the incident irradiance. The scattering function for backscatter ($\psi=\pi$) from spheres is the same for each of the plane polarized components of incident radiations, so that it is not necessary to designate the polarization of the scattering function [33]. If the relative size distribution is used to calculate the scattering function $F(\pi)$, then $F(\pi)$ can be given by

$$F(\pi) = N F_r(\pi) \qquad \text{(III-7)}$$

where $F_r(\pi)$ is the scattering function calculated from the relative particle size distribution.

Assuming that the distance R >> x (Figure III-2, p.25) as is the case for most applications, the distance r can be

approximated by R. The irradiance backscattered from a volume dV is then

$$dH_{VV} = P_t \frac{(T_{13}^V T_{31}^V)}{A_S R^2} N F_r(\pi) \exp(-2N\beta_r x)\, dV \qquad \text{(III-8)}$$

where T_{31}^V is the Fresnel transmission coefficient for vertical polarization for propagation from medium 3 to medium 1. Since single scattering is assumed, the volume element dV must be within the boundaries of the incident beam and can thus be represented as

$$dV = A_S dx$$

Substituting this equation into (III-8) and confining the limit of integration on x to be the depth L along the beam gives

$$\int_0^{H_{VV}} dH_{VV} = P_t \frac{(T_{13}^V T_{31}^V)}{R^2} N F_r(\pi) \int_0^L \exp(-2N\beta_r x)\, dx$$

which after integrating gives

$$H_{VV} = \frac{P_t (T_{13}^V T_{31}^V)}{R^2} \frac{F_r(\pi)(1 - \exp(-2N\beta_r L))}{2\beta_r}$$

The single scattered power P_{VV}^{S} collected by a receiver of area A_r is then

$$P_{VV}^{S} = \frac{P_t A_r \eta (T_{13}^{V} T_{31}^{V})}{R^2} \frac{F_r(\pi)(1 - \exp(-2N\beta_r L))}{2\beta_r} \quad \text{(III-9)}$$

where the factor η is a system constant to correct for the efficiency of the optical components and the calibration of the system.

It is appropriate at this point, to define for the single scatter model an effective volume reflection coefficient γ^S. Observing (III-9), the terms which describe the scattering media in terms of its scattering properties are the scattering function $F_r(\pi)$ and the volume extinction coefficient β_r. The combination of the scattering function and the volume extinction coefficient derived through the integration process represents the fraction of the incident energy which is single scattered to the receiver. This fraction of energy will be defined to be the single scatter volume reflection coefficient γ^S which for vertical transmit polarization is given by

$$\gamma_{VV}^{S} = \frac{F_r(\pi)(1 - \exp(-2N\beta_r L))}{2\beta_r} \quad \text{(III-10)}$$

Several observations can be made about (III-10) concerning the magnitude of the volume reflection coefficient

relative to the mean depth L and the volume extinction coefficient. Representing the exponential in (III-10) in a series expansion gives

$$\exp(-2N\beta_r L) = 1 - 2N\beta_r L + \frac{(2N\beta_r L)^2}{2!} + \ldots\ldots$$

Assuming that $N\beta_r L << 1$ (or that the mean depth is much smaller than the extinction length, $1/N\beta_r$) gives

$$\exp(-2N\beta_r L) \approx 1 - 2N\beta_r L$$

Substituting this expression into (III-10) gives

$$\gamma_{vv}^{s} \approx F_r(\pi) NL \qquad \text{(III-11)}$$

which shows that at very low particle concentrations, the single scatter return is proportional to the particle concentration (consistent with single scatter theory).

Considering the case where $N\beta_r L >> 3$ (or that the extinction length is 3 times smaller than the mean depth L), the single scatter volume reflection coefficient is approximated by

$$\gamma_{vv}^{s} \approx F_r(\pi) / 2\beta_r \qquad \text{(III-12)}$$

which shows that the single scatter return is independent of particle concentration.

For the case of $N\beta_r L \simeq 1$, (III-10) must be used.

Multiple Scatter Model

Several assumptions concerning the nature of the multiple scatter mechanism will be made in considering an analytical model for multiple scatter within the volume. First, no attempt will be made to provide a physical model of the multiple scatter mechanism. Instead, the more general approach is used by assuming that the backscatter from a multiple scattered wave exists which is some fraction of the incident field. Furthermore, the scattering media is assumed to be bounded by a smooth surface.

Following the same procedure for the multiple scatter case as for single scatter and noting that the multiple scatter term should be of the same form as (III-9), a volume reflection coefficient γ_{vv}^{m} is used to represent the fraction of the backscattered energy which is like-polarized multiple scatter. The backscattered power for this case can then be given as

$$P_{vv}^{m} = \frac{P_t A_r}{R^2} \left(T_{13}^{V} T_{31}^{V} \right) \eta \gamma_{vv}^{m} \qquad \text{(III-13)}$$

Realizing that due to multiple scatter there is a significant amount of energy contained within the cross polarized component, the same procedure is followed by defining a volume reflection coefficient γ_{vh}^{m}. The volume reflection coefficient is treated as a tensor to account for any polarization dependency of the particle scattering within the media. The cross polarized power can then be given as

$$P_{vh}^{m} = \frac{P_t A_r (T_{13}^{v} T_{31}^{h})}{R^2} \eta \gamma_{vh}^{m} \qquad \text{(III-14)}$$

Note that the transmission coefficient for the cross term contains the term T_{31}^{h}, which accounts for the cross polarized transmission from media 3 to 1.

An important observation concerning the previous developments is that the effective volume reflection coefficient for the single scatter term is given in terms of the physical scattering properties of the medium, that is, in terms of the scattering function and extinction coefficient. The volume reflection coefficient for the multiple scatter process, however, is not given in terms of the media properties and must then be determined empirically or analytically by another approach.

Results

The model describing the backscatter from a suspension of spherical particles bounded by a smooth surface and illuminated by a vertically polarized plane wave, can be obtained in terms of the like polarized components and cross polarized components as

$$P_{vv} = \frac{P_t A_r}{R^2}(T_{13}^v T_{31}^v)\ \eta(\gamma_{vv}^s + \gamma_{vv}^m) \qquad \text{(III-15)}$$

$$P_{vh} = \frac{P_t A_r}{R^2}(T_{13}^v T_{31}^h)\ \eta\gamma_{vh}^m \qquad \text{(III-16)}$$

Similarly, for horizontal transmit polarization the like and cross components are

$$P_{hh} = \frac{P_t A_r}{R^2}(T_{13}^h T_{31}^h)\ \eta(\gamma_{hh}^s + \gamma_{hh}^m) \qquad \text{(III-17)}$$

$$P_{hv} = \frac{P_t A_r}{R^2}(T_{13}^h T_{31}^v)\ \eta\gamma_{hv}^m \qquad \text{(III-18)}$$

Oil on Water

Approach

Oil on turbid water can be described as a laterally inhomogeneous, isotropic, lossy dielectric. (It is assumed that the oil is homogeneous with depth, that is, the index of refraction of the oil is not a function of oil depth.) The effect of oil on water is twofold: 1) the difference in the index of refraction of oil relative to water alters the transmission coefficients at the air/oil boundary; and 2) the lossy properties of the oil results in attenuation of the energy transmitted through the oil. The following sections extend the turbid water model developed in the previous section to include these two effects of oil on water.

Transmission Coefficients

The effect of a layer of oil on water is diagrammed in Figure III-3. Medium 2 can be described as a dielectric mixture of oil and water since the oil is not laterally homogeneous. To consider this inhomogeneity, an effective index of refraction of the oil and water mixture is used by weighting each index of refraction by the fractional areal coverage of oil. Defining this fraction of areal coverage to be ρ, the effective index of refraction

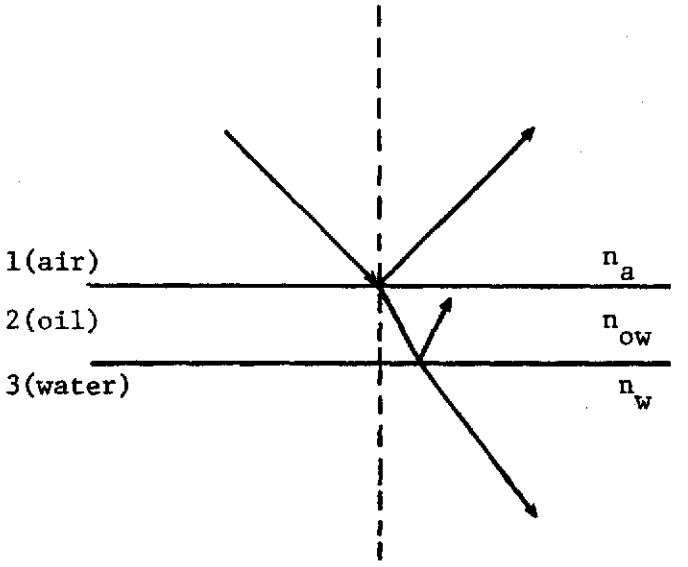

Figure III-3. Diagram for a Layer of Oil on Water

n_{ow} of the oil and water mixture can be given in terms of the relative indices of refraction of oil n_o and water n_w as

$$n_{ow} = \rho n_o + (1 - \rho) n_w \qquad \text{(III-19)}$$

To account for the transmission of energy across boundaries 1-2 and 2-3 requires the use of two transmission coefficients. Two more transmission coefficients are then required to account for the transmission of energy out of the water volume and across boundary 2-1.

Attenuation

The second and more profound effect on the backscatter from oil on water is the two way attenuation characteristic which reduces the backscattered power exponentially with respect to the oil thickness and the oil extinction coefficient. Expressing this effect analytically and including the boundary transmission effect, the results of the turbid water model are modified by

$$P_{VV}^{O} = \frac{(T_{12}^{V} T_{23}^{V} T_{32}^{V} T_{21}^{V})}{(T_{13}^{V} T_{31}^{V})} \exp(-2\alpha t) P_{VV} \qquad \text{(III-20)}$$

and

$$P_{vh}^{o} = \frac{(T_{12}^{v} T_{23}^{v} T_{32}^{h} T_{21}^{h}) \exp(-2\alpha t) P_{vh}}{(T_{13}^{v} T_{31}^{h})} \qquad \text{(III-21)}$$

where P_{vv} and P_{vh} are the subsurface backscattered powers in the absence of oil, given in (III-15) and (III-16); the T_{ij}^{x}'s are the Fresnel transmission coefficients where the superscript x represents the polarization and the subscripts represent from medium i to medium j; α is the effective extinction coefficient (function of oil type and wavelength); and t is the oil thickness. The transmission coefficients in the denominator normalize P_{vv} and P_{vh} to cancel the air to water transmission coefficients observed in (III-15) and (III-16). The effective extinction coefficient can be expressed in terms of the extinction coefficient α_h for a homogeneous oil layer by the fractional cover ρ as

$$\alpha = \alpha_h \rho \qquad \text{(III-22)}$$

Since the oil on water model includes the use of an effective refractive index and extinction coefficient, one primary restriction of the applicability of model is that a long term time average of the return signal and/or a large spatial average of the surface must be used so

that the effective coefficients mentioned above are applicable to the measurement situation.

CHAPTER IV

LIDAR POLARIMETER

The sensor used in this investigation was a dual polarization laser backscatter system termed a lidar polarimeter. This chapter describes the system components [16] and the transceiver configuration of the lidar polarimeter.

System Description

The lidar polarimeter transmits a linearly polarized laser beam and receives both the vertical and horizontal polarized backscattered energy. This section describes the system components which perform this task.

Transceiver

The transmitter of the lidar polarimeter (See Figures IV-1 and IV-2) is a 5 mw, helium-neon, cw laser (Spectra Physics Model 120) provided with a Spectra Physics broadband polarization rotator attached to the laser output. The polarization rotator allows variation of the transmitter polarization. The transmitted laser beam is modulated by a Princeton Applied Research (PAR) rotary, light chopper to allow detection insensitivity to ambient radiation (See Detection Electronics).

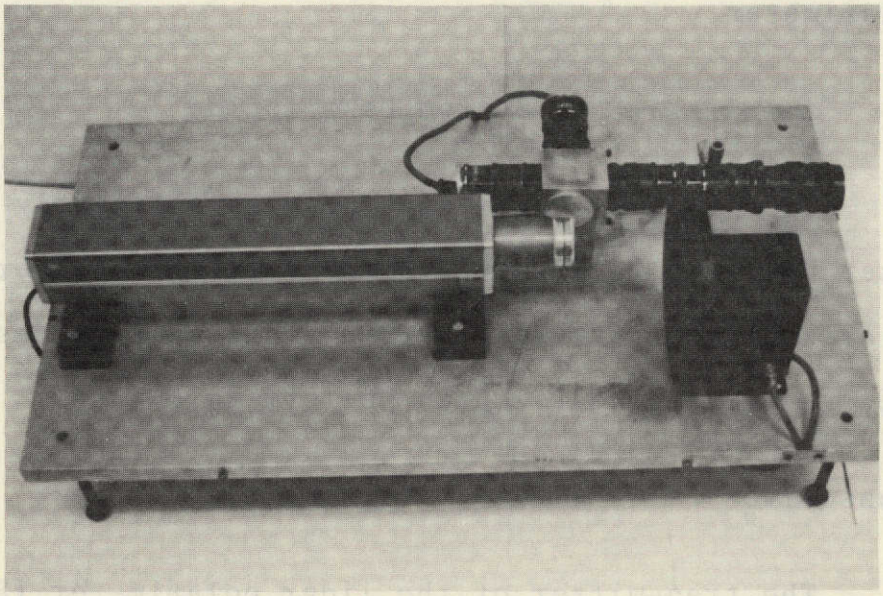

Figure IV-1. Lidar Polarimeter Transceiver

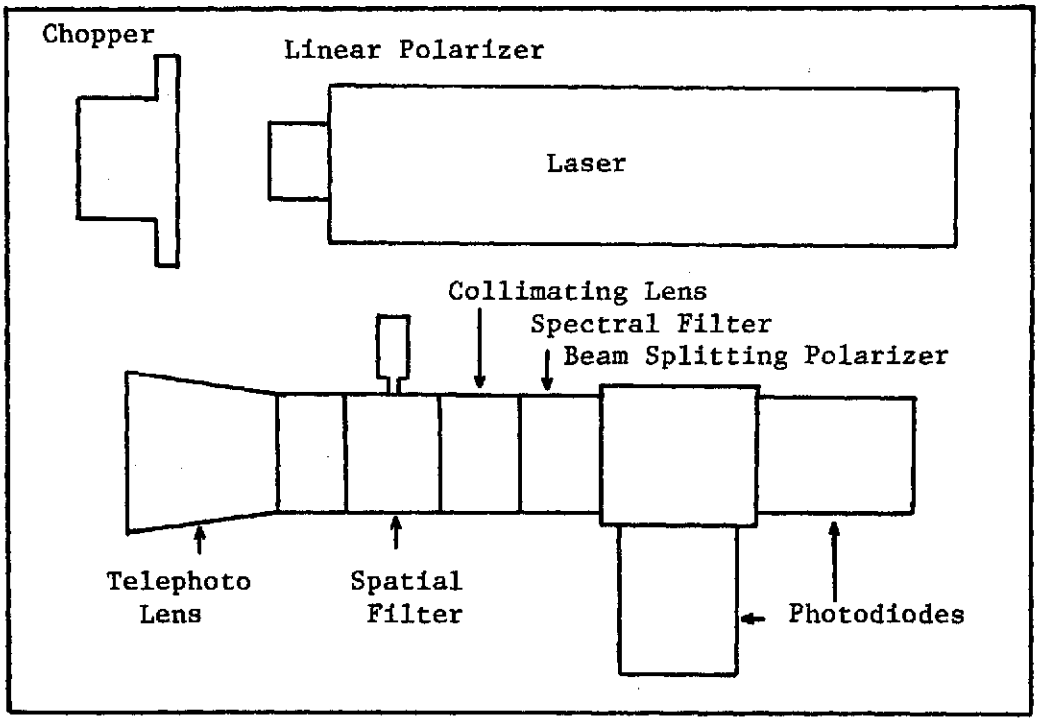

Figure IV-2. Schematic Diagram of Lidar Polarimeter

The receiver of the lidar polarimeter includes several separate standard photographic extension tubes mated with a Vivitar 135 mm f/3.5 telephoto camera lens. The extension tubes house several optical components. A Jodon pinhole assembly located in the focal plane of the collecting lens provides a narrow receiver field of view, with fine adjustment of direction. A five centimeter focal length lens recollimates the spatially filtered return before passing through a narrow band spectral filter. A Spectra Physics 2.5 centimeter beam-splitting polarizer cube is located inside an aluminum box assembly with ports threaded to fit the extension tubes. The horizontal and vertical polarization components are detected by separate United Detector Model 500 photodiode/op-amp combination detectors mounted in extension tubes. The characteristics of the transceiver section are summarized in Table IV-1.

The transceiver was mounted on a 19" x 34" x 1" aluminum plate. To allow field portability, the plate was then mounted to a heavy duty Majestic instrument tripod (Model T-114) with a rotatable head (Model H120). The rotatable head allows continuous tilt from straight down to 180° up. A Davis Sanford tripod dolly Model DS-69 was used to aid in sensor mobility. A metal hood enclosing the transceiver section assures protection during

Table IV-1. Lidar Polarimeter Specifications

Power Transmitted	6 mw @ 633 nm
Minimum Detectable Polarization Ratio	1:200
Receiver Aperture	38 mm
Spectral Filter Bandwidth	3 nm @ 633 nm
Beam Divergence	1.7 milliradians
Voltage Responsivity	5 μv/pw
RMS Noise Deviation	
(1 sec integration time)	10 μv
(30 sec integration time)	2 μv

transit and inclement weather. Figure IV-3 shows a photograph of the transceiver package.

Detection Electronics

The modulated signals from the photodiodes are synchronously detected with a PAR Model 124 lockin amplifier, to avoid DC drift, low frequency noise, and ambient radiation interference. Measurements with the lockin amplifier showed an rms noise deviation of approximately 10 μv with a 1 second integration time, and 2 μv with a 30 second integration time.

The lockin amplifier was housed in a central control unit along with the laser power supply and photodiode power supply. A description and diagram of the lidar polarimeter electronics are given in Appendix A. Figure IV-4 shows the complete lidar polarimeter system.

Transceiver Configuration

The bistatic nature of the lidar polarimeter requires special considerations. Since the receiver is not on axis with the transmitter, an intersection region is created at the point where the field of view and transmitted beam intersect. Figure IV-5 diagrams this effect.

The depth of the intersection region can be estimated by the following procedure. The angle ϕ between

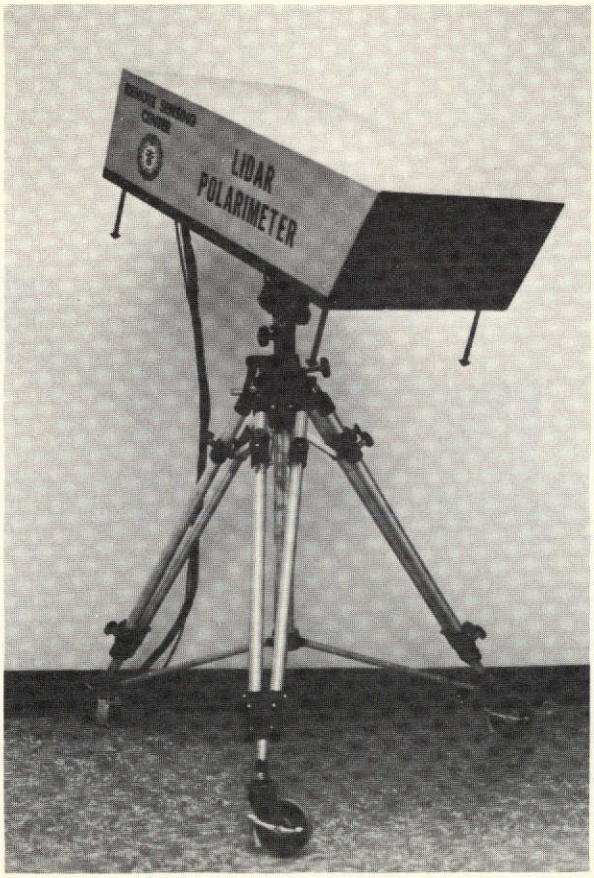

Figure IV-3. Lidar Polarimeter Transceiver Package

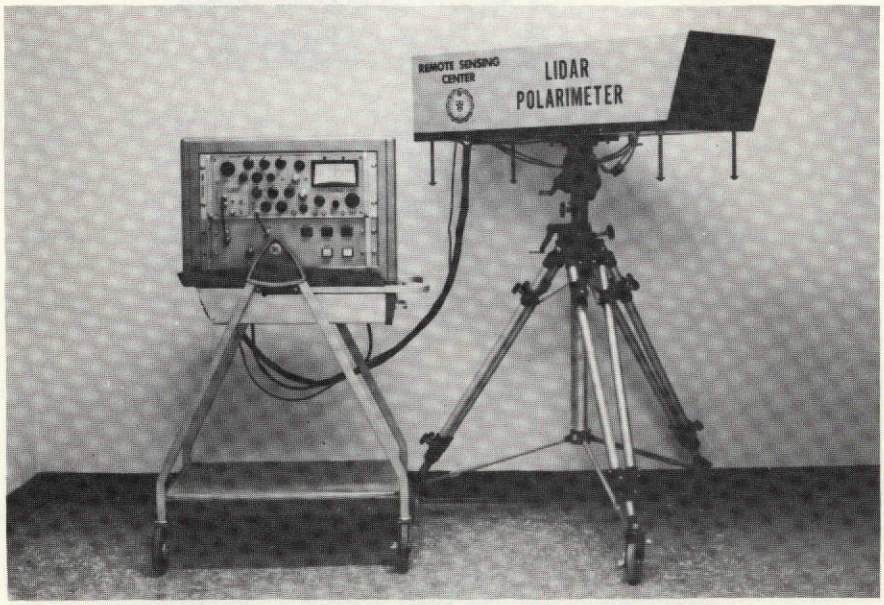

Figure IV-4. Complete Lidar Polarimeter System

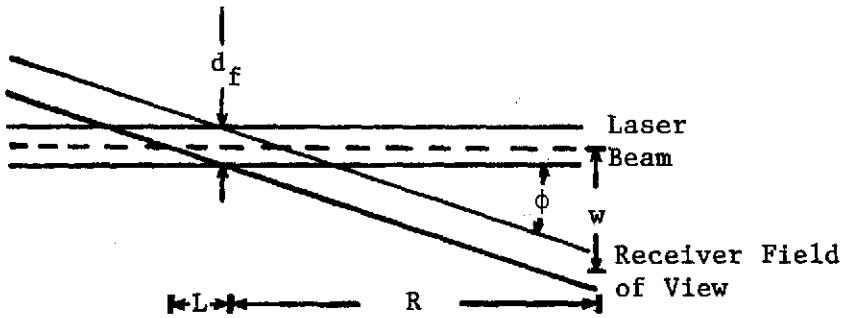

Figure IV-5. Diagram of Bistatic Lidar Measurement Volume

the receiver and transmitter is approximated by

$$\phi \approx \frac{w}{R}$$

assuming that R >> w, where w is the separation distance between the transmitter and the receiver, and R is the slant range to the surface of the target. Observing the geometry of the intersection region and assuming that R >> d_f shows that the mean depth L is given by

or

$$L \approx \frac{d_f}{2\phi}$$

$$L \approx \frac{d_f R}{2 w} \qquad \text{(IV-1)}$$

where d_f represents the diameter of the field of view at the surface of the target. Using the ray optics approach, the diameter of the field of view at the surface can be given in terms of the diameter of the receiver spatial filter (pinhole) d_{ph} by

$$d_f = \frac{d_{ph} R}{F}$$

where F is the focal length of the collecting lens.

Substituting this expression into (IV-1) gives

$$L = \frac{d_{ph} R^2}{2 w F} \qquad \text{(IV-2)}$$

Another system parameter which will be needed in later developments is the diameter of the laser beam d_L at the surface of the target. For the laser used in the experiments, d_L is approximated in terms of the range in meters and the beam divergence (1.7 milliradians) as

$$d_L \approx .001 + .0017R$$

The area of illumination (m^2) can then be given by

$$A_L = \frac{\pi}{4}(.001 + .0017R)^2 \qquad \text{(IV-3)}$$

CHAPTER V

EXPERIMENTS

Several laboratory turbid water experiments were conducted with the lidar polarimeter to determine the validity of the scattering model developed in Chapter III and to better understand the nature of the scattering mechanism. Several field experiments along natural waterways were conducted with the lidar polarimeter to determine the applicability of the laser sensor for determining subsurface water quality parameters. Laboratory oil on water experiments were also conducted to determine the validity of the oil on water scattering model and to demonstrate the scattering phenomenas involved so that a procedure could be presented for characterizing oil pollution with respect to oil type and oil thickness. This chapter describes these experiments.

Turbid Water

Achieving the objectives of the laboratory turbid water experiments required varying several parameters. These include: 1) varying the suspended particle concentration from very low concentrations where single scatter should be dominant to very high concentrations where multiple scatter should be dominant; 2) varying the receiver

field of view to determine the dependency of the depolarization on the scattering volume viewed by the receiver; 3) varying the transmitter polarization; and 4) varying the absorption losses of the water medium to determine the effect on the depolarization.

The first experiments included measuring P_{vv} and P_{vh} and varying 1) the suspended particle concentration (number of particles, N',/mL) from 1.75 X 10^6 to 2.03 X 10^{11}, and 2) the diameter of the receiver field of view at the surface from .32 cm to 1.07 cm. The suspended particles used for these measurements were relatively monodispersive polystyrene latex spheres (Dow Plastic Pigment 722) with a known refractive index (1.59) and particle size distribution (Figures V-1 and V-2) [34]. The field of view was varied by changing the spatial filter diameter from .3 mm to 1 mm. A second set of backscatter measurements with a constant field of view (.64 cm) were made by varying the suspended particle concentration using a relatively polydispersive polytetrafluoroethylene resin dispersion ("Teflon" TFE 30 dispersion manufactured by E. I. Dupont Nemours and Co.). This dispersion consisted of spherical particles with a refractive index of 1.37 and diameters in the range .04 μm to .4 μm (Figures V-3 and V-4) [35]. This second measurement also included measuring not only P_{vv} and P_{vh} but also P_{hh} and P_{hv}.

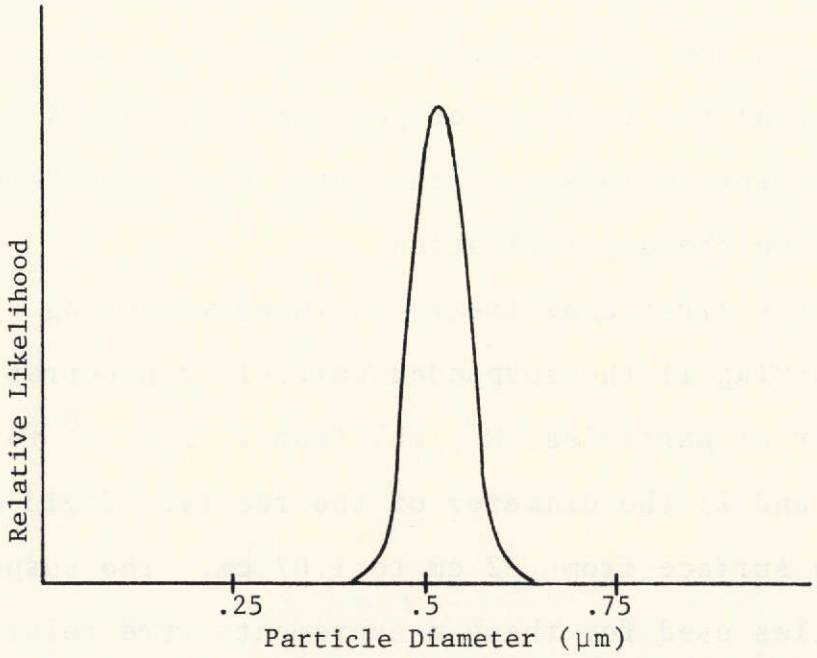

Figure V-1. Approximate Relative Size Distribution for Dow Plastic Pigment 722

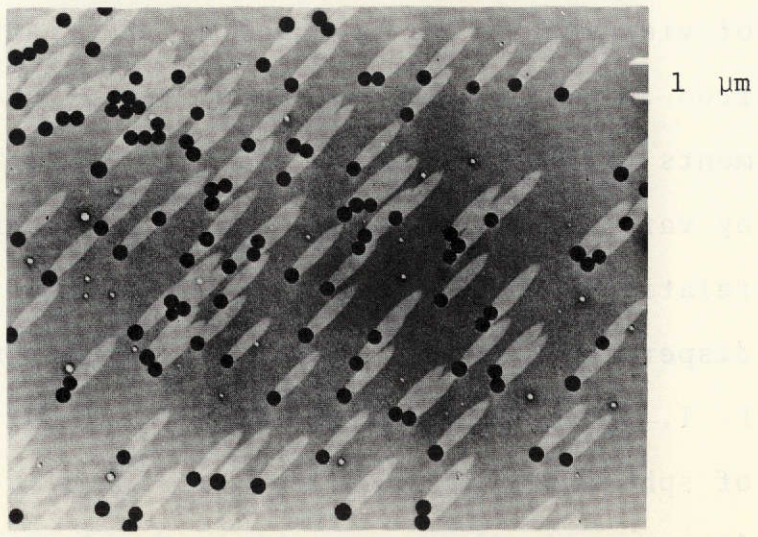

Figure V-2. Photomicrograph of Dow Plastic Pigment 722

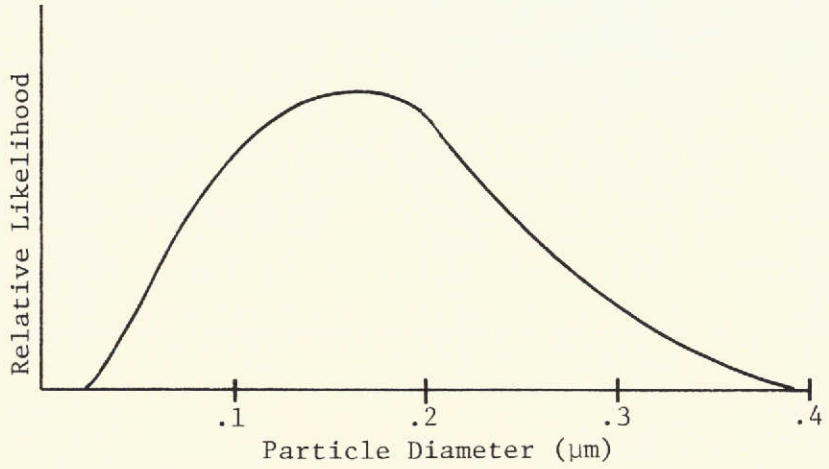

Figure V-3. Approximate Relative Size Distribution for Dupont TFE 30

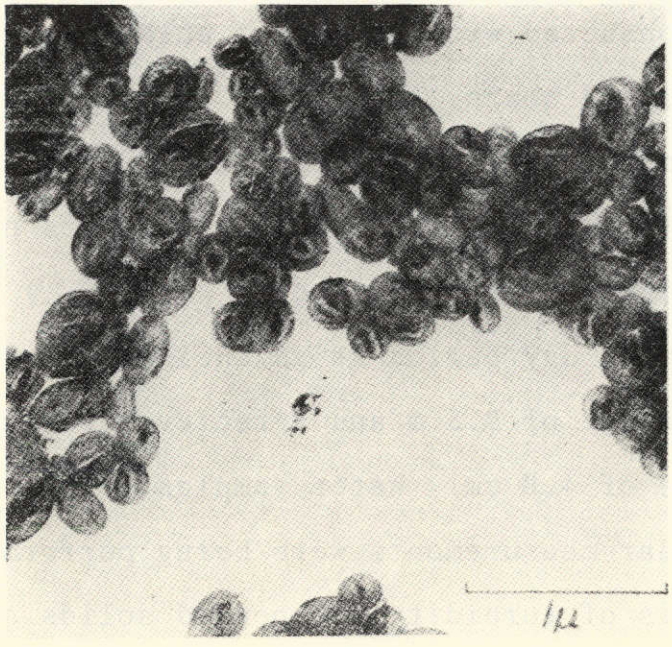

Figure V-4. Photomicrograph of Dupont TFE 30

The last turbid water experiment included measuring P_{vv} and P_{vh} from a constant scattering concentration (using polystyrene latex particles with a concentration of 4.37 X 10^9 N'/mL) and a constant field of view (.64 cm) with a varying absorbent concentration of the water medium. The absorbent used for this experiment was black nigrosine dye. Dye concentrations ranged from 0.0 to 214.0 mg/L. All data collected in these experiments along with values for the system parameters are listed in Appendix B.

Natural Waterways

Several field experiments from natural waterways were conducted with the lidar polarimeter from atop bridges and boats. The first significant field experiment was conducted from a bridge on the Brazos River at Waco, Texas (Figure V-5). Lidar measurements of P_{vv} and P_{vh} (also a few measurements of P_{hh} and P_{hv}) were recorded over a two day period at an incidence angle of 30°, a slant range of 9.5 m and a reciever field of view at the surface of 4.8 cm. Water samples were collected while the lidar measurements were being performed so that an analysis of turbidity, suspended solids and transmittance could be performed for each sample. Special care was taken to inhibit physical or chemical alteration of the

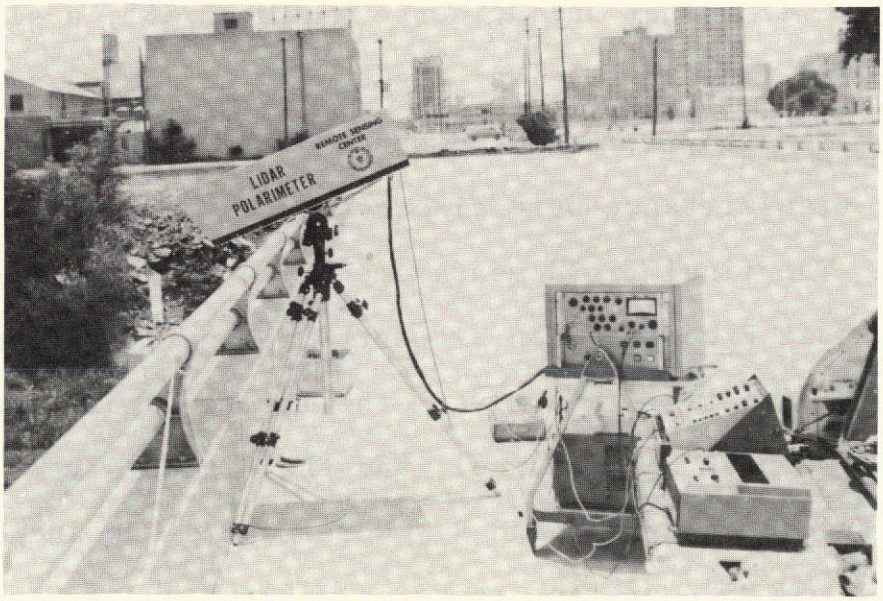

Figure V-5. Experimental Set Up On
Brazos River Bridge

water impurities. A twenty minute time history of the like polarized return was recorded with a Hewlett-Packard 7004-B X-Y Recorder.

The second field experiment was conducted from the boat Excellence on an eight mile stretch along the Houston Ship Channel (Figure V-6). Lidar measurements of P_{vv} and P_{vh} were made at an incidence angle of 35°, a slant range of 2.84 m and a receiver field of view at the surface of approximately 1.25 cm. Ground observations of turbidity and transmittance were also recorded.

The final field measurement was conducted again on the boat Excellence on a twenty mile stretch along three interconnecting waterways: the Intercoastal Waterway, the Freeport Ship Channel, and the Brazos River. Lidar measurements of P_{vv} and P_{vh} were made at an incidence angle of 35°, a slant range of 2.84 m, and a receiver field of view at the surface of approximately 1.25 cm. Ground observations of turbidity, suspended solids, and transmittance were performed. Data for these field measurements are given in Appendix B.

Oil on Water

The objectives of the oil on water experiments included demonstrating four concepts: 1) oil on water attenuates the energy backscattered to the receiver; 2) the

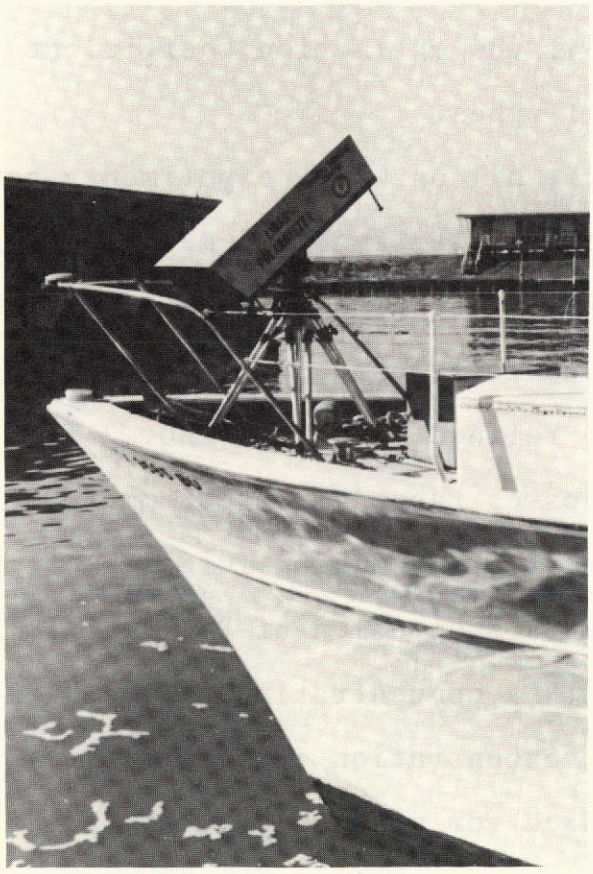

Figure V-6. Experimental Set Up Aboard The Boat Excellence

presence of oil on water does not significantly alter the subsurface depolarization ratio; 3) the extinction coefficient of a specific oil type is a function of the wavelength; and 4) the extinction coefficient varies for different oil types.

The first oil on water experiment conducted with the lidar polarimeter included measuring P_{vv} and P_{vh} and varying the oil thickness for different test oils. The test oils used for these experiments were gasoline, kerosene, SAE 30 refined motor oil, no. 2 fuel oil, and crude oil. Thicknesses ranged from .05 mm to 5.5 mm. The subsurface scattering medium for all test oils except crude oil was a suspension of Dow Plastic Pigment 722 particles with a concentration of 1.75×10^9 N'/mL. A much higher concentration of scatterers (3.97×10^{10} N'/mL) was used for crude oil because of its ultra-absorptive characteristic. All lidar data are listed in Appendix B.

Approximate values of the extinction coefficients for the different test oils were determined experimentally or from previous work [36] for laser wavelengths of .6328 μm and .4416 μm. Experimental values for the extinction coefficients were obtained by measuring the attenuation of laser light through a 1 mm wide glass sample cell containing the different test oils and then

calculating the values from the exponential attenuation formula $e^{-\alpha t}$.

CHAPTER VI

RESULTS

The previous chapters have investigated, analytically and experimentally, the problem of explaining the backscatter from turbid water and oil on turbid water. Chapter III presented the development for backscatter from turbid water considering both single scatter and multiple scatter effects. The last section of Chapter III extended these results to include the effect on the backscatter of a layer of oil on the turbid water, considering the refractive index change and attenuation due to the presence of oil. Chapters IV and V described the laboratory and field experiments which were conducted to: 1) determine the validity of the turbid water and oil on turbid water scattering models; 2) obtain a better understanding of the nature of the scattering phenomena; and 3) determine the applicability of a lidar polarimeter for remote measurements of subsurface water quality parameters and oil on water. This chapter describes the results of the investigation by analyzing the turbid water data, the natural waterway data, and the oil on water data, and comparing these results with the analytical models.

Turbid Water

Chapter III presented the development of an analytical model for backscatter from smooth surfaced, turbid water by modeling the like polarized return as an incoherent sum of a single scatter term, (III-9), and a multiple scatter term, (III-13), where the single scatter term could be uniquely determined from the characteristics of the scattering medium. The analytical model for the cross polarized return consisted only of a multiple scatter term, represented by (III-14). This section first considers the validity of the single scatter term by examining the like-polarized returns from an aqueous suspension having low particle concentrations, where single scatter should be the dominant scattering mechanism. This section then considers the behavior of the entire analytical turbid water model (represented by (III-15) and (III-16) by comparing the relative magnitudes of the like-polarized volume reflection coefficients (γ_{vv}^{s} and γ_{vv}^{m}), and the cross polarized volume reflection coefficients (γ_{vh}^{m}) as a function of particle concentration. The results of this comparison will show that at low particle concentrations single scatter is the dominant scattering mechanism (γ_{vv}^{s} is much greater than γ_{vh}^{m}), and that at very high particle concentrations, multiple scatter is the dominant scattering mechanism

(γ_{vv}^{m} and γ_{vh}^{m} are much greater than γ_{vv}^{s}).

Finally, this section discusses several characteristics of measured backscatter that were observed from variations of particle concentration, receiver field of view, transmitter polarization, and aqueous absorbent concentration.

Comparison With Analytical Model

In examining the validity of the smooth surfaced, turbid water model developed in Chapter III, the subsurface single scatter term of (III-15) is first considered. Theoretical values of single scatter return were computed for varying polystyrene latex particle concentrations and fields of view using (III-9). The system parameters used for these calculations are given in Table VI-1 and Appendix B. The relative scattering function, $F_r(\pi)$, for the latex particles was calculated using an IBM 360 computer routine developed by Adams [37]. The relative volume extinction coefficient, β_r, was obtained experimentally by measuring the attenuation of laser light through very dilute concentrations of latex particles (dilute concentrations were imperative for this parameter determination to insure measurement of single scatter attenuation only). The value of β_r was not determined analytically because the imaginary part of the refractive index was not known and calculations

Table VI-1. Several Parameters Used for Comutations in Single Scatter Model

Power Transmitted	2 mw RMS
Optical Efficiency	.5
Area of Receiver	11.3 cm^2

Table VI-2. Scattering and Extinction Coefficients for Polystyrene Latex and Teflon Particles

	Polystyrene Latex	Teflon
Relative Scattering Function ($F_r(\pi)$) (cm^2/particle)	1.033×10^{-12}	1.163×10^{-15}
Relative Extinction Coefficient (β_r) (cm^2/grams)	18219.	81.9

by Kerker [33] show that the magnitude of the extinction cross section (or equivalently β_r) is highly dependent upon the imaginary part of the refractive index.

Theoretical values of single scatter return were also computed for an aqueous suspension having varying concentrations of teflon particles. The value of $F_r(\pi)$ was determined empirically by a data fit in the low range of particle concentration. The value of β_r was determined by attenuation measurements, as discussed previously. The values of these coefficients for the latex particles and the teflon particles are given in Table VI-2. The relative scattering function and extinction coefficient for an average sized latex particle is several orders of magnitude greater than the coefficients for an average sized teflon particle. Figures V-1 (p. 54) and V-3 (p. 55) show that the mean size of the latex particles is several times larger than the mean size of the teflon particles. Since it is well known that larger particles scatter much more incident radiation than do smaller particles, the values for these coefficients appear reasonable.

Employing these coefficients in (III-9), the theoretical and experimental values of like polarized single scatter return were plotted as a function of latex particle concentration (Figure VI-1) and teflon particle concentration (Figure VI-2). Figures VI-1 and VI-2 indicate

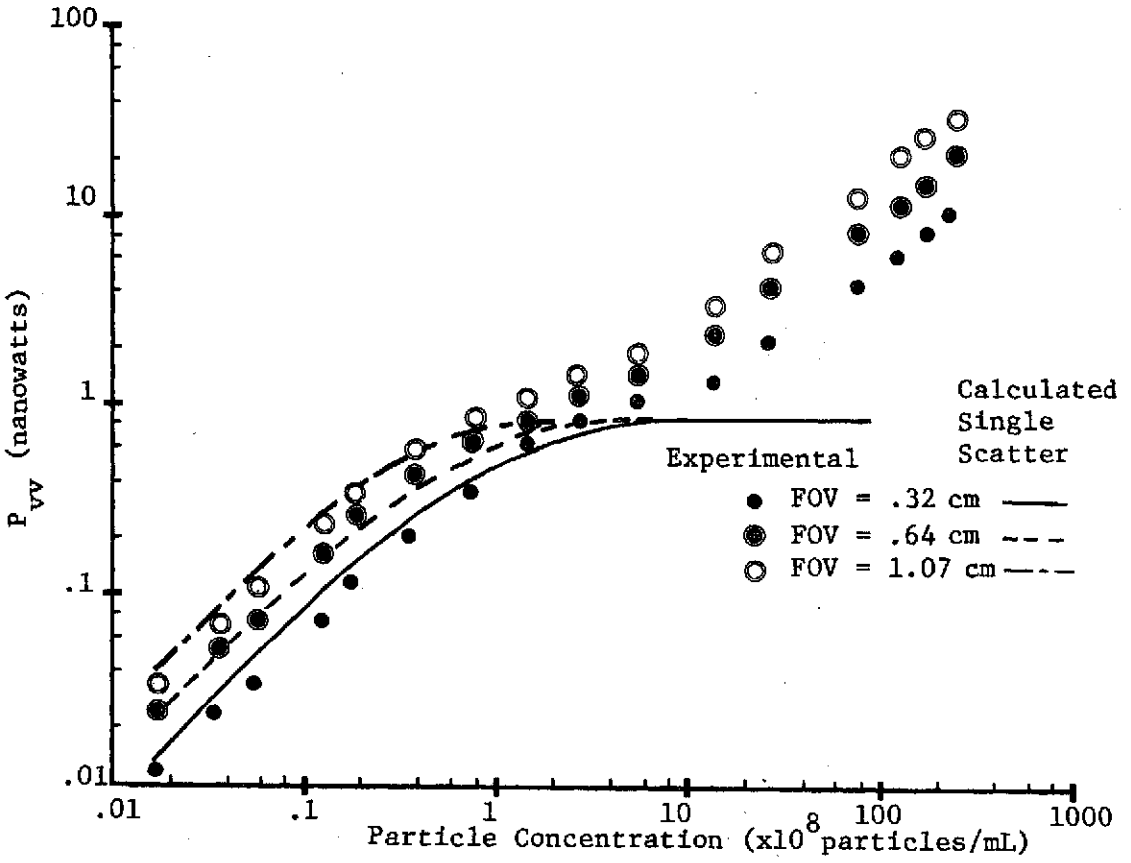

Figure VI-1. Comparison of Calculated Single Scatter Return with Experimental Data as a Function of Field of View and Latex Particle Concentration

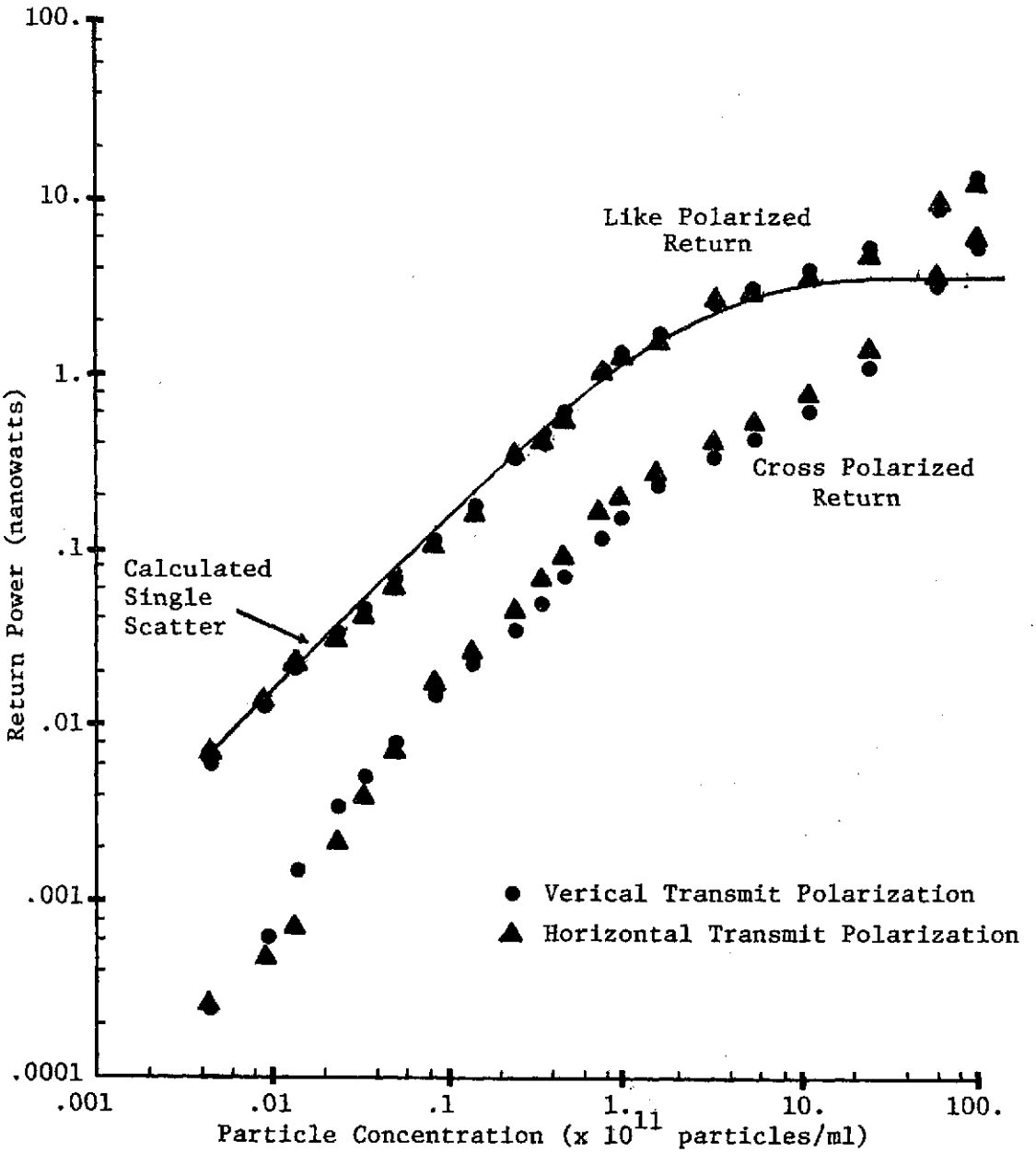

Figure VI-2. Comparison of Transmit Polarization and Calculated Single Scatter Return with Experimental Data as a Function of Teflon Particle Concentration

that at very low particle concentrations, the experimental backscatter is proportional to particle concentration, which is consistent with the expression for the single scatter volume reflection coefficient, γ_{vv}^{s}, given by (III-11). Observe also from these figures that as the particle concentration becomes larger, the experimental backscatter tends to saturate briefly and follow the asymtote of the calculated single scatter return. Finally, Figure VI-1 shows that at low particle concentrations, the experimental single scatter varies proportionally with the receiver field of view (or equivalently the mean depth L, given by (IV-1)), in direct agreement with the expression for the single scatter volume reflection coefficient, given by (III-11).

The good agreement obtained in comparing the experimental values with calculated values (at particle concentrations where single scatter appears to be the dominant mechanism) suggests that the single scatter term of (III-15) is valid. For large particle concentrations, however, the single scatter term does not adequately describe the backscatter and, therefore, the entire analytical model (represented by (III-15) and (III-16)), which incorporates multiple scatter effects, must be used. The following paragraphs examine the behavior of the entire model.

The validity of the entire analytical model is best established by comparing the relative magnitudes of the single scatter volume reflection coefficient, γ_{vv}^{s}, with the multiple scatter volume reflection coefficients, γ_{vv}^{m} and γ_{vh}^{m}. Referring to (III-15) and (III-16), observe that the multiple scatter volume reflection coefficients, γ_{vv}^{m} and γ_{vh}^{m}, represent the fraction of incident radiation that is multiple scattered in the direction of the receiver. The effective single scattter volume reflection coefficient, γ_{vv}^{s}, represents the fraction of incident radiation that is single scattered to the receiver. Examining the relative magnitudes of these volume reflection coefficients as a function of particle concentrations should provide a better understanding of the nature of the scattering mechanism and also establish the validity of the entire analytical model.

The magnitudes of the volume reflection coefficients are plotted in Figure VI-3 as a function of latex particle concentration for a field of view of .64 cm. The curve representing γ_{vv}^{s} was calculated from the relative scattering coefficient, the mean depth L, and the particle concentration, using (III-10). The values of the like polarized multiple scatter coefficient γ_{vv}^{m} were determined by solving (III-15) for γ_{vv}^{m} and using the measured values of like polarized backscatter for P_{vv} and the above mentioned

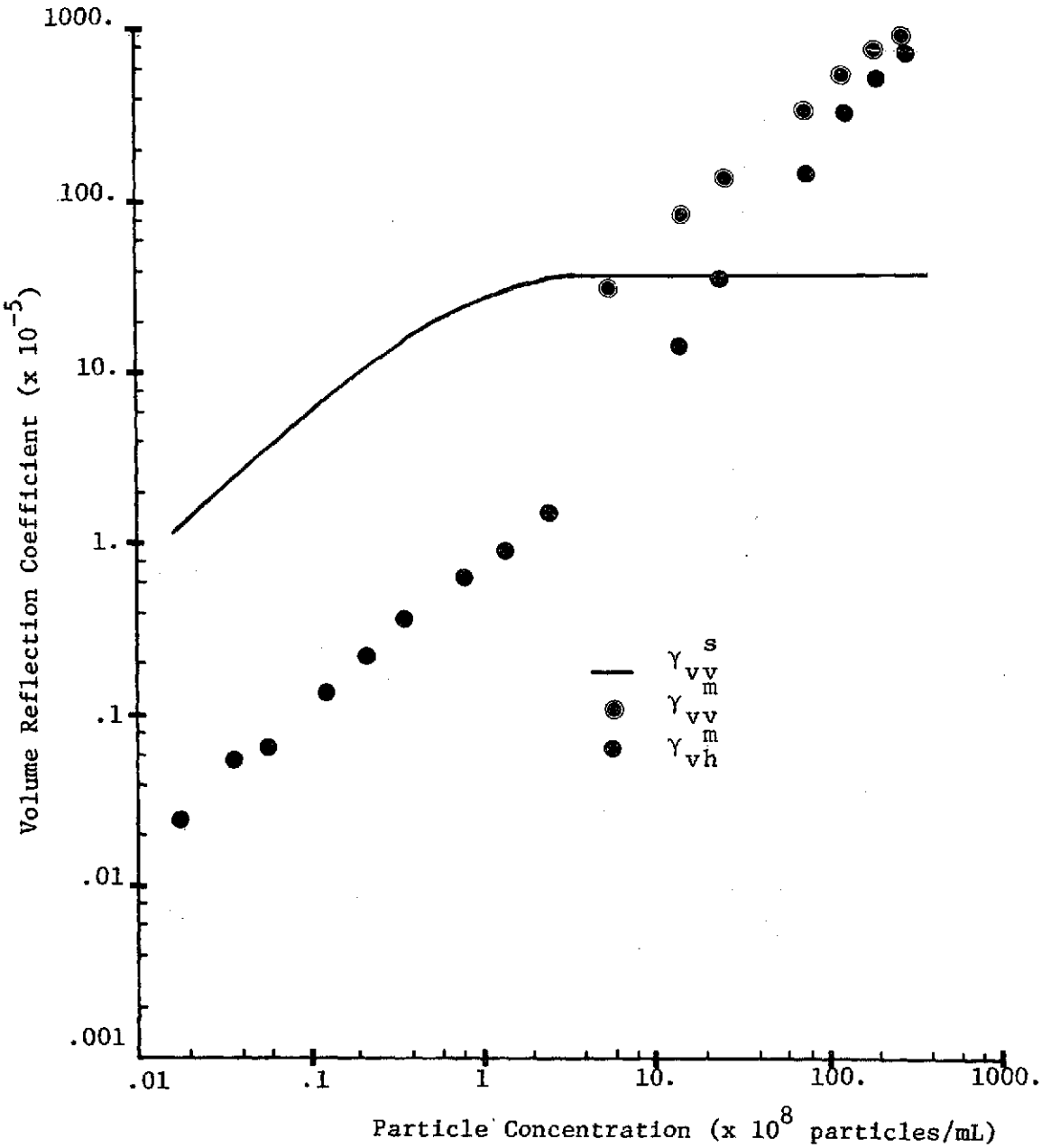

Figure VI-3. Comparison of Volume Reflection Coefficients as a Function of Latex Particle Concentration

values for γ_{vv}^{s}. The values for γ_{vh}^{m} were calculated from (III-16) using the measured values of P_{vh}.

For particle concentrations less that 10^9 particles/ml, the single scatter volume reflection, γ_{vv}^{s}, is much greater than the cross polarized multiple scatter volume reflection coefficient γ_{vh}^{m}. Therefore, in this particle concentration range, single scatter appears to be the dominant scattering mechanism (the values of γ_{vv}^{m} at particle concentrations where single scatter is dominant should not be used for comparison since these values represent the error in the single scatter model). However, observe that as the particle concentration increases beyond this region, the multiple scatter coefficients begin to become a more significant fraction of the backscattered energy. At a particle concentration of approximately 10^{10} particles/ml, γ_{vv}^{s} appears insignificant compared to the values of γ_{vv}^{m} or γ_{vh}^{m}, that is, multiple scatter appears to be the dominant scattering mechanism. Observe that at even higher concentrations of particles, γ_{vh}^{m} approaches γ_{vv}^{m}, which implies that the polarization of the backscattered wave is completely random and has no preferred orientation.

Observing Figure VI-3 (p. 71) also shows that the cross polarized volume reflection coefficient increases steadily with particle concentration. The increase in γ_{vh}^{m} in the single scatter region at concentrations less

than 10^9 particles/ml are likely to be due to the minute nonspherical properties of the particles and the presence of a small amount of multiple scattered radiation. At concentrations much higher than this, the increase in γ_{vh}^m with particle concentration is due to increased multiple scatter.

The previous examination of the relative magnitudes of the volume reflection coefficients shows that each volume reflection coefficient (γ_{vv}^s, γ_{vv}^m, and γ_{vh}^m) represents a significant fraction of the backscattered energy during certain portions of the progression from low particle concentrations to high particle concentrations. Therefore, the entire analytical model for describing the backscatter from turbid water, represented by (III-15) and (III-16), appears valid. Previous analytical backscatter models such as those developed by Rouse [30], Leader [29], and Wilhelmi [18] have ignored the presence of single scatter from the subsurface. It is apparent from the results presented in Figures VI-1(p.67), VI-2 (p. 68), and VI-3 (p. 71) that these effects cannot be ignored, except for a very dense medium, where multiple scatter is the dominant scattering mechanism.

Discussion

Having determined the validity of the analytical model, a discussion of the characteristics of the data described in Chapter V will be given to better understand the nature of the scattering phenomena. The first effect examined is the relationship between the presence of significant multiple scatter and the particle concentration. The calculated single scatter return plotted in Figure VI-1 (p. 67) appears to be consistent with experimental data when the value of the argument of the exponential in (III-9), $(2N\ \beta_r L)$, is less than approximately 1.2, and appears to vary proportionally with concentration for arguments less than approximately 0.2. These attenuation values are in fair agreement with the guidelines set forth by van de Hulst [32] in giving the critical attenuation values for determining the presence of multiple scatter. Van de Hulst claims that whenever the value of the argument in (III-9) is greater than 0.6, multiple scattering effects should be considered, and that single scatter should be the dominant mechanism for values of the argument less than 0.2.

While the attenuation factors mentioned above are reasonable indicators for determining when multiple scattering becomes dominant, possibly a stronger indication of the occurrence of this phenomena is the depolarization

ratio (cross polarized return divided by like polarized return). Figures VI-4 and VI-5 show that the depolarization ratio is small and relatively constant when single scatter is the dominant mechanism. Observe that it is when the single scatter term saturates that the depolarization ratio begins to increase, that is, when multiple scatter becomes the dominant scattering mechanism.

An interesting comparison can be made concerning the different depolarization ratios that are observed from the backscatter from low concentrations of latex particles and teflon particles. Observe that the depolarization ratio value for low concentrations of teflon particles (Figure VI-5) remains essentially constant at 0.1, while the depolarization ratio for the latex particles (Figure VI-4) remains essentially constant at a much smaller value of 0.03. The difference in the depolarization ratio values can be explained by observing Figures V-2 (p. 54) and V-4 (p. 55). Observe that the sphericity of the latex particles is much greater than that of the teflon particles. The latex particles, therefore, depolarize the incident radiation much less that the teflon particles (it is generally accepted that nonspherical scatterers depolarize incident radiation). Since this phenomena should introduce depolarization proportional to particle concentration, the depolarization ratio at low concentra-

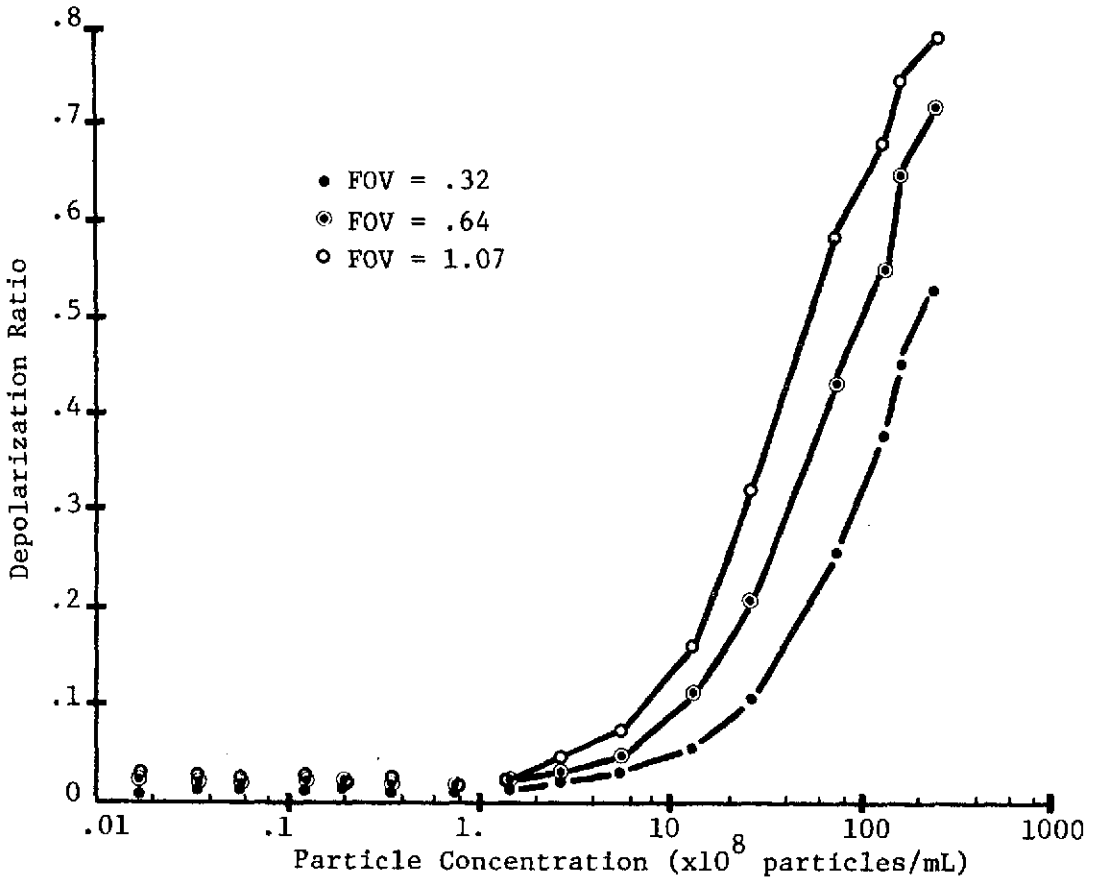

Figure VI-4. Comparison of Depolarization Ratios as a Function of Field of View and Latex Particle Concentration

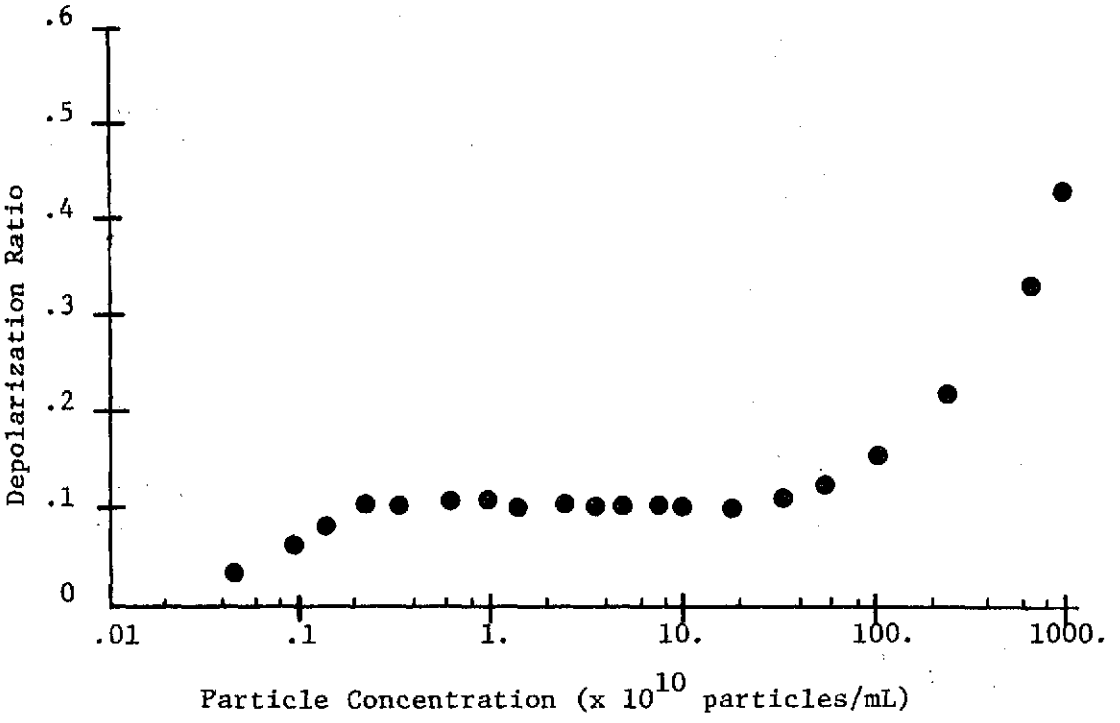

Figure VI-5. Graph of Depolarization Ratio as a Function of Teflon Particle Concentration

tions of scatterers (where single scatter is proportional to concentration) should remain constant.

Another effect studied to better understand the nature of the scattering mechanism was the effect on the backscatter of varying the field of view of the receiver. From Figures VI-1 (p. 67), VI-4 (p. 76), and VI-6, it is observed that not only do the like and cross polarized backscatter returns increase with increases in field of view, but the depolarization ratio increases as well. This is significant in that it proves that the depolarization is a multiple volume scatter process. This is apparent from the fact that if the depolarization was due to the nonspherical properties of the particles, the like-polarized and cross-polarized returns would increase proportionally with an increase in volume. However, since the cross-polarized returns increase more than the like returns (due to an increase in volume), the depolarization process must be due to scattering outside of the incident beam, that is, a volume scattering process.

Another effect examined in the turbid water experiments was the effect on the backscatter of adding an absorbent to the scattering medium. From Figure VI-7, it is observed that the depolarization ratio varies inversely with absorbent concentration. This observation supports the presence of a multiple scatter mechanism since the

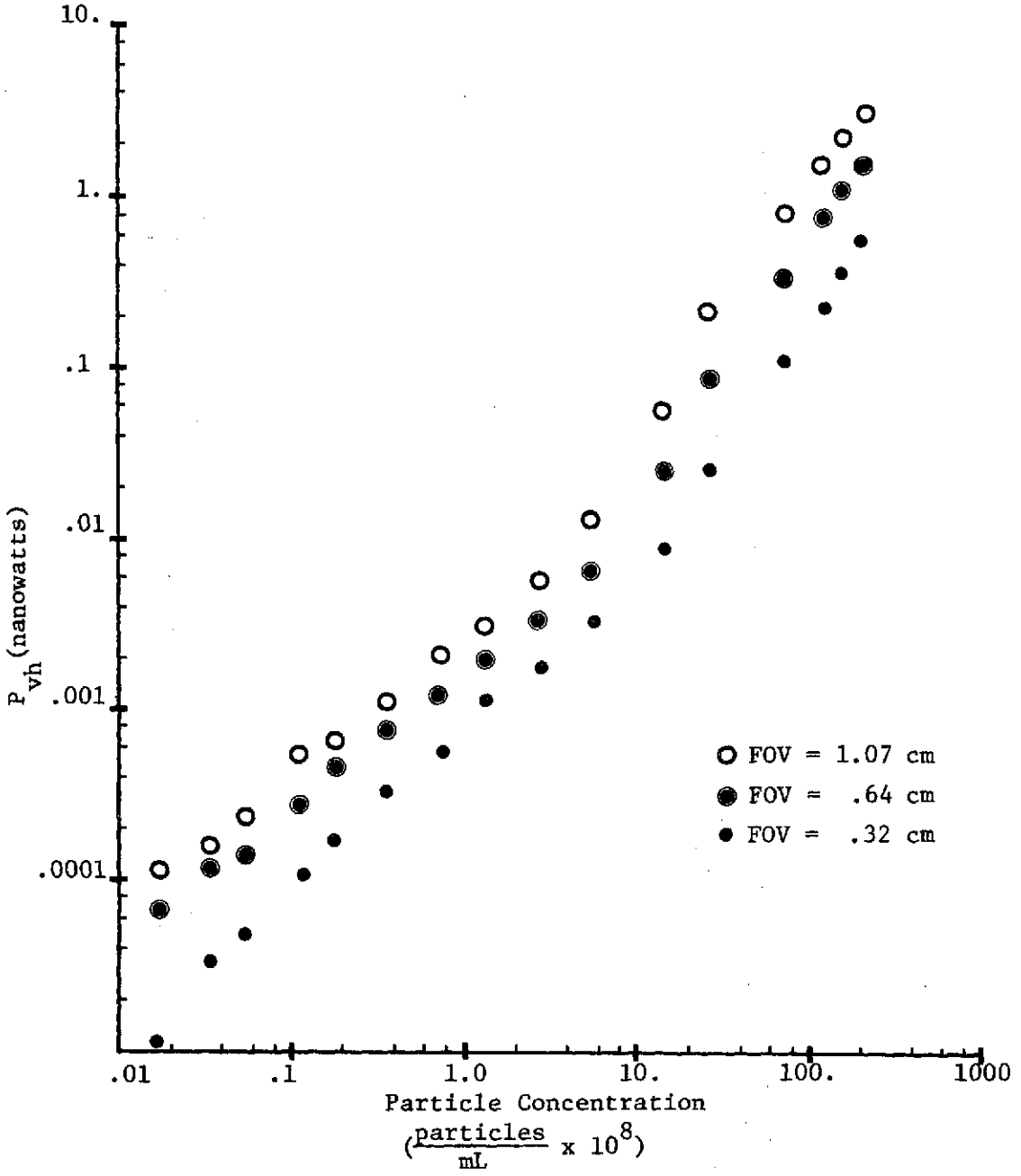

Figure VI-6. Graph of Depolarized Return as a Function of Receiver Field of View and Latex Particle Concentration

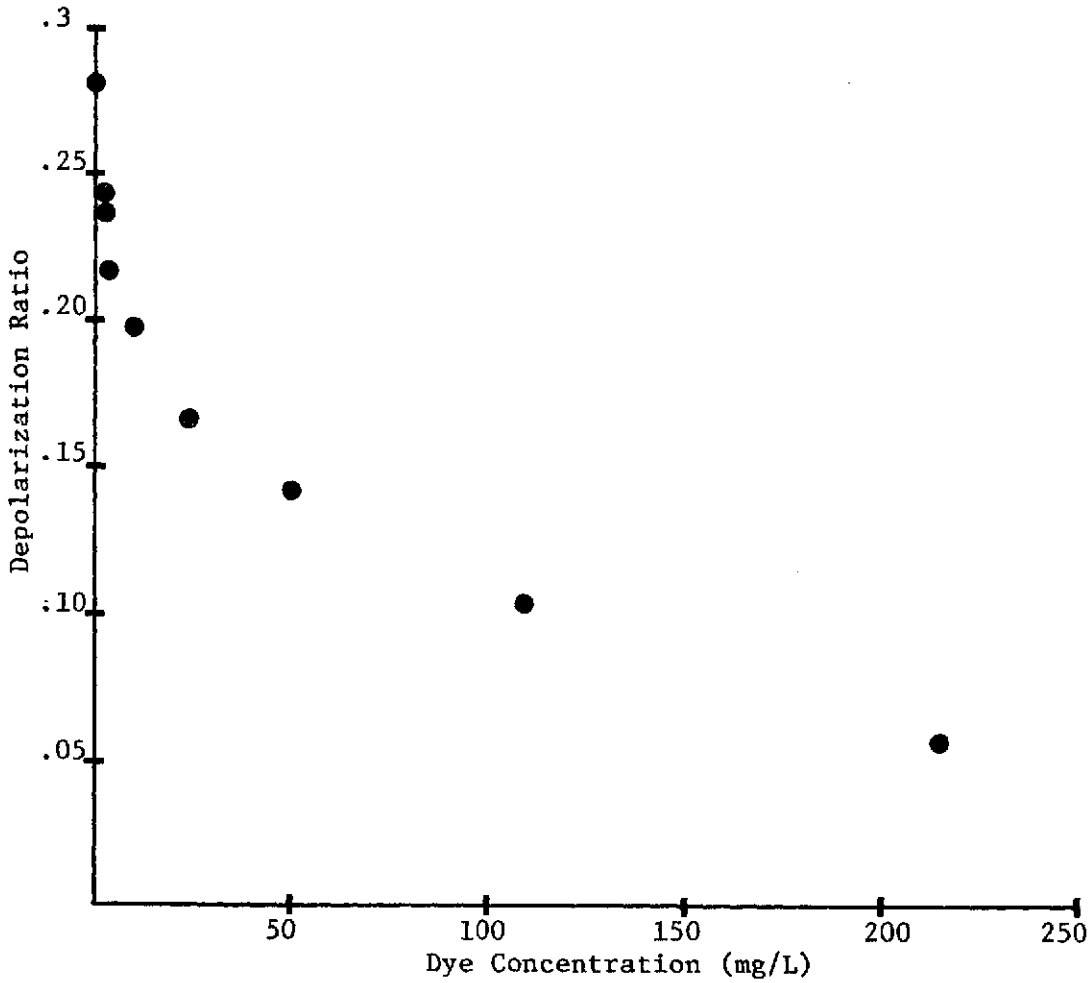

Figure VI-7. Graph of Depolarization Ratio as a Function of Absorbent Concentration

total path length of a multiple scattered wave is longer than that of a single scattered wave. The exponential attenuation ($e^{-\beta x}$, where x is the path length) due to the absorbent, decreases the intensity of the multiple scattered wave much more than the single scattered wave. This effect could hinder measurements of the particle concentration, since the behavior of the absorbent effects the depolarization ratio in the same manner as would the effect of decreasing the particle concentration. Note, however, that large dye concentrations were required to vary the depolarization ratio significantly and that under normal conditions in the natural environment it is not expected that the absorbent concentration would vary as dramatically.

The last effect studied in the turbid water experiment was the effect on the backscatter of changes in the transmit polarization. As can be observed from Figure VI-2 (p. 68), the like polarized returns were fairly consistent and independent of transmit polarization. The cross-polarized returns for horizontal transmit polarization appear to be a small amount larger than the cross-polarized returns for vertical transmit polarization (the cross returns at very low particle concentration of particles are beyond the noise limitation of the system and should not be used for comparison). This small inconsistency of cross returns does not support the analytical model, that

is, the analytical model supports the law of reciprocity. Other investigators such as Rouse [30] also contend that recriprocity must hold for an isotropic media. Therefore, the small differences of P_{vh} and P_{hv} must be due to the presence of nonspherical scatterers.

Natural Waterways

Representative results of the first field measurement trip (data are listed in Appendix B and coded by 71473 and 71573 under DATE) from atop a bridge on the Brazos River near Waco, Texas are plotted in Figures VI-8 to VI-11. Relatively few data observations were made during this trip because of several experimental difficulties. These data, however, did provide initial indications that the like polarized backscatter, cross polarized backscatter, and the depolarization ratio vary proportionally with turbidity and suspended solids and inversely with transmittance. The twenty minute time history of P_{vv} (Figure VI-10) shows clearly that an increase in turbidity results in an increase in P_{vv}. Figure VI-10 also implies that for that particular location, the ordinate of the time history could have essentially been turbidity and provided a continuous, real-time measurement of that parameter. The few horizontal transmit polarization measurements showed

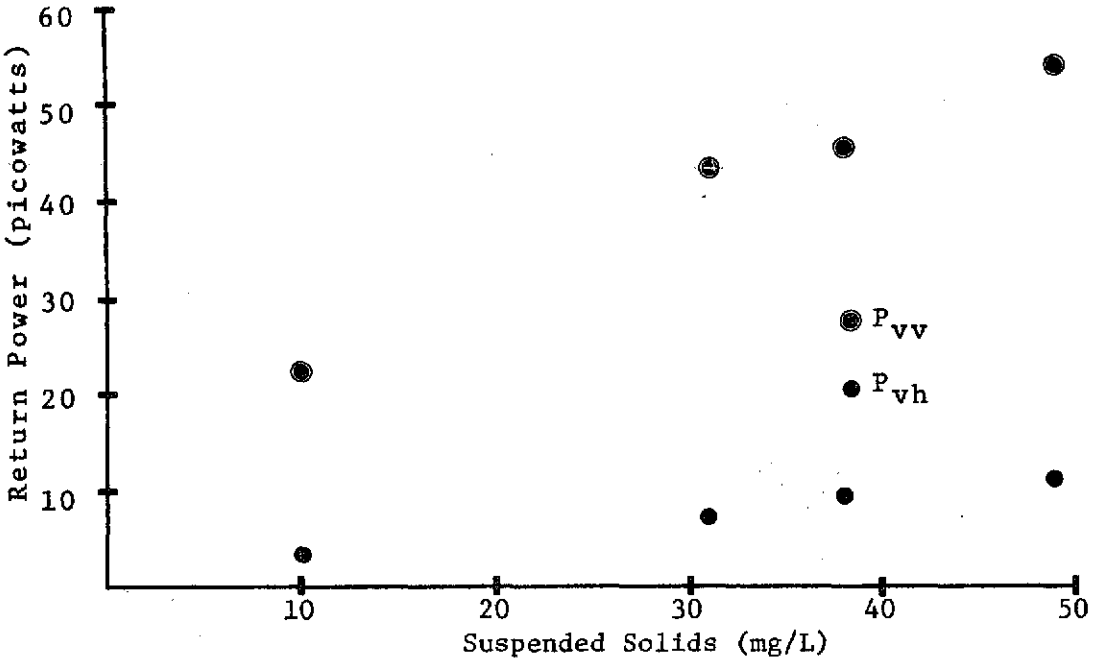

Figure VI-8. Graph of Lidar Returns as a Function of Suspended Solids Observed from a Bridge on the Brazos River

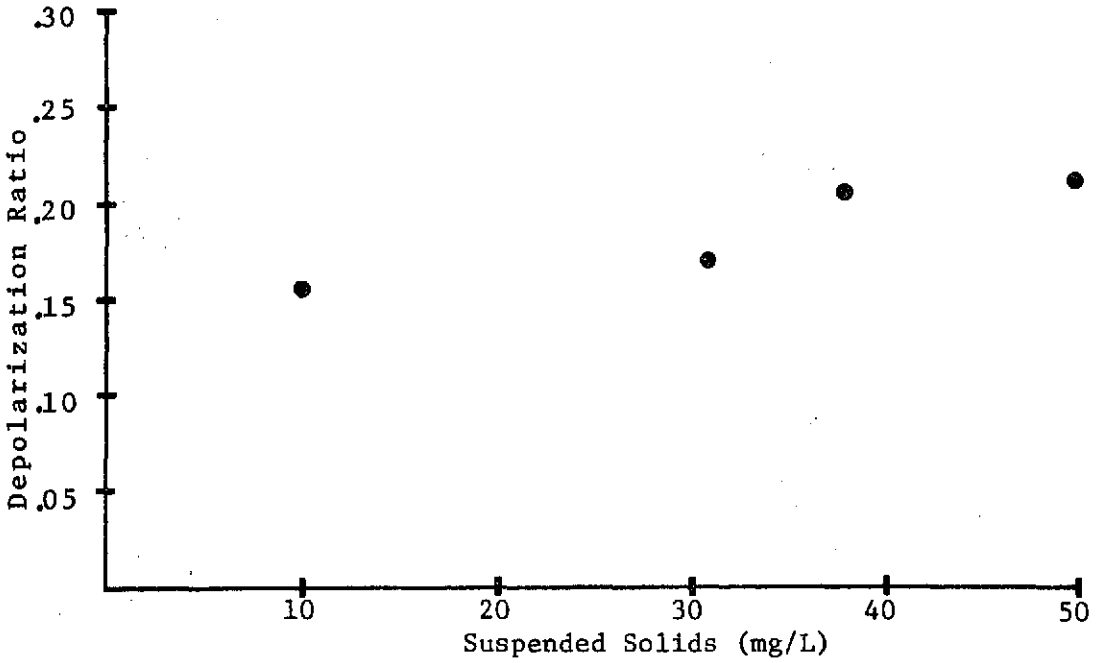

Figure VI-9. Graph of Lidar Depolarization Ratios as a Function of Suspended Solids Observed from a Bridge on the Brazos River

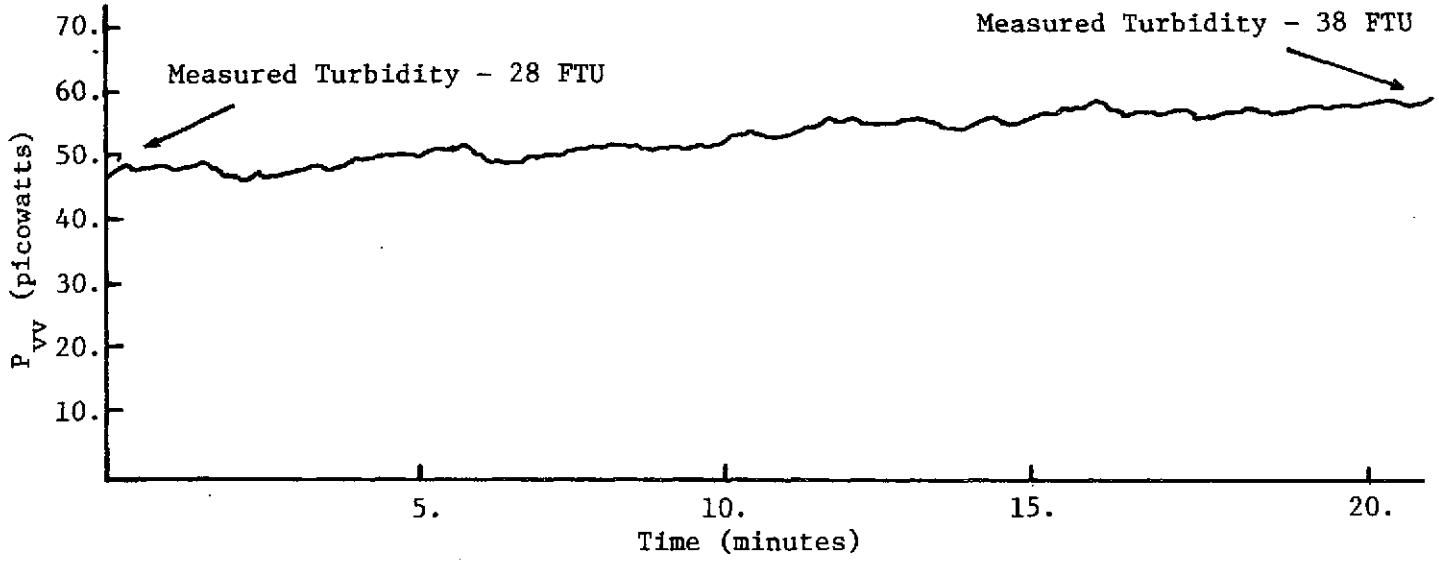

Figure VI-10. Twenty Minute Time History of Like Polarized Returns Recorded from a Bridge on the Brazos River

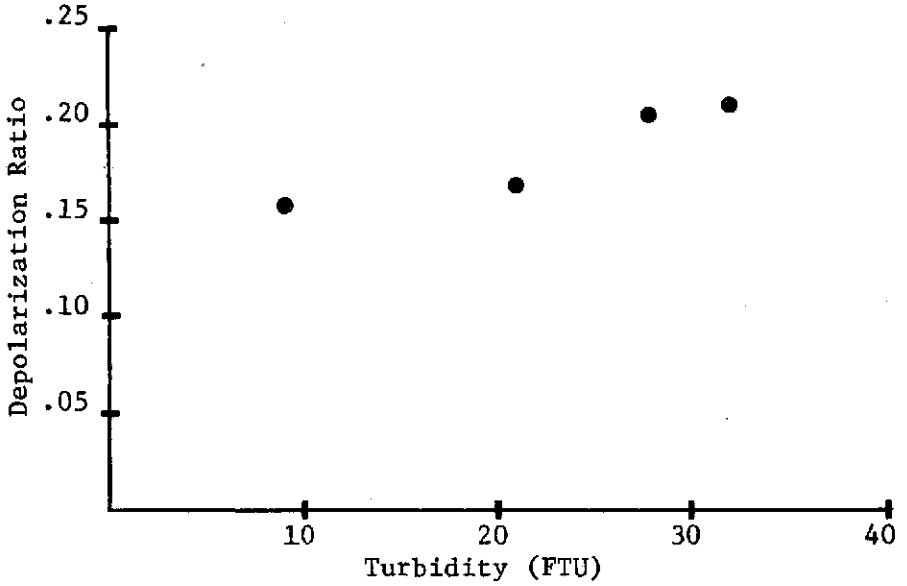

Figure VI-11. Graph of Lidar Depolarization Ratio as a Function of Turbidity Observed from a Bridge on the Brazos River

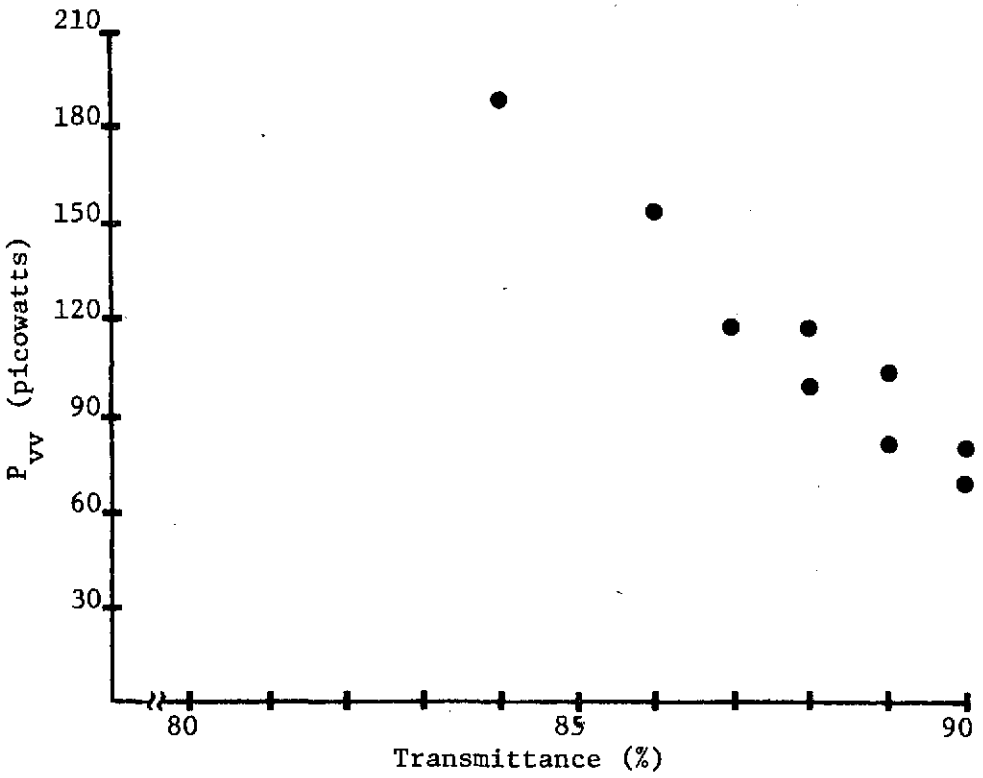

Figure VI-12. Graph of Like Polarized Returns as a Function of Transmittance Observed along Houston Ship Channel from a Boat

insignificant differences in backscatter relative to vertical transmit polarization measurements.

A representative plot of the results from the field measurement trip on the boat Excellence along the Houston Ship Channel (data are listed in Appendix B and coded by 92573 under DATE) is given in Figure VI-12 (p. 85). Note that the return power supports the results of the previous field measurement trip by varying inversely with transmittance. A significant measurement error was encountered in these measurements which partially explains the scattered data points. The lidar slant range aboard the Excellence was approximately 2.84 m, with a receiver field of view diameter at the surface of 1.26 cm and a distance between the receiver and transmitter of 12.4 cm. According to (IV-1), the values correspond to a mean depth along the beam of approximately 14.4 cm. Since the peak value of water wave heights was approximately 10 cm, the lidar measurement volume was changing significantly with wave height variations. Time averaging with the lock-in amplifier smoothed these variations in returns, but did not provide accurate and consistent measurements of backscatter. As a result of this problem, a system constraint was developed for future field measurements to improve performance in a natural environment with water waves. This constraint requires that the mean depth, L, multiplied

by cos θ (since L is the depth along the incident beam) be much greater than the peak wave height, Δ, or

$$L \cos(\theta) \gg \Delta$$

which when substituting (IV-2) for L gives

$$\frac{d_{ph} R^2 \cos(\theta)}{w F} \gg 2\Delta \qquad \text{(VI-1)}$$

This equation represents a parametric decision criterion for lidar operation under field conditions. To minimize wave effects using this equation requires careful consideration because several trade-offs are involved. Increasing the receiver field of view diameter ($d_{ph}R/F$) does tend to minimize wave effects, but only at the expense of increased background noise (solar radiation). An optimal procedure then for the minimization of wave effects is first to minimize the distance, w, between the transmitter and receiver. Second, for a given altitude, A, the slant range, R, is given by

$$R = A / \cos(\theta)$$

which when substituted in (VI-1) gives

$$\frac{A^2 d_{ph}}{w \cos(\theta) F} \gg 2\Delta$$

This equation shows that wave effects can also be minimized by operating at grazing angles. However, observations of the Fresnel transmission coefficient show that these coefficients vary dramatically with changes in incidence angles near grazing. Wave variations, that is, local angle variations, would therefore create significant backscatter "noise" at incidence angles greater than 50°. A general procedure for minimizing wave effects considering all parameters is to: 1) minimize the distance between the transmitter and receiver; 2) operate at incidence angles less than 50° but away from nadir (to avoid specular reflections); and 3) maximize the slant range without forcing field of view at the surface to be much larger than the diameter of the incident beam. Observe that a receiver field of view matched to the transmitted beam is not optimum, since wave variations can significantly effect the

measurement volume. Therefore, at ranges less than about 20 m, the diameter of the receiver field of view at the surface should be at least twice the diameter of the incident beam.

Employing these criteria on the last field measurement trip aboard the Excellence (data are listed in Appendix B and coded by 120173 under DATE) provided excellent results. Representative results are plotted in Figures VI-13 to VI-15. Note that the data consistency is better than the data from previous field measurement trips and that the depolarization varies significantly with changes in turbidity, suspended solids, and transmittance. Also the magnitude of the depolarization ratios are within the same range as those measured from simulated turbid water in the laboratory. Therefore, the laboratory simulations of turbid water employed earlier to test the validity of the analytical model are valid simulations of natural water. The magnitudes of the depolarization ratios are also within the range of laboratory depolarization ratios which varied directly with particle concentrations. This is significant because this confirms that the magnitudes of particle concentrations that are found in natural waterways are large enough to cause changes in depolarization ratios for different concentrations. These values also infer that single scatter is also present from the subsurface, and that the

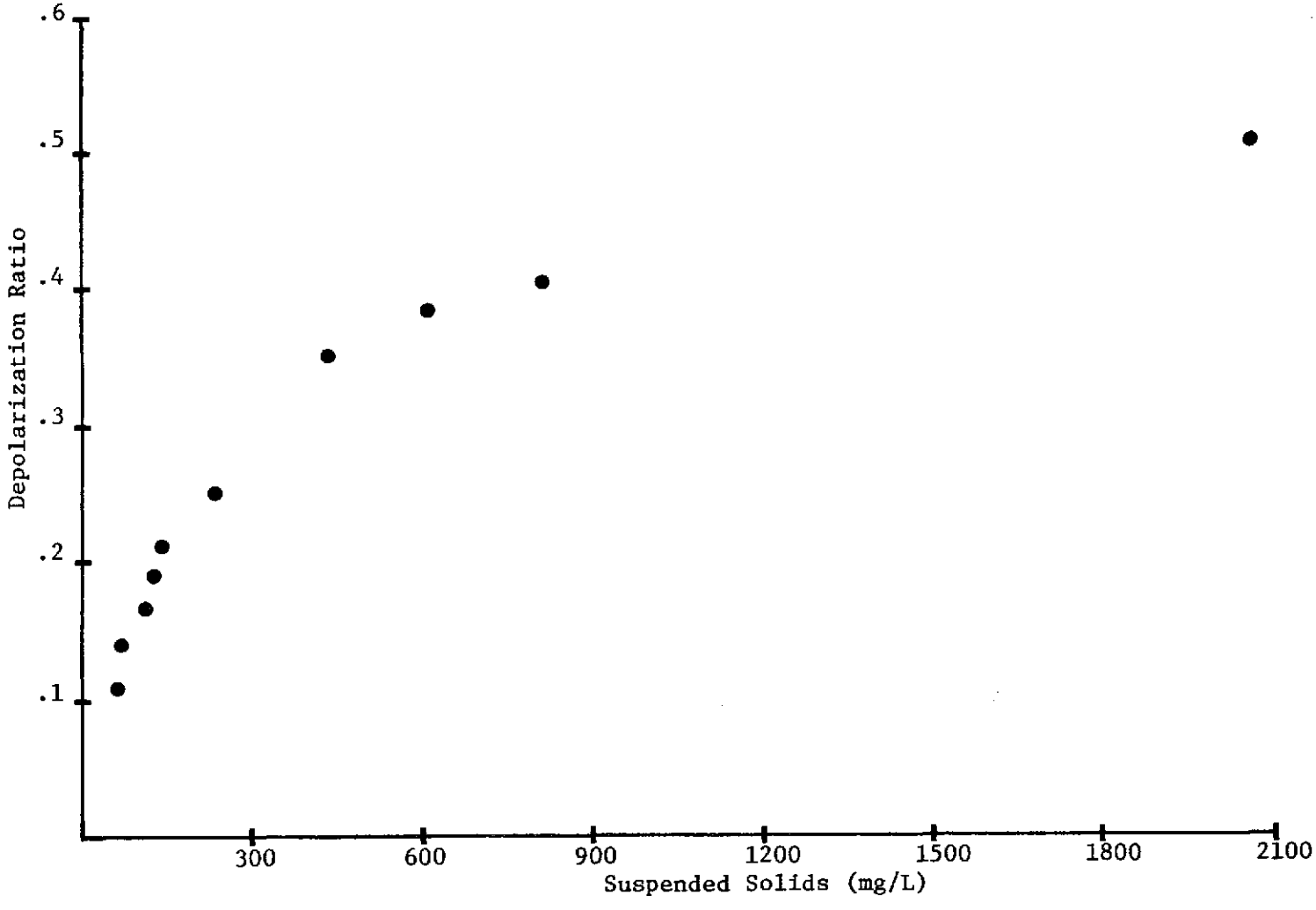

Figure VI-13. Graph of Lidar Depolarization Ratio as a Function of Suspended Solids Observed Along the Brazos River from a Boat

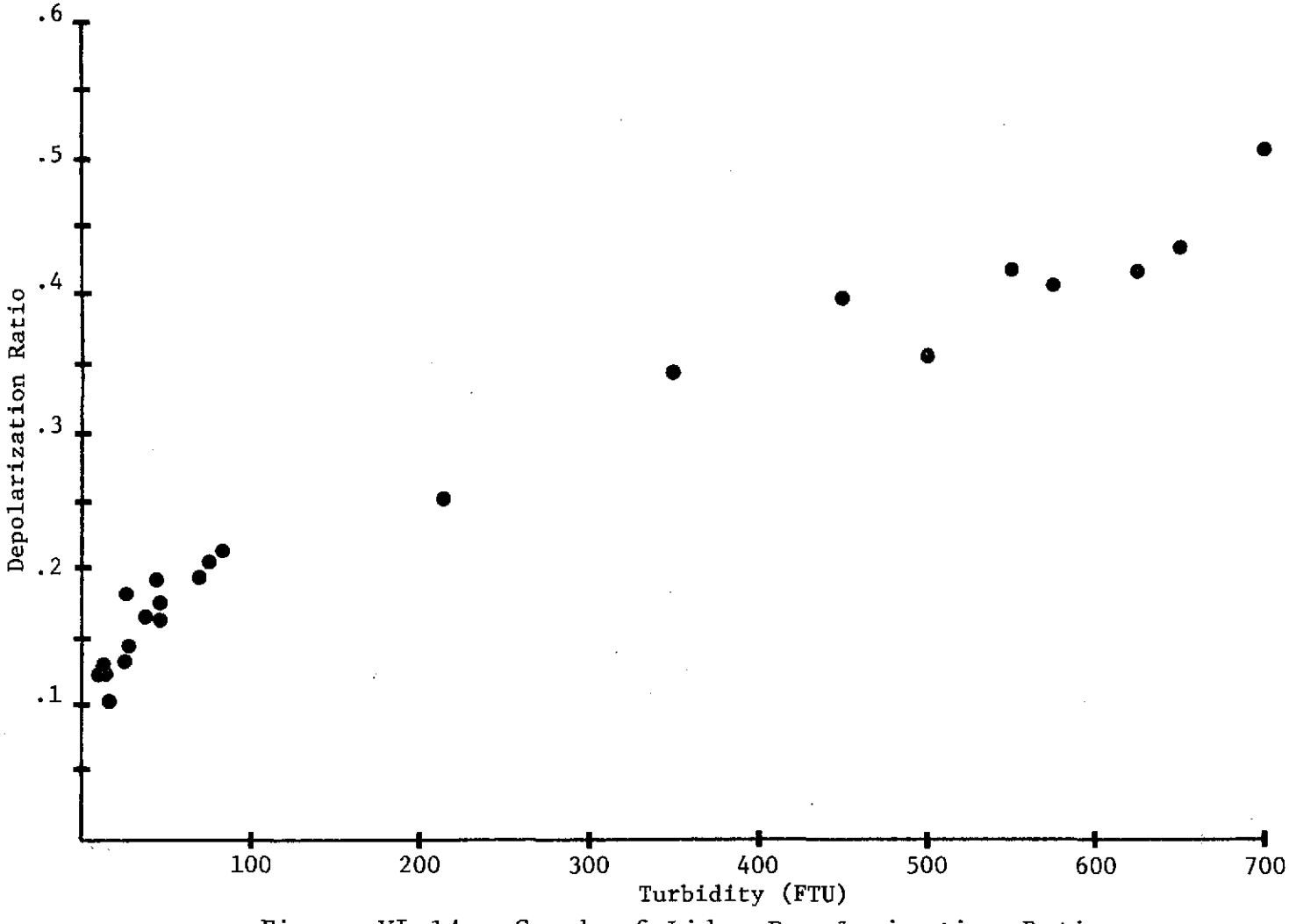

Figure VI-14. Graph of Lidar Depolarization Ratios as a Function of Turbidity Observed Along Brazos River From a Boat

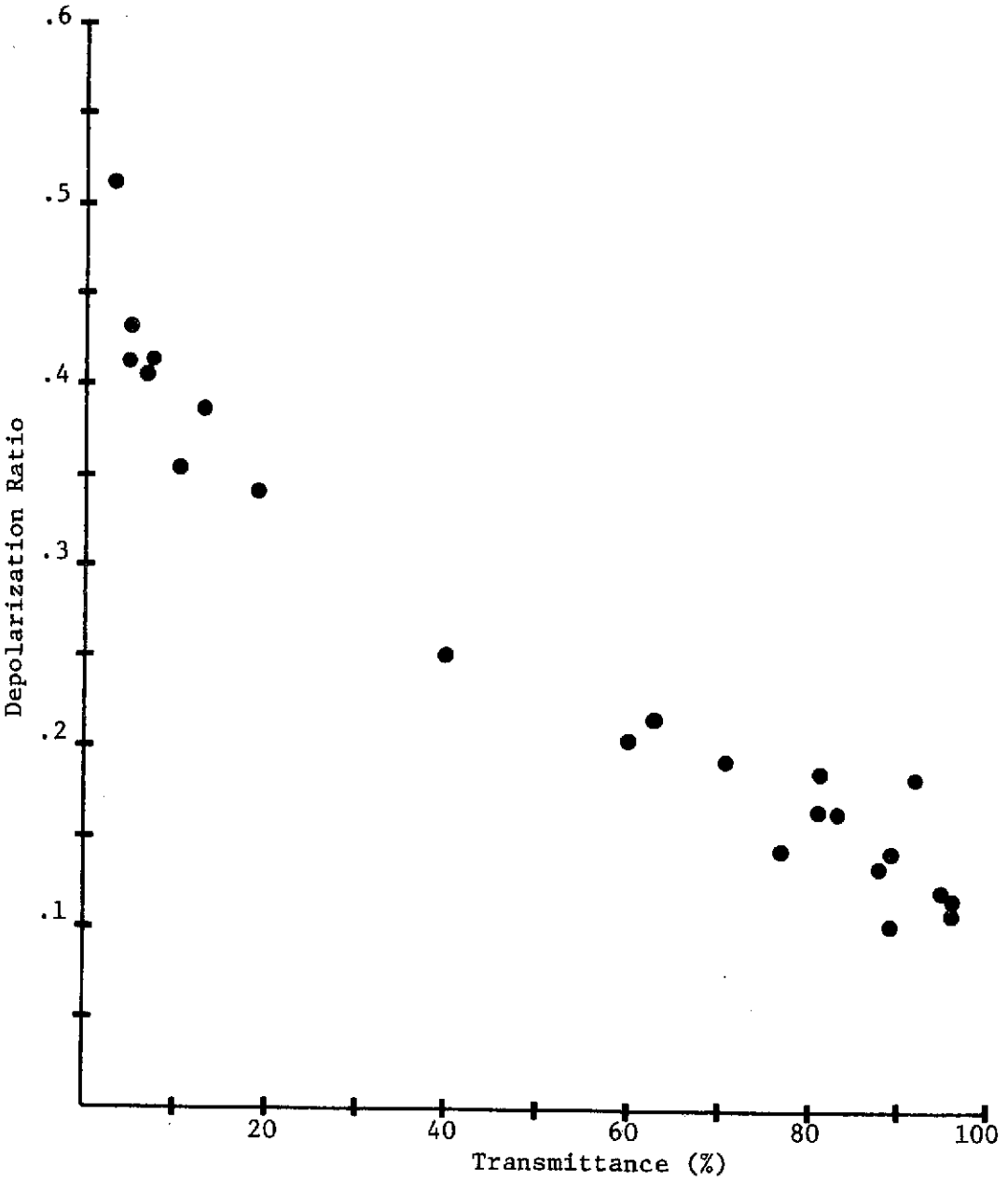

Figure VI-15. Graph of Lidar Depolarization Ratios as a Function of Transmittance Observed Along Brazos River From a Boat

model found valid in the previous sections appears valid for describing the backscatter from natural waterways.

An experimental error common to all field measurement data was the requirement of a 30 second time interval between consecutive recordings of P_{vv} and P_{vh}, due to the single channel capacity of the lock-in amplifier. This time lag between recordings coupled with collecting water samples within these intervals can add significant error (approximately 5%) because of the dynamic changes that occur in the subsurface over a short period of time, as shown in Figure VI-10 (p. 84).

Oil on Water

Comparison With Analytical Model

The analytical model for oil on water represented by (III-20) and (III-21) incorporated the effects on the backscatter of the change in refractive index and attenuation due to the presence of a laterally inhomogeneous layer of oil on water. It was assumed in this model that the attenuation due to oil was independent of polarization, that is, the oil attenuated both like and cross polarized returns in the same fashion. Employing these results, the theoretical values of backscatter were calculated for varying thicknesses of different test oils on water.

Representative values for the indices of refraction, transmission coefficients, and homogeneous extinction coefficients employed in (III-20) and (III-21) were determined empirically or from published work [36], and are given in Tables VI-3 and IV-4 (the significance of these values is discussed in the next section.) For these laboratory studies, the oil layers were laterally homogeneous, which allowed use of homogeneous indices of refractions and extinction coefficients (ρ=1 in (III-19) and (III-22)). The value for P_{vv} and P_{vh} in (III-20) and (III-21) are the measured values of backscatter in the absence of oil.

Graphical comparisons of calculated values and experimental values of backscatter for several test oils (values are for an excitation wavelength of λ=.6328 μm) are given in Figures VI-16 to VI-19, as a function of oil thickness. Observe from Figures VI-16 and VI-17 that the attenuation due to crude oil is quite significant, resulting in a decrease in like or cross polarized backscatter greater than 3 orders of magnitude for an oil thickness of .3 mm. The attenuation due to no. 2 fuel oil is less than that of crude oil, but still results in a decrease of backscatter, greater than 1 order of magnitude for a 1 mm oil thickness.

Table VI-3. Values of Refractive Indices and Transmission Coefficients Used in Calculations of Backscatter from Oil on Water

Test Oils	n_o	T_{13}^v, T_{31}^v	T_{12}^v, T_{21}^v	T_{32}^v, T_{23}^v	T_{32}^h	T_{21}^h	T_{31}^h
Crude Oil	1.48	----	.976	.997	.996	.945	----
No. 2 Fuel Oil	1.44	----	.980	.999	.998	.953	----
SAE 30	1.43	----	.981	.999	.998	.954	----
Gasoline	1.37	----	.985	.999	.999	.963	----
Kerosene	1.37	----	.985	.999	.999	.963	----
Water	1.33	.988	----	----	----	----	.970

Table VI-4. Homogeneous Extinction Coefficients for the Test Oils at Two Different Wavelengths

Test Oils	α_r (nepers/mm; λ=.6328 μm)	α_b (nepers/mm; λ=.4416 μm)	Ratio (α_r/α_b)
Crude Oil	12.5	9.12	1.37
No. 2 Fuel Oil	1.5	7.10	.207
SAE 30	.05	.35	.143
Gasoline	.006	.07	.08
Kerosene	.015	no measurable attenuation	-----

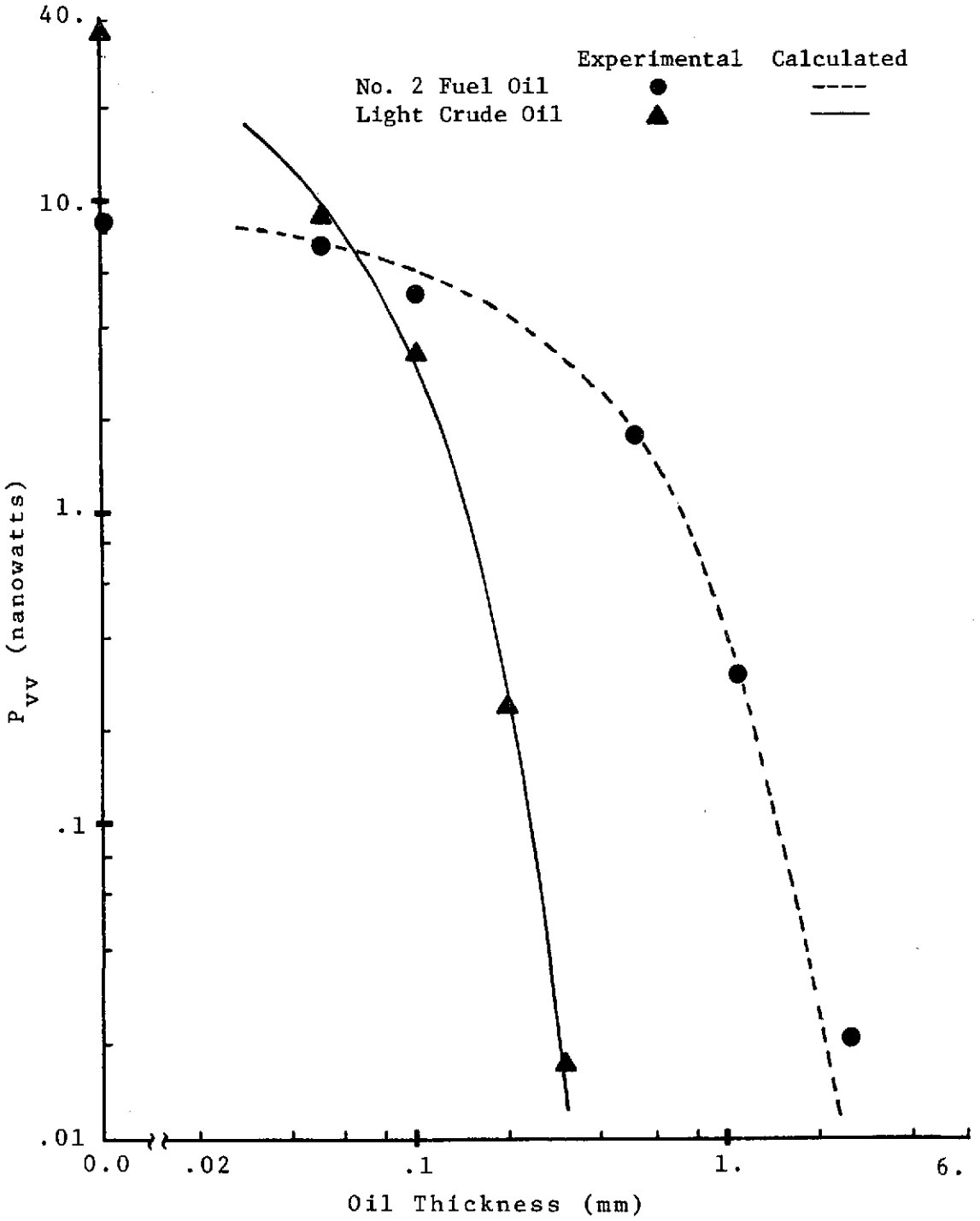

Figure VI-16. Comparison of Analytical Model with Experimental Data for Like Polarized Backscatter from Crude Oil and No. 2 Fuel Oil on Turbid Water

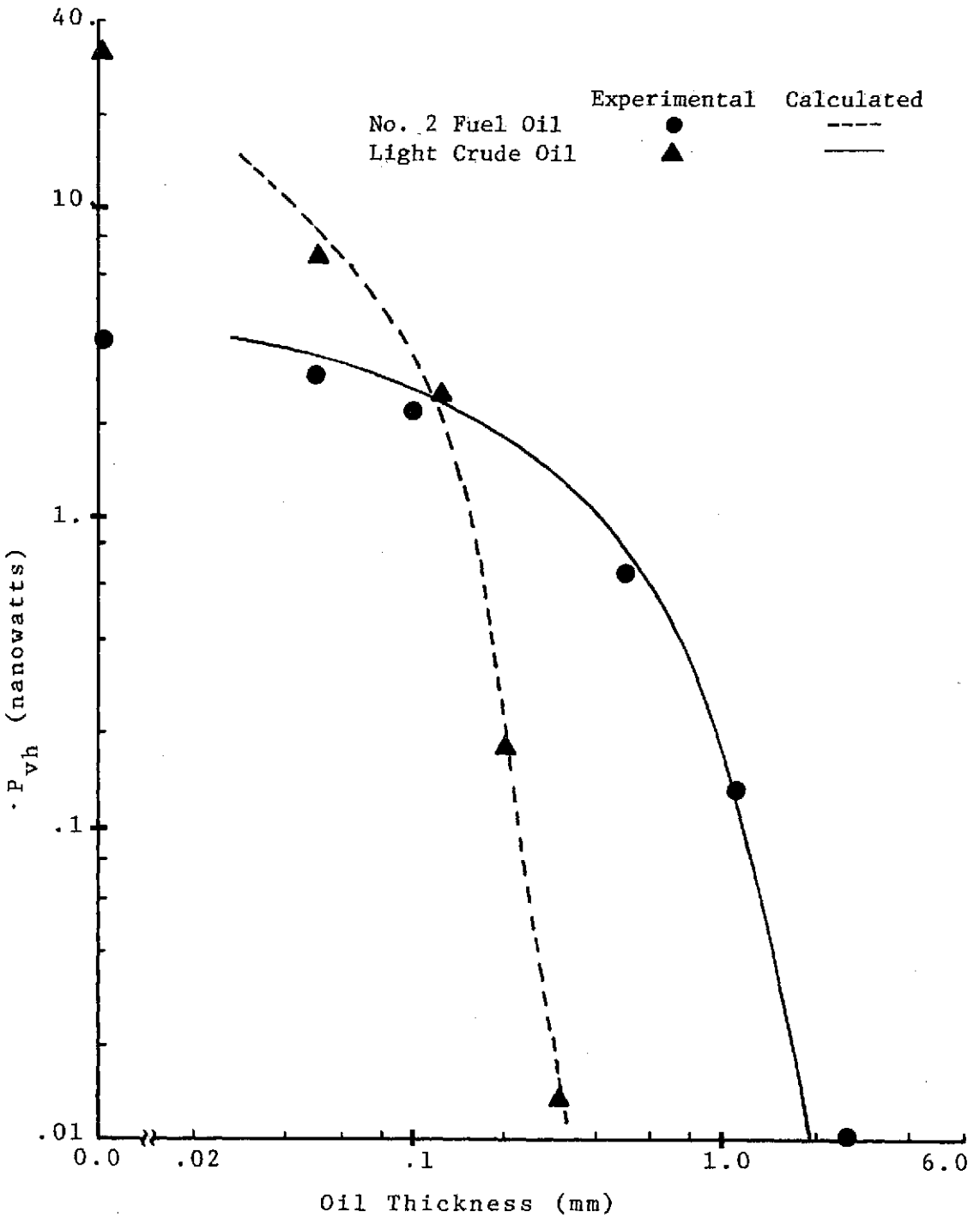

Figure VI-17. Comparison of Analytical Model with Experimental Data for Cross Polarized Backscatter from Crude Oil and No. 2 Fuel Oil on Turbid Water

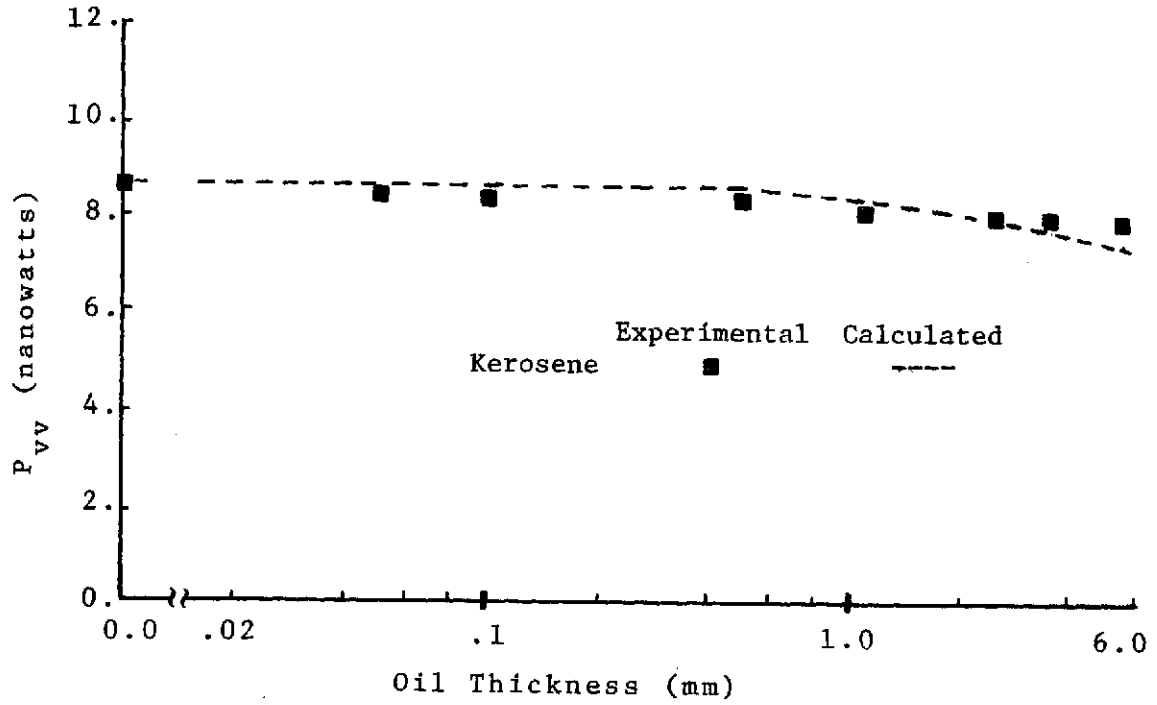

Figure VI-18. Comparison of Analytical Model with Experimental Data for Like Polarized Backscatter from Kerosene on Water

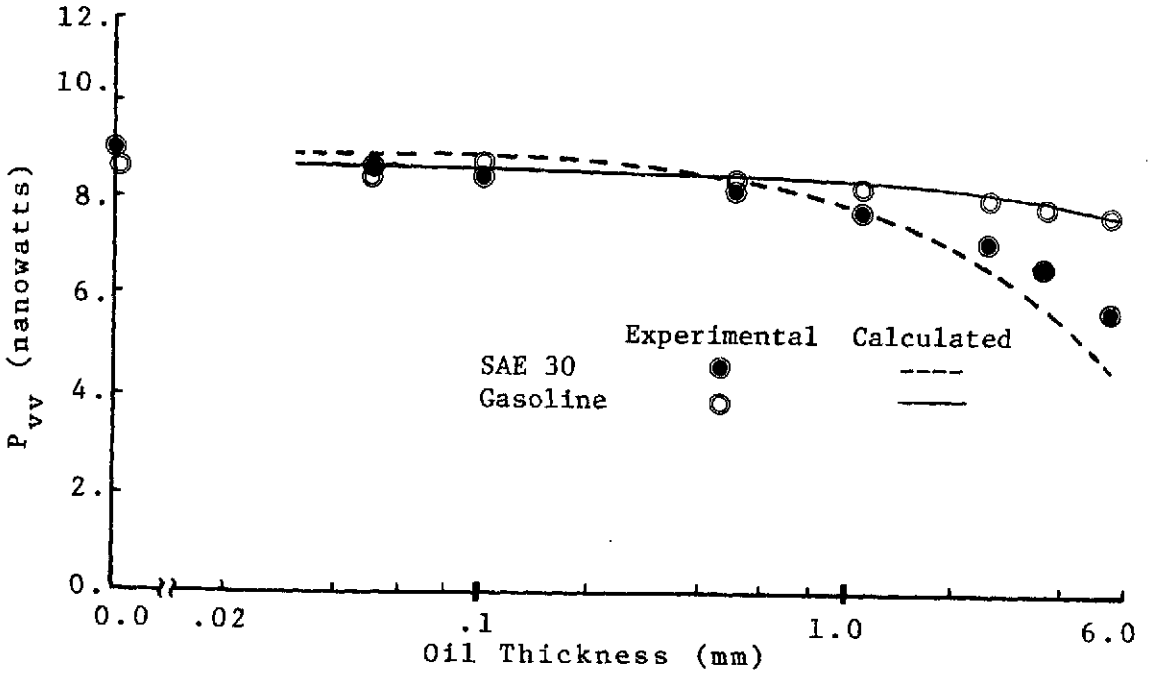

Figure VI-19. Comparison of Analytical Model with Experimental Data for Like Polarized Backscatter from SAE 30 and Gasoline on Turbid Water

The attenuation due to kerosene is minimal (Figures VI-18 (p. 98) and VI-19 (p. 98)), even at oil thicknesses as large as 6 mm. The attenuation due to gasoline (Figure VI-19 (p. 98)) is also quite small for the red excitation wavelength used in these measurements, decreasing the backscatter only a few percent for large oil thicknesses. The attenuation due to the presence of SAE 30 refined motor oil is also relatively small, decreasing the backscatter approximately 15 percent for an oil thickness of 1 mm. Good agreement was obtained between calculated values and experimental values of backscatter for all test oils (Figures VI-16 to VI-19 (pp. 96-98)). An examination of the depolarization ratio will now be given to determine its behavior as a function of oil thickness.

The depolarization ratio remains essentially constant for different thicknesses of oil on water (Figures VI-20 to VI-22). This is in direct agreement with the calculated values for the depolarization ratio, since the model assumed equal attenuation for like and cross polarized returns. Large values of depolarization ratios were observed because of the large particle concentrations that had to be used (for large thicknesses of crude oil) to provide magnitudes of backscatter above the noise limitations of the system. Therefore, any volume scatter from the oil itself may have been masked by the large contribution of

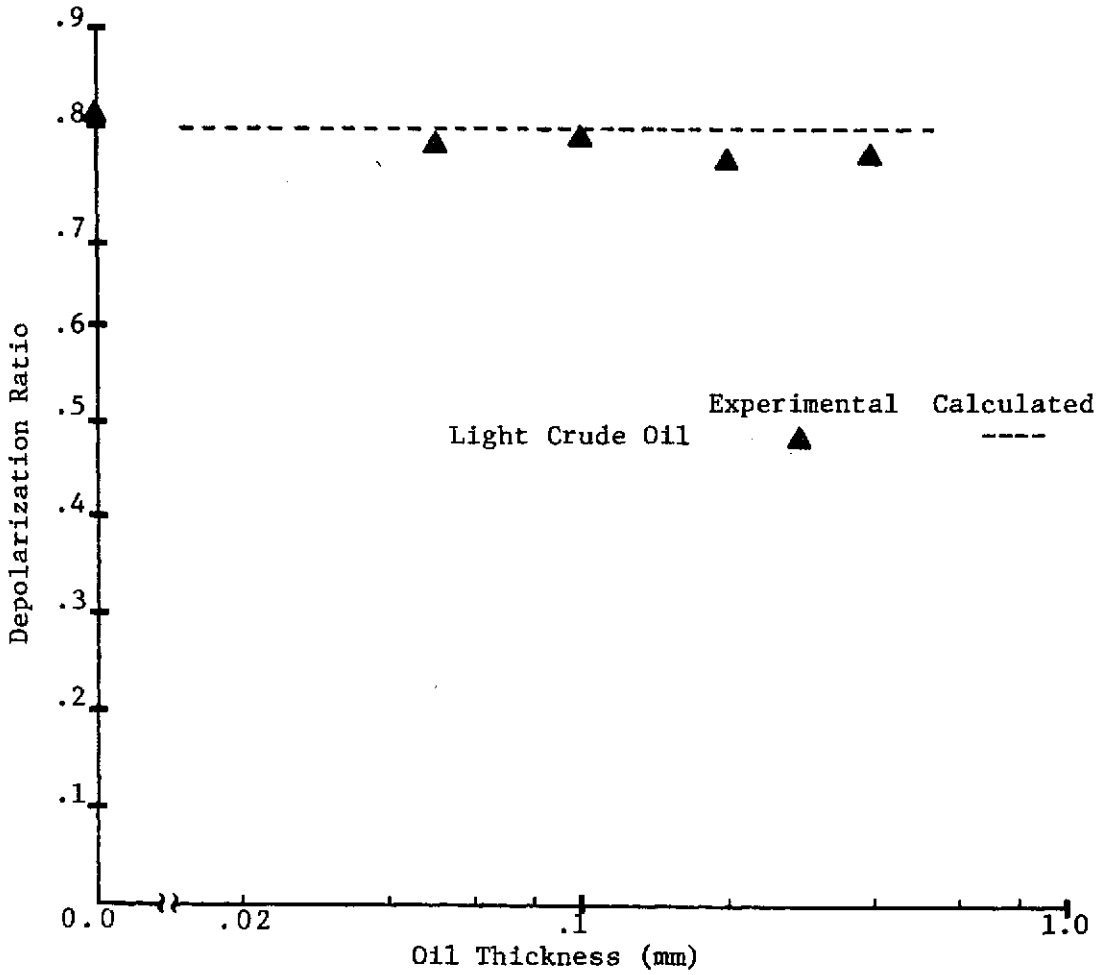

Figure VI-20. Comparison of Analytical Model with Experimental Data for the Depolarization Ratios from Crude Oil on Turbid Water

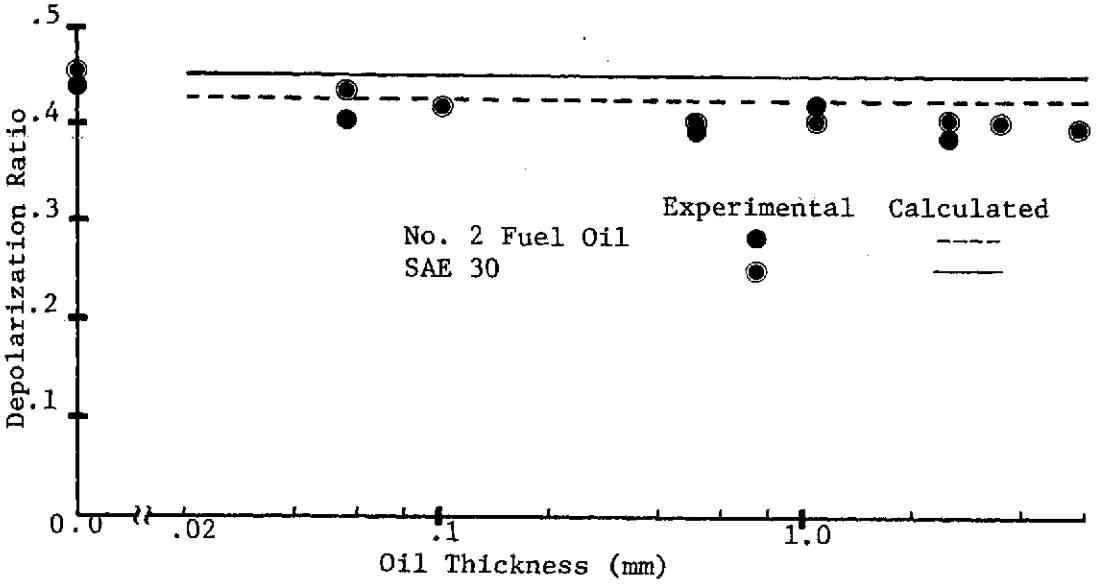

Figure VI-21. Comparison of Analytical Model with Experimental Data for the Depolarization Ratios from No. 2 Fuel Oil and SAE 30 on Turbid Water

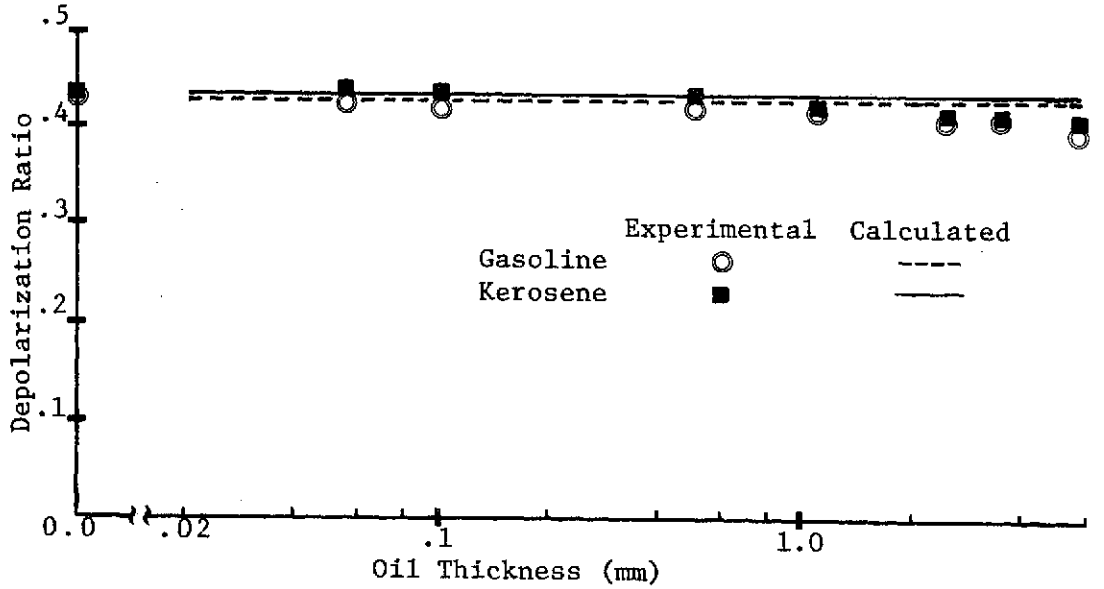

Figure VI-22. Comparison of Analytical Model with Experimental Data for the Depolarization Ratios from Gasoline and Kerosene on Turbid Water

volume scatter from the subsurface. It is felt, however, that the volume scatter contribution from any of the test oils would be much smaller than that observed from the subsurface.

The excellent agreement between the calculated values and experimental values of backscatter and depolarization ratios suggests that the analytical model for oil on water represented by (III-20) and (III-21) is valid.

The estimated experimental error in the data acquisition of the oil on water experiments is 5 percent. The most significant error which was encountered in the procedure was the experimental measurements of oil thickness. Oil thickness was measured by adding a known volume of oil to a known, contained surface area, with the quotient of the volume and surface area giving the oil thickness. The known volume of oil added was subject to several experiment constraints such as the adhesive characteristics of the oil to the measurement vessle. The oil on water also tended to move toward the edge of the container which reduced the oil thickness at the center of the container, where the laser beam was incident.

Discussion

The detection, identification, and measurement feasibility of oil on water can be established by observing the following characteristics of the data presented in Figures VI-4 (p. 76) and VI-5 (p. 77), VI-16 to VI-19 (pp. 96-98), VI-20 to VI-22 (pp.100-101), and in Table VI-4 (p. 95): 1) the variation of subsurface particle concentrations significantly alters the depolarization ratio; 2) the presence of oil does not significantly alter the depolarization ratio; and 3) the attenuation due to oil is a function of oil type, oil thickness, and excitation wavelength. Using these results, a general procedure can be followed for detection, type identification, and thickness measurement of oil on water. The detection of oil on water should require only a single wavelength lidar polarimeter and an observance of P_{vv}, P_{vh} and the depolarization ratio (P_{vh}/P_{vv}). Any significant changes in P_{vv} or P_{vh} without a significant change in depolarization ratio should indicate the presence of oil.

Oil type identification can be determined using a lidar polarimeter by incorporating additional spectral information in the backscatter. Employing a dual wavelength lidar polarimeter system such as that being constructed by the Remote Sensing Center at Texas A&M

University should provide adequate spectral information to perform oil type identification. Referring to the analytical model for oil on water given by (III-20), observe that the extinction coefficient in (III-20) has been shown from Table VI-4 (p. 95) to be a function of oil type and excitation wavelength. Therefore, the like and cross polarized returns measured by a dual wavelength system can be represented by the following equations:

$$P_{vv}^{r} = T' \exp(-2\alpha_r t)\ P_{vv}' \qquad \text{(VI-2)}$$

$$P_{vh}^{r} = T'' \exp(-2\alpha_r t)\ P_{vh}' \qquad \text{(VI-3)}$$

$$P_{vv}^{b} = T' \exp(-2\alpha_b t)\ P_{vv}'' \qquad \text{(VI-4)}$$

$$P_{vh}^{b} = T'' \exp(-2\alpha_b t)\ P_{vh}'' \qquad \text{(VI-5)}$$

where P_{ij}' designates the red returns in the absence of oil; P_{ij}'' designates the blue returns in the absence of oil; and and T' and T'' represent the transmission coefficients in (III-20) and (III-21). Oil detection is first established by following the same procedure mentioned above for the single wavelength system. Once oil detection is established, the ratio of the natural logarithm of P_{vv}^{r} and P_{vv}^{b}

should be observed from which the ratio α_r/α_b can be calculated as

$$\alpha_r/\alpha_b = \ln\left(\frac{P_{vv}^r}{T'P_{vv}'}\right)\Big/\ln\left(\frac{P_{vv}^b}{T'P_{vv}''}\right)$$

Referring to Table VI-4 (p. 94), observe that this ratio is single valued for the oil types, that is, each extinction coefficient ratio corresponds to only one oil type. Therefore, employing this ratio as an indicator of oil type, allows identification of oil type through dual wavelength backscatter measurements.

Oil thickness determination follows easily after oil type has been established by employing a table look-up procedure to determine the value of the extinction coefficient for the specific oil type. Employing one of these extinction coefficients, for instance α_r, in (VI-2) allows solution for the oil thickness t (ignoring transmission coefficient effects).

A possible ambiguity involved in the above procedure is that the extinction coefficient may not correspond to only one oil type. However, for the test oils used in this study, this ambiguity was not present. The detection scheme ignores the transmission coefficient effects due to a layer of oil on water. Observing the magnitudes of the transmission coefficients listed in Table VI-3 (p. 94),

however, shows that the product of the transmission coefficients used in (III-20) and (III-21) is greater than .95. Therefore, if these effects are ignored, a maximum error of 5 percent in calculating P_{VV}^{o} will be encountered. Smaller errors can be obtained by including a table look-up procedure for the index of refraction, once oil type is determined. This error does not significantly effect oil type identification (since ratios are used), but does affect oil thickness determination.

Table VI-4 (p. 94) and Figure VI-18 (p. 97) show that the attenuation of laser light due to kerosene is minimal. Therefore, kerosene on water does not appear to be detectable by the wavelengths observed in this study. However, as reported by Horvath et al. [36], kerosene has a strong, narrow absorption band at a wavelength of approximately .3 μm and could therefore be detected by a lidar polarimeter extending its wavelength to the ultraviolet region of the spectrum.

CHAPTER VII

CONCLUSIONS AND RECOMMENDATIONS

This investigation has examined, experimentally and analytically, the applicability of a dual polarization laser backscatter system for remote identification and measurement of subsurface water turbidity and oil on water. The following paragraphs describe the conclusions drawn from this study and the recommendations for future work.

Conclusions

The analytical model for describing the backscatter from smooth surfaced, turbid water developed in this investigation included single scatter and multiple scatter effects. A comparison of the experimental data with the analytical model showed that the analytical model was valid and that single scatter effects cannot be ignored, except for scattering from a very dense medium. The experimental laboratory data for backscatter from turbid water also showed that the depolarization ratio: 1) remained constant as a function of particle concentration at low particle concentrations; 2) varied directly with particle concentration at high particle concentrations; 3) varied directly with the receiver field of view; and 4) varied inversely with absorbent concentration. Experimental laboratory

data also showed that changes in transmit polarization had an insignificant effect on the backscatter.

Field measurement data from several natural waterways showed that the like and cross polarized returns and the depolarization ratio varied directly with the water quality parameters turbidity and suspended solids, and inversely with transmittance. These results support the use of a lidar polarimeter for remote measurements of turbidity, suspended solids, and transmittance.

The analytical model developed in this investigation for describing the backscatter from oil on water included the effect on the backscatter of the change in refractive index and attenuation due to the presence of oil on water. Experimental laboratory data with laterally homogeneous oil layers verified the validity of the analytical model and established the following characteristics of the data: 1) the presence of oil on turbid water does not significantly alter the depolarization ratio; and 2) the attenuation due to oil is a function of oil type, oil thickness, and excitation wavelength. Considering these effects on the backscatter, a detection scheme was presented whereby the presence of oil on water can be established using a single wavelength lidar polarimeter. A detection, type identification, and thickness measurement scheme was also presented using a dual wavelength lidar polarimeter. These

results strongly support the use of a lidar polarimeter for oil pollution detection and measurement.

Recommendations

Based on the findings of this study, several recommendations are made concerning the development of a more exact model of the backscatter from turbid water and the enhancement of the applicability of a lidar polarimeter for remote measurements of water pollution. The like polarized single scatter model presented in this investigation included an exact treatment of the single scattering mechanism, that is, the single scatter model was given in terms of the physical properties of the medium, and, therefore, required empirical results to determine its behavior. Future investigations should include an analytical treatment of the multiple scatter volume reflection coefficients (cross and like polarized) to derive expressions for these coefficients as a function of one another or as a function of the medium properties.

To more firmly establish the applicability of a lidar polarimeter for remote measurements of water quality parameters, a more exhaustive field measurements program should be conducted to determine exact relationships between the lidar returns and the physical water quality parameters. Spectral characteristics of backscatter from natural

waterways should also be investigated for possible identification of harmful, chemical subsurface pollutants.

Future investigations for oil pollution detection and identification should consider more thoroughly the spectral characteristics of many oils. This study is necessary so that the assumptions employed in the identification scheme (the ratio of two extinction coefficients for two different wavelengths is single valued) can be more thoroughly tested. Also, future experimental investigations should determine if the inhomogeneities of the oil layer are correctly accounted for in the analytical model, so that these effects may be incorporated into the detection scheme.

REFERENCES

[1] L. Ciaccio, Water and Water Pollution Handbook. New York: Marcel Derker, Inc., 1971.

[2] W. James and M. Schwebel, "Applications of Remote Sensors to Water Quality Management in the Coastal Area," Technical Report RSC-38, Remote Sensing Center, Texas A&M University, College Station, Texas, August 1972.

[3] K. Piech and J. Walker, "Aerial Color Analysis of Water Quality," Presented at January 1971 Meeting of the American Society of Civil Engineers, Phoenix, Arizona.

[4] K. Piech and J. Walker, "Photographic Analyses of Water Resource Color and Quality," Presented at March 1971 Meeting of the American Society of Photogrammetry, Washington, D.C.

[5] F. Burgess and W. James, "Airphoto Analysis of Ocean Outfall Dispersion," Federal Water Quality Office, EPA, Water Pollution Control Research Series 16070ENS.

[6] J. Halajian and H. Hallock, "Digital Photometric and Polarimetric Surveys of Water and Land Areas," Grumman Aerospace Corporation, Report No. ADR 03-02-71.1, August 1971.

[7] H. Hallock and J. Halajian, "Correlation of Optical Models and Aircraft Data of Water Turbidity," Presented at Annual Meeting of the Optical Society of America, Ottawa, Canada, October 1971.

[8] M. Schwebel, "Remote Measurements of Turbidity and Chlorophyll Through Aerial Photograph," Technical Report RSC-47, Remote Sensing Center, Texas A&M University, College Station, Texas, October 1973.

[9] N. Foster, "Aerial 8-14 Micron Imagery Applied to Mapping Thermal Effect Mixing Boundaries," Masters Thesis, Interdisciplinary Engineering, Texas A&M University, College Station, Texas, August 1970.

[10] J. Estes and B. Golomb, "Monitoring of Environmental Pollution," Journal of Remote Sensing, March-April 1966.

[11] N. Guinard, "The Remote Sensing of Oil Slicks," Processings of the Seventh International Symposium on Remote Sensing of Environment, University of Michigan, Ann Arbor, May 1971, pp. 1005-1026.

[12] H. Kim, "New Algae Mapping Technique by the Use of an Airborne Laser Fluorosensor," Applied Optics, Vol. 11, May 1972., pp. 1217-1224.

[13] J. Fantasia, "An Investigation of Oil Fluorescence as a Technique for the Remote Sensing of Oil Spills," Report No. DOT-TSC-USCG-71-7, United States Coast Guard, Washington, D.C., June 1971.

[14] V. Granastein, et al., "Multiple Scattering of Laser Light from Turbid Water," Applied Optics, vol. 11, May 1972, pp. 1217-1224.

[15] V. Granastein, et al., "Multiple Scattering of Laser Light from Turbid Water," Applied Optics, vol. 11, August 1972, pp. 1870-1871.

[16] G. Wilhelmi, W. T. Mayo, Jr., and J. W. Rouse, Jr., "Remote Water Quality Measurements with a Lidar Polarimeter," Laser and Unconventional Optics Journal, Vol. 43, January/February 1973, pp. 3-16.

[17] T. Sheives, "The Depolarization of Linearly Polarized Laser Light Backscattered from Turbid Water," Technical Memorandum RSC-68, Remote Sensing Center, Texas A&M University, College Station, Texas, March 1973.

[18] G. Wilhelmi, "An Investigation of the Depolarization of Backscattered Electromagnetic Waves Using a Lidar Polarimeter," Technical Report RSC-45, Remote Sensing Center, Texas A&M University, College Station, Texas, August 1973.

[19] W. James, "Quantitative Evaluation of Water Quality in the Coastal Zone by Remote Sensing," Technical Report RSC-33, Remote Sensing Center, Texas A&M University, College Station, Texas, September 1971.

[20] T. Camp, Water and Its Impurities, New York: Reinhold Publishing Corporation, 1963.

[21] R. Sheldon, et al., "The Size Distribution of Particles in the Ocean," Limnology and Oceanography, Vol. XVII, May 1972, p. 327-340.

[22] D. Gordon, "A Microscopic Study of Orgranic Particles in the North Atlantic Ocean," Deep Sea Research, Vol. 17, February 1970, pp. 175-185.

[23] J. Krey, "Detritus in the Ocean and Adjacent Sea", In Estuaries, ed. by G. Lauff. Washington, D.C.: American Association for the Advancement of Science, 1964.

[24] R. Biggs, "The Sediments of Chesapeake Bay," In Estuaries, ed. by G. Lauff. Washington, D.C.: American Association for the Advancement of Science, 1964.

[25] Standard Methods for the Examination of Water and Waste Water, Thirteenth Edition, New York: American Public Health Association, Inc., 1971.

[26] T. Murphy, "Environmetal Effects of Oil Pollution," Journal of the Sanitary Engineering Division, Vol. 97, June 1971, pp. 361-371.

[27] C. Mitchell, et al., "What Oil Does to Ecology," Journal Water Pollution Control Federation, Vol. 42, May 1970, pp. 812-818.

[28] E. Cowell, The Ecological Effects of Oil Pollution on Littoral Communities. Amsterdam: Elsevier Publishing Co. Ltd, 1971.

[29] J. Leader, "Bidirectional Scattering of Electromagnetic Waves from Rough Surfaces," Presented at the Spring Meeting of the USNC/URSI of the IEEE, Washington, D.C., April 1970.

[30] J. Rouse, Jr., "The Effect of the Subsurface on the Depolarization of Rough Surface Backscatter," Radio Science, vol. 7, 1972, pp. 889-895.

[31] J. Rouse, Jr., "On Volume-Dependent Depolarization of EM Backscatter from Rough Surfaces," Presented at Twentieth Meeting of Electromagnetic Wave Propagation Involving Irregular Surfaces and Inhomogeneous Media, The Hague, Netherlands, March 1974.

[32] H. van de Hulst, Light Scattering by Small Particles. New York: John Wiley & Sons, Inc., 1957.

[33] M. Kerker, The Scattering of Light and Other Electromagnetic Radiation. New York: Academic Press, 1969.

[34] Dow Chemical Company, Designed Products Department, Midland, Michigan, Personal Correspondence, August 1973.

[35] J. Lontz and B. Happoldt, Jr., "Teflon Tetrafluoroethylene Resin Dispersion," Industrial Engineering Chemistry, vol. 44, August 1952, pp. 1800-1805.

[36] R. Horvath, et al., "Measurement Program for Oil Slick Characteristics," Report No. DOT-CG-92580-A, United States Coast Guard, Washington, D.C., February 1970.

[37] C. Adams, et al., "Flux and Polarization Calculations of the Radiation Reflected from the Clouds of Venus," The Astrophysical Journal, Vol. 170, December 1971, pp. 371-386.

APPENDIX A

DESCRIPTION AND DIAGRAM OF LIDAR POLARIMETER CONTROL UNIT

The most significant improvement of the second generation field portable lidar polarimeter was the packaging of a central electronic control unit (see Figure A-1) which allows convenient operation, field portability, and faster experimental set-up time. This appendix describes a few of the considerations that were involved in the design of the electronic unit and gives detailed schematics and wiring diagrams of the electronic circuitry.

Problem Description

There are several electronic components contained within the lidar polarimeter: laser, laser power supply, two photodiode/operational amplifier (op-amp) combination detectors, photodiode/op-amp power supply, light chopper, and lock-in amplifier. The signals transferred between the above components include: chopping reference frequency light level signals from each of the two detectors, DC offset bias voltages for each op-amp, and driving power inputs for all components.

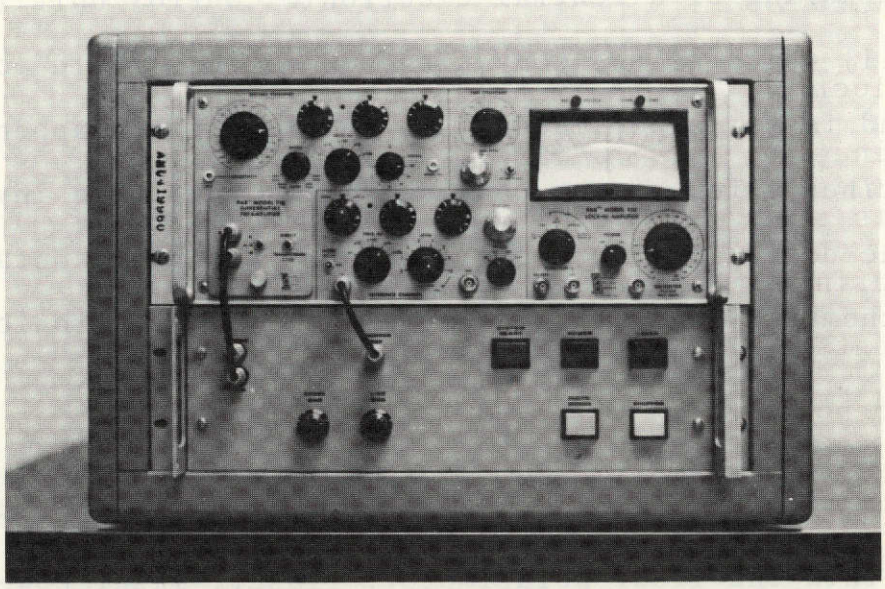

Figure A-1. Lidar Polarimeter Electronic Control Unit

Design Considerations

The magnitude of the light level voltages transferred from the photodiode op-amp detectors can be on the order of tens of microvolts. Noise design considerations such as proper shielding of signal wires and operating common mode were imperative.

Another consideration involved in the design of the electronic unit was the requirement of a twenty-five minute warm-up period for the laser power output to reach its steady state peak value. Use of the lidar polarimeter during this warm-up period would yield inaccurate measurements. A special timing circuit was therefore implemented to notify the lidar operator when this twenty-five minute warm-up period expired. Digital gating circuitry for all components was also used to notify the operator when all system components are activated and ready for operation.

A final consideration involved in the design of the electronic unit involved adapting the lidar system to the power supplied by a gasoline-powered 110 VRMS, 60-cycle generator needed for field operation. Field tests with the lidar system powered by a gasoline generator showed that the frequency stability of the 1500 watt generator was inadequate. The light chopper had a synchronous motor and the chopping frequency would not remain sufficiently

stable to allow synchronous detection with the lock-in amplifier. To alleviate this problem a special push-pull power amplifier circuit was designed and constructed to amplify the voltage supplied by a stable 60-cycle generator [Model 120-Exact Generator] to the necessary voltage and current required by the light chopper. Field tests with this additional circuit resulted in successful operation of the lidar system when powered by a gasoline-powered generator.

Electronic Unit Description

The interconnection of the electronic control unit with the transceiver of the lidar polarimeter is diagrammed in Figure A-2. Figure A-3 gives the connector and wire list, listing all labeled connectors and wires with their manufacturer and type. Figure A-4 shows the detailed wiring diagram for the connections indicated in Figure A-2.

A schematic drawing of the 110 VRMS power wiring connections of the electronic control unit is given in Figure A-5. The wiring of the indicator lights and other DC powered components is shown in Figure A-6 with an assembly drawing for Figures A-5 and A-6 given in Figure A-7. The timing, gating, and lamp driver circuits are diagrammed in Figure A-8.

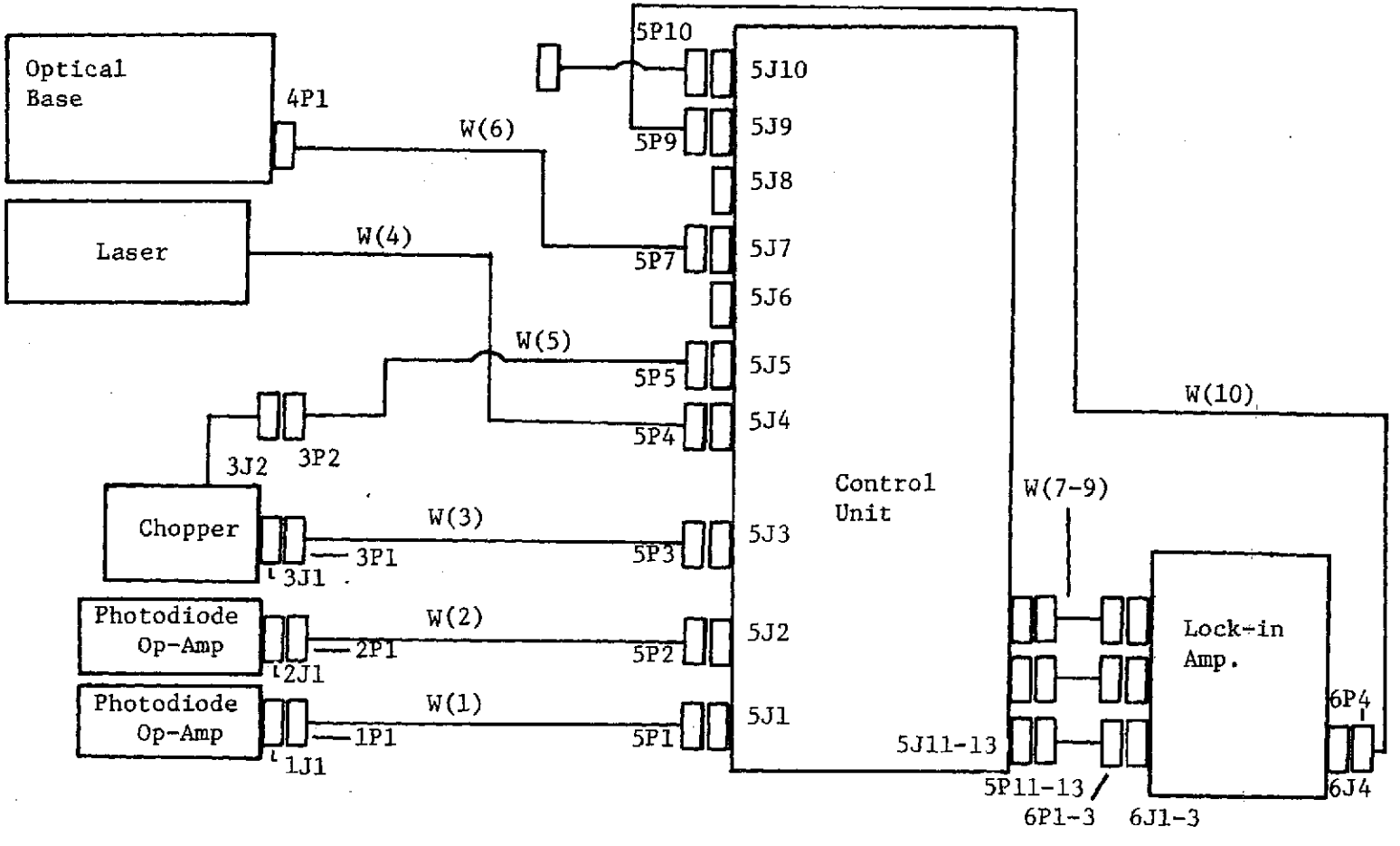

Figure A-2. Lidar Polarimeter Electronic Connections.

1J1,2J1,5J1 - Winchester 7 pin, M7S
1P1,2P1,5P1 - Winchester 7 pin, M7P
3J1 - Kings 79-46
3P1,5P11-13,6P1-3 - Amphenol UG88/U
3J2 - Cinch Jones P303-CCT-K
3P2 - Cinch-Jones P303-CCT-L
4P1 - Crimp Terminal
5J2 - Winchester 10 pin, M710S
5P2 - Winchester 10 pin, M710P
5J3 - Winchester 4 pin, M4S
5P3 - Winchester 4 pin, M4P
5J4 - Kings KV-79-18
5P4 - Kings KV-59-27
5J5-5J9 - Amphenol 160-4-N
5J6,5J7,5J8 - Terminal Plugs
5J10 - Amphenol 160-5-N
5J11-13 - Amphenol UG657/U
6J1-2 - Kings 79-46
6J3 - Kings 79-35
W(1),W(2) - Belden Audio, 3 shielded pairs, Type 8767
W(3) - Belden Audio, 1 shielded pair, Type 8434
W(4) - Belden H.V. COAX, RG/58U
W(5),W(10) - 110V AC three conductor power cord
W(6) - Single Conductor Insulated Wire (Gauge-22)
W(7) - Belden COAX, RG158/U

Figure A-3. Connector and Wire Parts List.

5J1-A→5P1-A→1P1-A→1J1-A→Pin 6, Op-Amp, signal
5J1-B→5P1-B→1P1-B→1J1-B→Pin 7, Op-Amp, +15 VDC
5J1-C→5P1-C→1P1-C→1J1-C→Pin 5, Op-Amp, DC Bias
5J1-D→5P1-D→1P1-D→1J1-D→Pin 1, Op-Amp, DC Bias
5J1-E→5P1-E→1P1-E→1J1-E→Pin 3,4, ground
5J2-A→5P2-A→2P1-A→2J1-A→Pin 6, Op-Amp, signal
5J2-B→5P2-B→2P1-B→2J1-B→Pin 7, Op-Amp, +15 VDC
5J2-C→592-C→2P1-C→2J1-C→Pin 5, Op-Amp, DC Bias
5J2-D→5P2-D→2P1-D→2J1-D→Pin 1, Op-Amp, DC Bias
5J2-E→5P2-E→2P1-E→2J1-E→Pin 3,4, Op-Amp, ground
5J3→5P3→3P2→3J2→chopper reference
5J4, switched high voltage→5P4, laser high voltage
5J5, switched 110 VAC→3P2 3J2, chopper 110 VAC
5J6, Auxiliary + 15 VDC→
5J7, Auxiliary Chassis ground→4P1, optical base
5J8, Auxiliary - 15 VDC→
5J9, Auxiliary 110 VAC→5P9, lockin x 110 VAC
5J10, 110 VAC input→5J10
5J1-A→5J11→5P11→6P1→6J1, signal
5J2-A→5J12→5P12→6P2→6J2, signal
5J3-A→5J13→5P13→6P3→6J3, chopper reference

Figure A-4. Interconnection Diagram for Figure A-2.

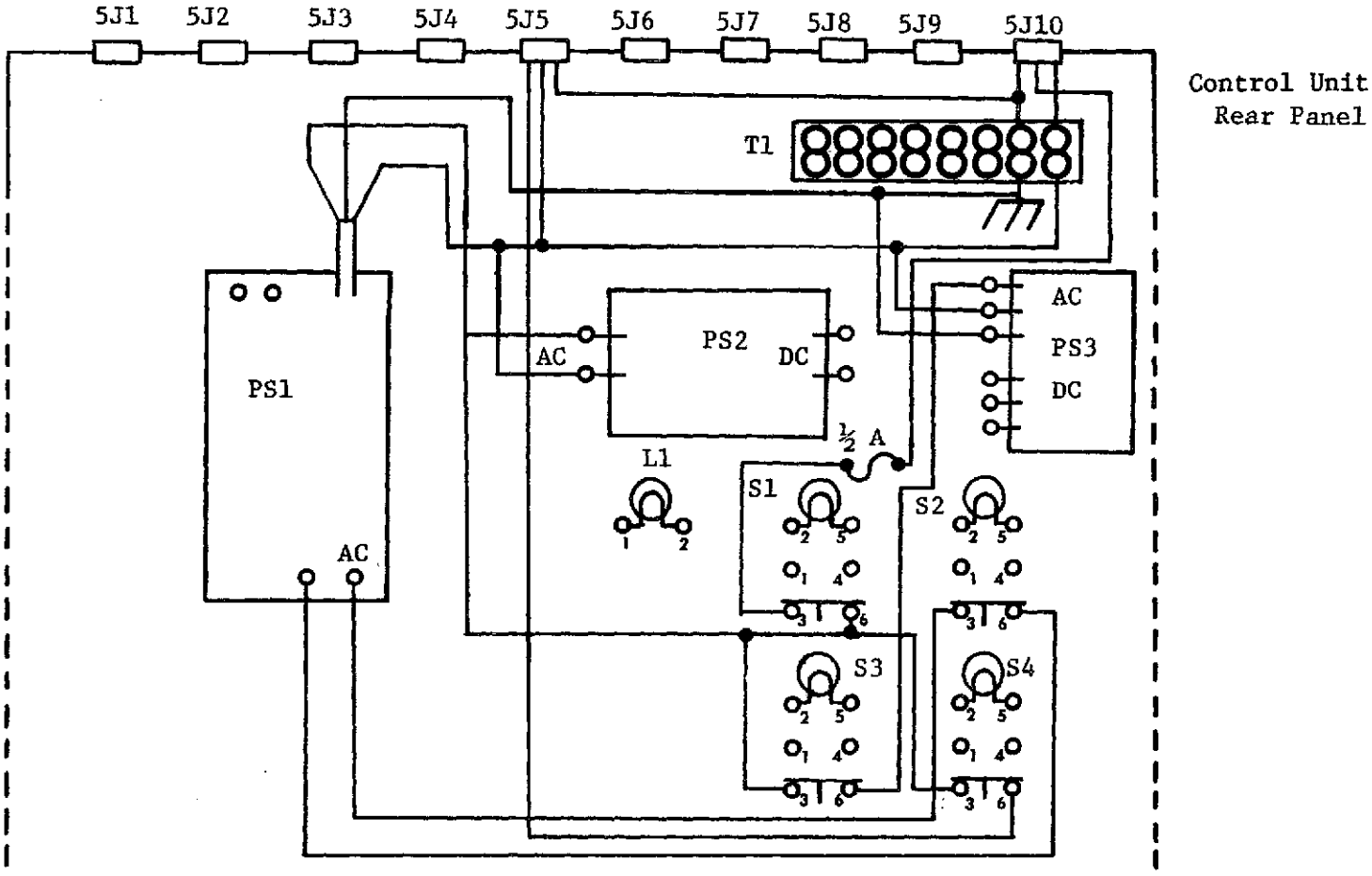

Figure A-5. AC Power Wiring Diagram.

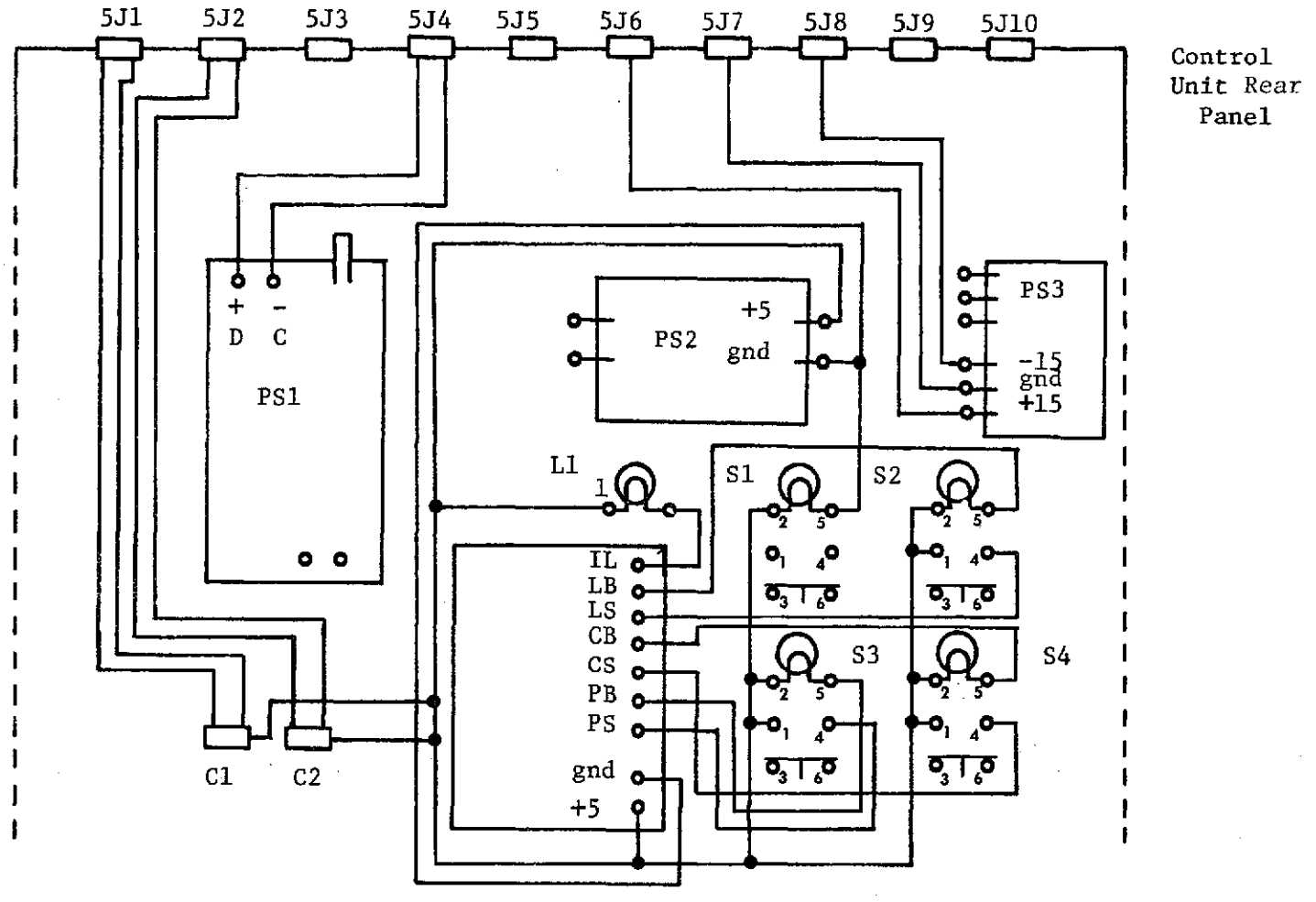

Figure A-6. DC Wiring Diagram.

PS1 - Spectra Physics Model 124 Laser Power Supply

PS2 - Wanlass OEM Power Supply, 5V @ 3A, Type DPS1-5

PS3 - Analog Devices Power Supply, ±15V, Model 950

L1 - System Status Indicator Light, Dialco Type 533-0901, with lense Dialco Type 303-3472

S1 - Main Power Switch, Dialco Type 513-1504-001 with lense Dialco Type 303-3474

S2 - Laser Power Switch, Dialco Type 513-1509-001 with lense Dialco Type 303-3471

S3 - Photo-diode OpAmp Power Supply Switch, Dialco Type 513-1509-001 with lense Dialco Type 303-3473

S4 - Chopper Power Switch, Dialco Type 513-1509-001 with lense Dialco Type 303-3475

T1 - Cinch Terminal Strip - Type 6-141

C1, C2 - Spectrol 10K Precision Potentiometers - Model 1532

Figure A-7. Assembly Drawing for Figures A-5 and A-6.

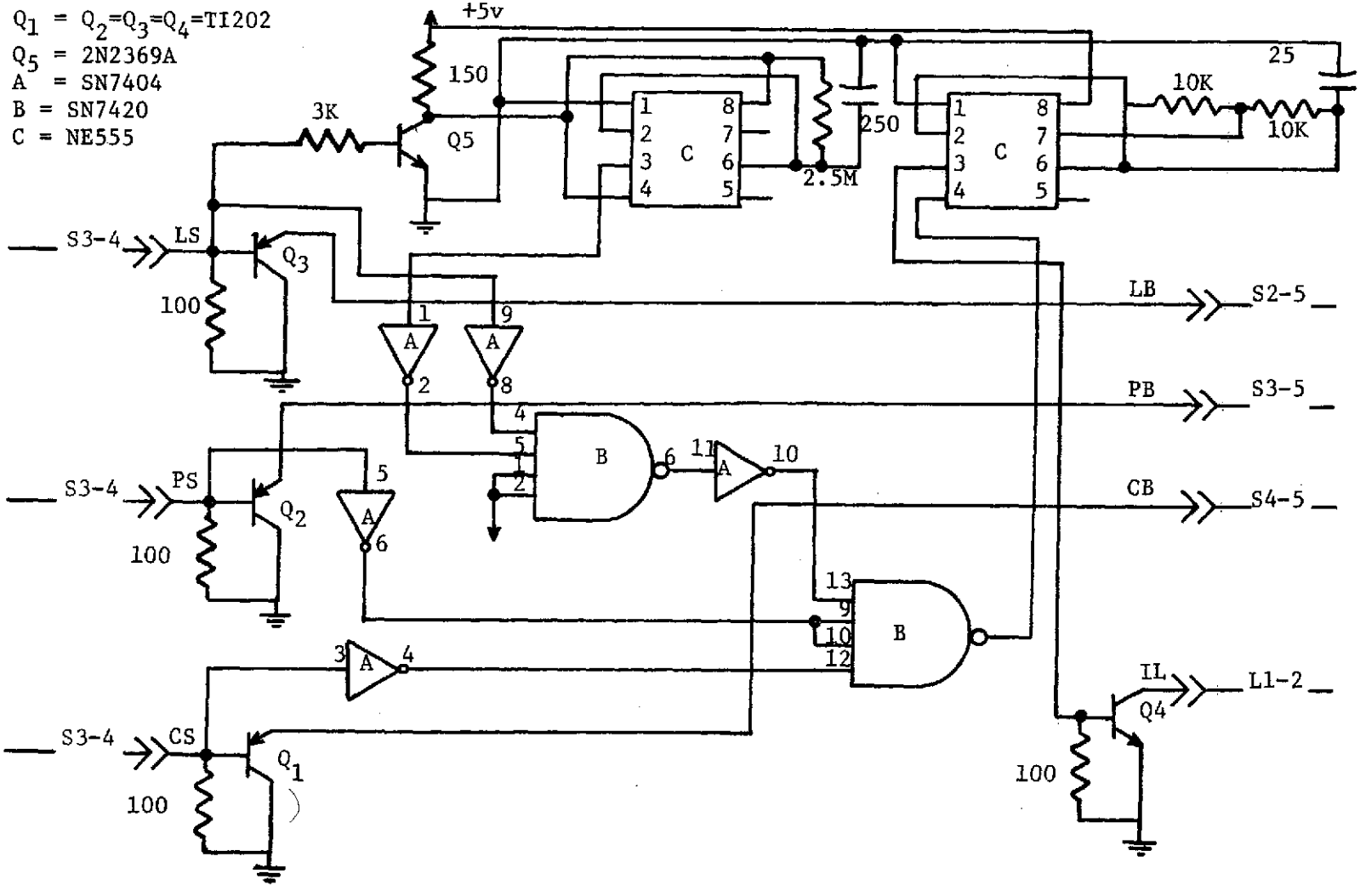

Figure A-8. Logic, Timer, and Lamp Driver Circuits.

The push-pull power amplifier circuit designed and constructed to provide a stable power frequency for the light chopper is diagrammed in Figure A-9. Supplying a 60-cycle 1.5 volt peak-to-peak voltage at the input of this circuit (along with a 35 V @ 7 amp operating voltage) results in a 110 VRMS output capable of supplying 14 watts of power.

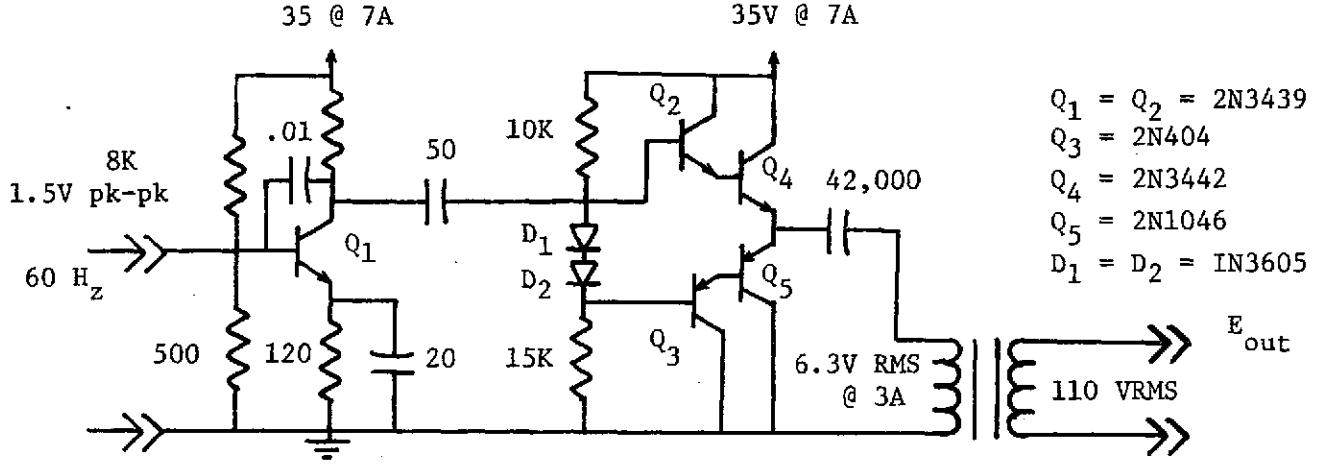

Figure A-9. Push-Pull Amplifier Circuit.

APPENDIX B

DATA

This appendix presents the data collected for this investigation. The data is segmented into three types of measurements: 1) laboratory turbid water measurements (Table B-1); 2) laboratory oil on water measurements (Table B-2); and 3) field measurements from natural waterways (Table B-3). Several lidar system parameters and measurement parameters that were used for this investigation are listed under the column CODE. The interpretation for this code is discussed below.

a b c d - The digit a represents the type of particles used for the turbid medium. Values for a are:

1 - Dow Plastic Pigment 722

2 - E.I. Dupont Resin Dispersion, TFE 30

3 - Natural Water (field measurement)

The digit b represents the slant range. Values for b are:

1 - 9.5 m

2 - 2.84 m

3 - 1.44 m

The digit c represents the diameter of the receiver field of view at the surface of the water. Values for c are:

1 - 4.2 cm

2 - 7.04 cm

3 - 21.1 cm

4 - 70.4 cm

5 - 1.26 cm

6 - .32 cm

7 - .64 cm

8 - 1.07 cm

The digit d represents the distance between the receiver and the transmitter at the transceiver section. Values for d are:

1 - 12.4 cm

2 - 7.3 cm

SAMPLE NUMBER	DATE	CODE	PARTICLE CONCENTRATION (NUMBER/ML)	PVV(WATTS)	PVH(WATTS)	PHH(WATTS)	PHV(WATTS)
2	11474	1362	0.175E 07	0.117E-10	0.117E-12	----------	----------
3	11474	1362	0.354E 07	0.235E-10	0.352E-12	----------	----------
4	11474	1362	0.530E 07	0.352E-10	0.470E-12	----------	----------
5	11474	1362	0.123E 08	0.764E-10	0.106E-11	----------	----------
6	11474	1362	0.192E 08	0.116E-09	0.176E-11	----------	----------
7	11474	1362	0.367E 08	0.210E-09	0.329E-11	----------	----------
8	11474	1362	0.715E 08	0.351E-09	0.587E-11	----------	----------
9	11474	1362	0.141E 09	0.603E-09	0.115E-10	----------	----------
10	11474	1362	0.296E 09	0.833E-09	0.186E-10	----------	----------
11	11474	1362	0.567E 09	0.104E-08	0.322E-10	----------	----------
12	11474	1362	0.142E 10	0.151E-08	0.902E-10	----------	----------
13	11474	1362	0.272E 10	0.234E-08	0.270E-09	----------	----------
14	11474	1362	0.735E 10	0.433E-08	0.113E-08	----------	----------
15	11474	1362	0.117E 11	0.621E-08	0.235E-08	----------	----------
16	11474	1362	0.160E 11	0.821E-08	0.376E-08	----------	----------
17	11474	1362	0.203E 11	0.103E-07	0.552E-08	----------	----------
19	11474	1372	0.175E 07	0.247E-10	0.587E-12	----------	----------
20	11474	1372	0.351E 07	0.517E-10	0.117E-11	----------	----------
21	11474	1372	0.530E 07	0.752E-10	0.141E-11	----------	----------
22	11474	1372	0.123E 08	0.168E-09	0.282E-11	----------	----------
23	11474	1372	0.192E 08	0.261E-09	0.482E-11	----------	----------
24	11474	1372	0.367E 08	0.458E-09	0.799E-11	----------	----------
25	11474	1372	0.715E 08	0.679E-09	0.132E-10	----------	----------
26	11474	1372	0.141E 09	0.869E-09	0.200E-10	----------	----------
27	11474	1372	0.296E 09	0.113E-08	0.345E-10	----------	----------
28	11474	1372	0.567E 09	0.148E-08	0.674E-10	----------	----------
29	11474	1372	0.142E 10	0.261E-08	0.284E-09	----------	----------
30	11474	1372	0.272E 10	0.409E-08	0.834E-09	----------	----------
31	11474	1372	0.735E 10	0.801E-08	0.341E-08	----------	----------
32	11474	1372	0.117E 11	0.127E-07	0.705E-08	----------	----------
33	11474	1372	0.160E 11	0.169E-07	0.108E-07	----------	----------
34	11474	1372	0.203E 11	0.218E-07	0.155E-07	----------	----------
36	11474	1382	0.175E 07	0.334E-10	0.106E-11	----------	----------
37	11474	1382	0.351E 07	0.698E-10	0.153E-11	----------	----------
38	11474	1382	0.530E 07	0.102E-09	0.247E-11	----------	----------

Table B-1. Turbid Water Data.

SAMPLE NUMBER	DATE	CODE	PARTICLE CONCENTRATION (NUMBER/ML)	PVV(WATTS)	PVH(WATTS)	PHH(WATTS)	PHV(WATTS)
39	11474	1382	0.881E 07	0.172E-09	0.364E-11	----------	----------
40	11474	1382	0.123E 08	0.233E-09	0.529E-11	----------	----------
41	11474	1382	0.192E 08	0.348E-09	0.646E-11	----------	----------
42	11474	1382	0.367E 08	0.560E-09	0.112E-10	----------	----------
43	11474	1382	0.715E 08	0.807E-09	0.201E-10	----------	----------
44	11474	1382	0.141E 09	0.105E-08	0.300E-10	----------	----------
45	11474	1382	0.296E 09	0.138E-08	0.593E-10	----------	----------
46	11474	1382	0.567E 09	0.195E-08	0.138E-09	----------	----------
47	11474	1382	0.142E 10	0.350E-08	0.563E-09	----------	----------
48	11474	1382	0.272E 10	0.636E-08	0.214E-08	----------	----------
49	11474	1382	0.735E 10	0.136E-07	0.799E-08	----------	----------
50	11474	1382	0.117E 11	0.202E-07	0.136E-07	----------	----------
51	11474	1382	0.160E 11	0.272E-07	0.204E-07	----------	----------
52	11474	1382	0.203E 11	0.324E-07	0.258E-07	----------	----------
54	11574	2372	0.454E 09	0.634E-11	0.235E-12	0.752E-11	0.235E-12
55	11574	2372	0.907E 09	0.141E-10	0.705E-12	0.141E-10	0.470E-12
56	11574	2372	0.136E 10	0.211E-10	0.164E-11	0.211E-10	0.705E-12
57	11574	2372	0.227E 10	0.348E-10	0.352E-11	0.348E-10	0.211E-11
58	11574	2372	0.318E 10	0.470E-10	0.493E-11	0.484E-10	0.399E-11
59	11574	2372	0.499E 10	0.745E-10	0.822E-11	0.750E-10	0.799E-11
60	11574	2372	0.863E 10	0.128E-09	0.153E-10	0.126E-09	0.167E-10
61	11574	2372	0.132E 11	0.195E-09	0.223E-10	0.195E-09	0.268E-10
62	11574	2372	0.222E 11	0.335E-09	0.364E-10	0.329E-09	0.484E-10
63	11574	2372	0.313E 11	0.471E-09	0.505E-10	0.458E-09	0.707E-10
64	11574	2372	0.449E 11	0.647E-09	0.740E-10	0.669E-09	0.978E-10
65	11574	2372	0.722E 11	0.104E-08	0.116E-09	0.104E-08	0.159E-09
66	11574	2372	0.994E 11	0.135E-08	0.154E-09	0.133E-08	0.206E-09
67	11574	2372	0.168E 12	0.192E-08	0.222E-09	0.191E-08	0.298E-09
68	11574	2372	0.304E 12	0.269E-08	0.323E-09	0.260E-08	0.422E-09
69	11574	2372	0.576E 12	0.328E-08	0.443E-09	0.330E-08	0.587E-09
70	11574	2372	0.112E 13	0.420E-08	0.669E-09	0.422E-08	0.840E-09
71	11574	2372	0.248E 13	0.563E-08	0.124E-08	0.563E-08	0.146E-08
72	11574	2372	0.657E 13	0.974E-08	0.334E-08	0.986E-08	0.371E-08
73	11574	2372	0.107E 14	0.131E-07	0.564E-08	0.131E-07	0.611E-08

Table B-1. Turbid Water Data Continued.

SAMPLE NUMBER	DATE	CODE	PARTICLE CONCENTRATION (NUMBER/ML)	DYE CONCENTRATION (MG/L)	PVV(WATTS)	PVH(WATTS)
1	11774	1372	0.437E 10	0.000E 00	0.564E-08	0.160E-08
2	11774	1372	0.437E 10	0.809E 00	0.536E-08	0.132E-08
3	11774	1372	0.437E 10	0.162E 01	0.517E-08	0.123E-08
4	11774	1372	0.437E 10	0.485E 01	0.482E-08	0.105E-08
5	11774	1372	0.437E 10	0.113E 02	0.421E-08	0.827E-09
6	11774	1372	0.437E 10	0.243E 02	0.336E-08	0.571E-09
7	11774	1372	0.437E 10	0.502E 02	0.247E-08	0.348E-09
8	11774	1372	0.437E 10	0.110E 03	0.150E-08	0.160E-09
9	11774	1372	0.437E 10	0.214E 03	0.822E-09	0.564E-10

Table B-1. Turbid Water Data Continued.

SAMPLE NUMBER	DATE	CODE	PARTICLE CONCENTRATION (NUMBER/ML)	OIL TYPE	OIL THICKNESS (MM)	PVV(WATTS)	PVH(WATTS)
1	11774	1372	0.175E 10	NO2 FUEL	0.000	0.893E-08	0.388E-08
2	11774	1372	0.175E 10	NO2 FUEL	0.050	0.728E-08	0.294E-08
3	11774	1372	0.175E 10	NO2 FUEL	0.100	0.517E-08	0.211E-08
4	11774	1372	0.175E 10	NO2 FUEL	0.500	0.172E-08	0.681E-09
5	11774	1372	0.175E 10	NO2 FUEL	1.100	0.310E-09	0.132E-09
6	11774	1372	0.175E 10	NO2 FUEL	2.500	0.211E-10	0.822E-11
7	11774	1372	0.175E 10	SAE 30	0.000	0.893E-08	0.399E-08
8	11774	1372	0.175E 10	SAE 30	0.050	0.869E-08	0.376E-08
9	11774	1372	0.175E 10	SAE 30	0.100	0.846E-08	0.352E-08
10	11774	1372	0.175E 10	SAE 30	0.500	0.822E-08	0.329E-08
11	11774	1372	0.175E 10	SAE 30	1.100	0.775E-08	0.317E-08
12	11774	1372	0.175E 10	SAE 30	2.500	0.728E-08	0.294E-08
13	11774	1372	0.175E 10	SAE 30	3.500	0.658E-08	0.270E-08
14	11774	1372	0.175E 10	SAE 30	5.500	0.587E-08	0.235E-08
15	11774	1372	0.175E 10	GASOLINE	0.000	0.846E-08	0.364E-08
16	11774	1372	0.175E 10	GASOLINE	0.050	0.846E-08	0.364E-08
17	11774	1372	0.175E 10	GASOLINE	0.100	0.846E-08	0.364E-08
18	11774	1372	0.175E 10	GASOLINE	0.500	0.822E-08	0.352E-08
19	11774	1372	0.175E 10	GASOLINE	1.100	0.811E-08	0.343E-08
20	11774	1372	0.175E 10	GASOLINE	2.500	0.799E-08	0.329E-08
21	11774	1372	0.175E 10	GASOLINE	3.500	0.794E-08	0.324E-08
22	11774	1372	0.175E 10	GASOLINE	5.500	0.787E-08	0.320E-08
23	11774	1372	0.175E 10	KEROSENE	0.000	0.869E-08	0.376E-08
24	11774	1372	0.175E 10	KEROSENE	0.050	0.846E-08	0.357E-08
25	11774	1372	0.175E 10	KEROSENE	0.100	0.834E-08	0.352E-08
26	11774	1372	0.175E 10	KEROSENE	0.500	0.822E-08	0.350E-08
27	11774	1372	0.175E 10	KEROSENE	1.100	0.811E-08	0.341E-08
28	11774	1372	0.175E 10	KEROSENE	2.500	0.806E-08	0.329E-08
29	11774	1372	0.175E 10	KEROSENE	3.500	0.804E-08	0.327E-08
30	11774	1372	0.175E 10	KEROSENE	5.500	0.787E-08	0.317E-08
31	11774	1372	0.397E 11	L CRUDE	0.000	0.376E-07	0.305E-07
32	11774	1372	0.397E 11	L CRUDE	0.050	0.905E-08	0.705E-08
33	11774	1372	0.397E 11	L CRUDE	0.100	0.329E-08	0.258E-08
34	11774	1372	0.397E 11	L CRUDE	0.200	0.247E-09	0.188E-09
35	11774	1372	0.397E 11	L CRUDE	0.300	0.176E-10	0.136E-10

Table B-2. Oil on Water Data.

SAMPLE NUMBER	DATE	CODE	PVV(WATTS)	PVH(WATTS)	PHH(WATTS)	PHV(WATTS)	TURBIDITY (FTU)	TRANSMITTANCE (%)	SUSPENDED SOLIDS (MG/L)
4	71473	3141	0.493E-10	0.106E-10	0.493E-10	0.117E-10	7.0	93.7	----------
14	71473	3131	0.388E-10	0.752E-11	0.388E-10	0.775E-11	8.0	93.5	----------
23	71473	3121	0.258E-10	0.352E-11	0.247E-10	0.352E-11	8.0	92.5	----------
36	71473	3111	0.223E-10	0.352E-11	0.211E-10	0.352E-11	9.0	94.0	10.0
54	71573	3111	0.458E-10	0.940E-11	0.446E-10	0.940E-11	28.0	75.0	38.0
59	71573	3111	0.435E-10	0.728E-11	----------	----------	21.0	81.0	31.0
60	71573	3111	0.411E-10	0.611E-11	----------	----------	22.0	81.0	----------
82	71573	3111	0.540E-10	0.113E-10	----------	----------	32.0	73.0	49.0
345	92573	3251	0.188E-09	0.294E-10	----------	----------	26.0	84.0	----------
230	92573	3251	0.153E-09	0.141E-10	----------	----------	22.0	86.0	----------
326	92573	3251	0.117E-09	0.141E-10	----------	----------	20.0	87.0	----------
134	92573	3251	0.117E-09	0.822E-11	----------	----------	18.0	88.0	----------
112	92573	3251	0.117E-09	0.940E-11	----------	----------	19.0	87.0	----------
362	92573	3251	0.822E-10	0.940E-11	----------	----------	18.0	89.0	----------
113	92573	3251	0.963E-10	0.106E-10	----------	----------	18.0	88.0	----------
150	92573	3251	0.112E-09	0.106E-10	----------	----------	17.0	89.0	----------
34	92573	3251	0.822E-10	0.822E-11	----------	----------	16.0	90.0	----------
235	92573	3251	0.681E-10	0.940E-11	----------	----------	15.0	90.0	----------
99	120173	3252	0.235E-09	0.388E-10	----------	----------	46.0	81.0	113.0
77	120173	3252	0.329E-09	0.705E-10	----------	----------	82.0	63.0	141.0
57	120173	3252	0.399E-09	0.999E-10	----------	----------	215.0	40.0	266.0
225	120173	3252	0.587E-09	0.200E-09	----------	----------	350.0	19.0	----------
24	120173	3252	0.200E-09	0.376E-10	----------	----------	42.0	81.0	125.0
59	120173	3252	0.282E-09	0.576E-10	----------	----------	75.0	60.0	----------
41	120173	3252	0.670E-09	0.258E-09	----------	----------	450.0	10.5	608.0
264	120173	3252	0.752E-09	0.305E-09	----------	----------	575.0	6.5	814.0
217	120173	3252	0.188E-09	0.352E-10	----------	----------	25.0	86.5	----------
165	120173	3252	0.846E-09	0.364E-09	----------	----------	650.0	5.0	----------
78	120173	3252	0.705E-09	0.294E-09	----------	----------	550.0	7.2	----------
250	120173	3252	0.634E-09	0.223E-09	----------	----------	500.0	10.0	430.0
90	120173	3252	0.799E-09	0.329E-09	----------	----------	625.0	4.5	----------
134	120173	3252	0.101E-08	0.517E-09	----------	----------	700.0	2.8	2056.0
56	120173	3252	0.176E-09	0.235E-10	----------	----------	28.0	84.0	----------
23	120173	3252	0.294E-09	0.564E-10	----------	----------	69.0	70.5	----------
52	120173	3252	0.136E-09	0.141E-10	----------	----------	16.0	89.0	----------
360	120173	3252	0.940E-10	0.113E-10	----------	----------	12.0	95.0	----------
352	120173	3252	0.799E-10	0.940E-11	----------	----------	11.0	96.0	62.0
35	120173	3252	0.987E-10	0.113E-10	----------	----------	12.0	96.0	----------
135	120173	3252	0.164E-09	0.235E-10	----------	----------	27.0	89.5	68.0
70	120173	3252	0.235E-09	0.399E-10	----------	----------	44.0	77.5	----------
386	120173	3252	0.200E-09	0.329E-10	----------	----------	45.0	81.5	----------

Table B-3. Field Data from Natural Waterways.